

## PUBLISHER :



### Address of Publisher & Editor's Office :

GDAŃSK UNIVERSITY  
OF TECHNOLOGY

Faculty  
of Ocean Engineering  
& Ship Technology

ul. Narutowicza 11/12  
80-952 Gdańsk, POLAND  
tel.: +48 58 347 13 66  
fax : +48 58 341 13 66  
e-mail : office.pmr@pg.gda.pl

### Account number :

**BANK ZACHODNI WBK S.A.**  
I Oddział w Gdańsku  
41 1090 1098 0000 0000 0901 5569

### Editorial Staff :

**Tadeusz Borzęcki** Editor in Chief  
e-mail : tadbtor@pg.gda.pl

**Przemysław Wierzychowski** Scientific Editor  
e-mail : e.wierzychowski@chello.pl

**Jan Michalski** Editor for review matters  
e-mail : janmi@pg.gda.pl

**Aleksander Kniat** Editor for international relations  
e-mail : olek@pg.gda.pl

**Kazimierz Kempa** Technical Editor  
e-mail : kkempa@pg.gda.pl

**Piotr Bzura** Managing Editor  
e-mail : pbzura@pg.gda.pl

**Cezary Spigarski** Computer Design  
e-mail : biuro@oficynamorska.pl

**Domestic price :**  
single issue : 20 zł

**Prices for abroad :**  
single issue :  
- in Europe EURO 15  
- overseas US\$ 20

**ISSN 1233-2585**



**POLISH  
MARITIME  
RESEARCH**

*in internet*

[www.bg.pg.gda.pl/pmr/pmr.php](http://www.bg.pg.gda.pl/pmr/pmr.php)



## POLISH MARITIME RESEARCH

No 3(66) 2010 Vol 17

## CONTENTS

- 3** **TOMASZ ABRAMOWSKI,  
TADEUSZ SZELANGIEWICZ**  
*Numerical analysis of influence of selected elements  
on effectiveness of streamline rudder*
- 8** **JÓZEF SZALA,  
GRZEGORZ SZALA**  
*A fatigue life calculation method for structural elements  
made of D16CzATW aluminium alloy*
- 18** **ZYGMUNT PASZOTA**  
*Theoretical and mathematical models of the torque  
of mechanical losses in a hydraulic rotational motor  
for hydrostatic drive*
- 26** **EUGENIUSZ KOZACZKA,  
JACEK DOMAGALSKI,  
IGNACY GŁOZA**  
*Investigation of the underwater noise produced  
by ships by means of intensity method*
- 37** **LESZEK MATUSZEWSKI,  
KRZYSZTOF FALKOWSKI**  
*Mathematical model of radial passive magnetic bearing*
- 45** **EUGENIUSZ RANATOWSKI**  
*Problems of welding in shipbuilding - an analytic-numerical  
assessment of the thermal cycle in HAZ  
with three dimensional heat source models in agreement  
with modelling rules. (Part III)*
- 53** **LESŁAW KYZIOŁ**  
*Analysis of fracture toughness of structural timber (Part I)*

# Editorial

---

POLISH MARITIME RESEARCH is a scientific journal of worldwide circulation. The journal appears as a quarterly four times a year. The first issue of it was published in September 1994. Its main aim is to present original, innovative scientific ideas and Research & Development achievements in the field of :

## **Engineering, Computing & Technology, Mechanical Engineering,**

which could find applications in the broad domain of maritime economy. Hence there are published papers which concern methods of the designing, manufacturing and operating processes of such technical objects and devices as : ships, port equipment, ocean engineering units, underwater vehicles and equipment as well as harbour facilities, with accounting for marine environment protection.

The Editors of POLISH MARITIME RESEARCH make also efforts to present problems dealing with education of engineers and scientific and teaching personnel. As a rule, the basic papers are supplemented by information on conferences , important scientific events as well as cooperation in carrying out international scientific research projects.

## Scientific Board

---

Chairman : Prof. **JERZY GIRTLEK** - Gdańsk University of Technology, Poland

Vice-chairman : Prof. **ANTONI JANKOWSKI** - Institute of Aeronautics, Poland

Vice-chairman : Prof. **MIROSLAW L. WYSZYŃSKI** - University of Birmingham, United Kingdom

---

Dr **POUL ANDERSEN**  
Technical University  
of Denmark  
Denmark

Prof. **STANISŁAW GUCMA**  
Maritime University of Szczecin  
Poland

Dr **YOSHIO SATO**  
National Traffic Safety  
and Environment Laboratory  
Japan

Dr **MEHMET ATLAR**  
University of Newcastle  
United Kingdom

Prof. **ANTONI ISKRA**  
Poznań University  
of Technology  
Poland

Prof. **KLAUS SCHIER**  
University of Applied Sciences  
Germany

Prof. **GÖRAN BARK**  
Chalmers University  
of Technology  
Sweden

Prof. **JAN KICIŃSKI**  
Institute of Fluid-Flow Machinery  
of PASci  
Poland

Prof. **FREDERICK STERN**  
University of Iowa,  
IA, USA

Prof. **SERGEY BARSUKOV**  
Army Institute of Odessa  
Ukraine

Prof. **ZYGMUNT KITOWSKI**  
Naval University  
Poland

Prof. **JÓZEF SZALA**  
Bydgoszcz University  
of Technology and Agriculture  
Poland

Prof. **MUSTAFA BAYHAN**  
Süleyman Demirel University  
Turkey

Prof. **JAN KULCZYK**  
Wrocław University of Technology  
Poland

Prof. **TADEUSZ SZELANGIEWICZ**  
Technical University  
of Szczecin  
Poland

Prof. **MAREK DZIDA**  
Gdańsk University  
of Technology  
Poland

Prof. **NICOS LADOMMATOS**  
University College London  
United Kingdom

Prof. **WITALIJ SZCZAGIN**  
State Technical University  
of Kaliningrad  
Russia

Prof. **ODD M. FALTINSEN**  
Norwegian University  
of Science and Technology  
Norway

Prof. **JÓZEF LISOWSKI**  
Gdynia Maritime University  
Poland

Prof. **BORIS TIKHOMIROV**  
State Marine University  
of St. Petersburg  
Russia

Prof. **PATRICK V. FARRELL**  
University of Wisconsin  
Madison, WI  
USA

Prof. **JERZY MATUSIAK**  
Helsinki University  
of Technology  
Finland

Prof. **DRACOS VASSALOS**  
University of Glasgow  
and Strathclyde  
United Kingdom

Prof. **WOLFGANG FRICKE**  
Technical University  
Hamburg-Harburg  
Germany

Prof. **EUGEN NEGRUS**  
University of Bucharest  
Romania

Prof. **YASUHIKO OHTA**  
Nagoya Institute of Technology  
Japan

# Numerical analysis of influence of selected elements on effectiveness of streamline rudder

Tomasz Abramowski, Ph. D.

Tadeusz Szelangiewicz, Prof.

West Pomeranian University of Technology, Szczecin

## ABSTRACT

*During designing steering gear for large fast transport ships (e.g. container carriers), shipowners usually put forward strong demands concerning ship manoeuvrability. It means that streamline rudders should be characterized by a high effectiveness, i.e. fast increasing values of lifting force in function of rudder angle and large values of lifting force related to rudder area. As gabarites of streamline rudder depend on a form and draught of stern part of ship's hull, an improvement of rudder effectiveness can be reached by an appropriate selection of rudder profile and application of additional elements to rudder blade.*

*This paper presents results of numerical investigations (by using CFD methods) of hydrodynamic forces acting on rudder blades of the same gabarites but based on different profiles. Such calculations were also performed for selected rudder blades fitted with additional elements intended for the improving of rudder effectiveness.*

**Keywords:** streamline rudder; improvement of rudder effectiveness; computational fluid dynamics (CFD)

## INTRODUCTION

During designing the streamline rudder its designer tends to make its effectiveness as large as possible. The effect can be reached by selecting an appropriate geometry of rudder, including its profile, as well as by applying additional elements which on the one hand are able e.g. to increase lifting force, and on the other hand e.g. to reduce tip losses.

In the subject-matter literature can be found dimensionless results of model tests of hydrodynamic characteristics of airfoils or other profiles used in designing a given rudder of determined dimensions. However similar results of model tests of the rudders fitted with additional elements can be not always recalculated to a designed rudder of determined dimensions. Determination of effectiveness of a designed rudder can be hence performed:

- either by conducting its model tests in a model basin,
- or by using computational fluid dynamics methods (CFD).

Model tests of rudders are much more expensive than numerical analyses which can be presently conducted both for models and full scale objects in view of rather easy access to high-performance computers, today.

## SCOPE OF THE NUMERICAL INVESTIGATIONS

The numerical investigations were conducted in two phases:

- I. In the first phase hydrodynamic characteristics of the profiles (Fig. 1) applicable to designing the rudders, were calculated. Dimensions of the rudders and their blade area

were the same as of the final rudder installed on B573 ship [1], which served as the initial object in the analyses in question.

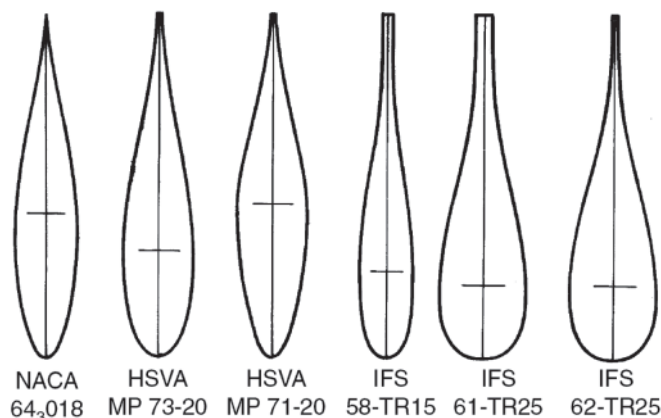


Fig. 1. The profiles used for the investigated rudders

- II. In the second phase certain modifications were introduced to the selected rudders of the above given profiles, and then successive calculations of their hydrodynamic characteristics were made, namely:

- for the rudder of NACA 0018 profile, fitted with a pivoting flap in the rear part of the profile, containing its trailing edge (Fig. 3a). In compliance with the subject-matter literature it was assumed that the deflection angle of the flap relative to rudder axis is equal to that of the main part of rudder blade (if the rudder angle was equal to  $30^\circ$  then the whole deflection angle of the flap was equal to  $60^\circ$ ).

- for the rudder of IFS58-TR15 profile with an additional plate fixed at rudder top to reduce generation of tip vortices (Schilling rudder, Fig. 3b).

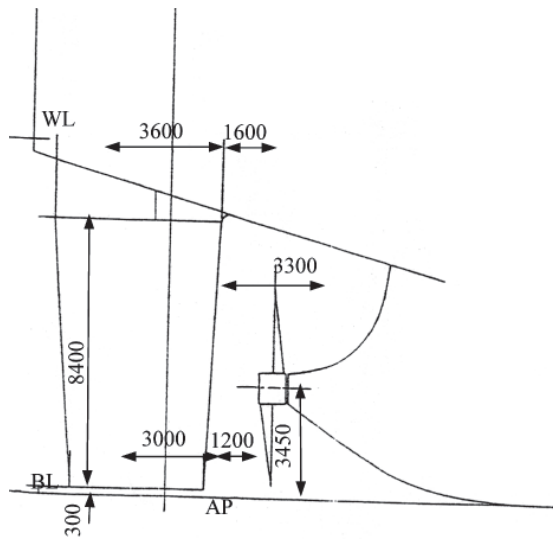


Fig. 2. The final rudder of B573 ship [1], of the area  $A_r = 39.48 \text{ m}^2$  and the aspect ratio  $\lambda = 1.79$

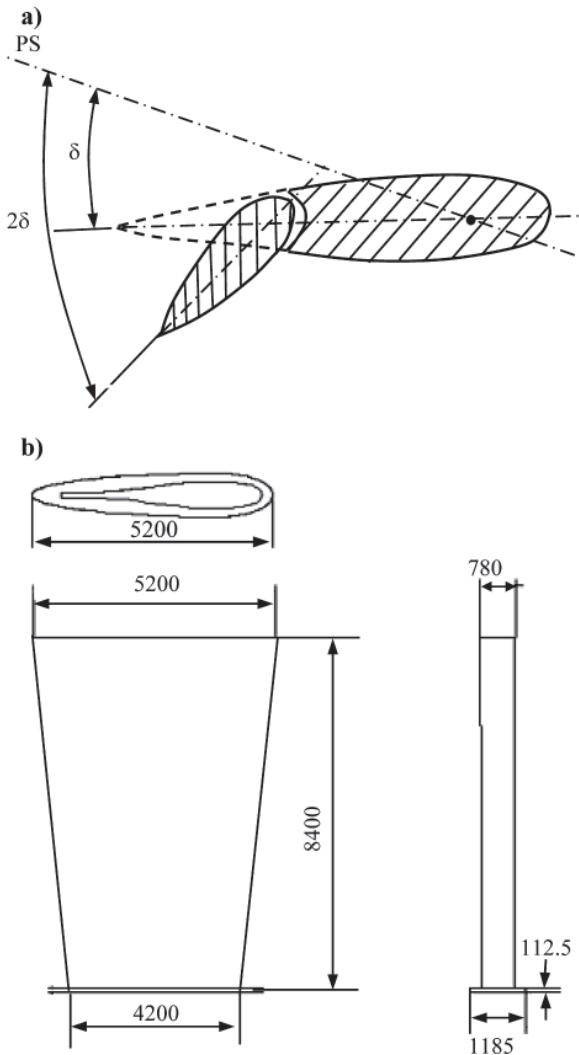


Fig. 3. Modification variants of the selected rudders:

- NACA 0018 rudder fitted with a pivoting flap.
- IFS 58-TR15 rudder fitted with an additional plate (Schilling's rudder)

The modified rudders maintained the same contour and dimensions as those of the B573 ship's rudder.

## THE METHOD AND DOMAIN OF COMPUTATIONS

The computational model of the rudder prepared for numerical calculations is presented in Fig. 4.

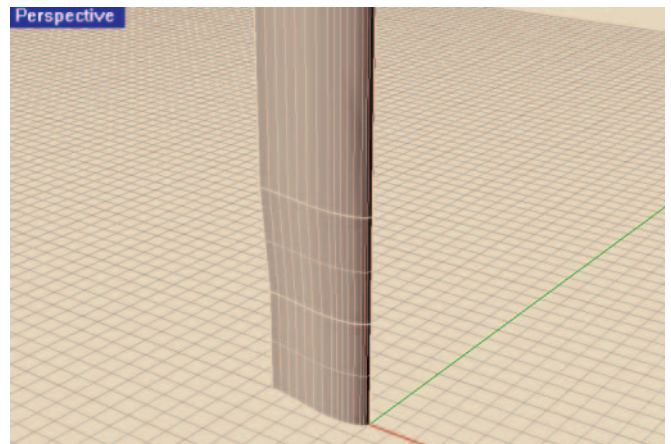


Fig. 4. The computational model of the rudder without any additional elements

The computational domain (Fig. 5) was so arranged as to make it possible to assume different inlet angles of waterflow velocity to the rudder. The upper and lower surface limiting the domain was defined to be the plane of symmetry. The rear surface was defined to be the pressure outlet and the front surface (a half of cylinder) and the side ones constituted the inlet for waterflow velocity to the domain.

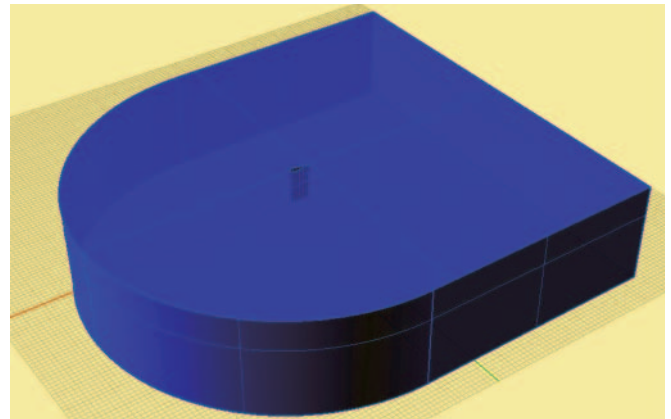


Fig. 5. The computational domain of rudders

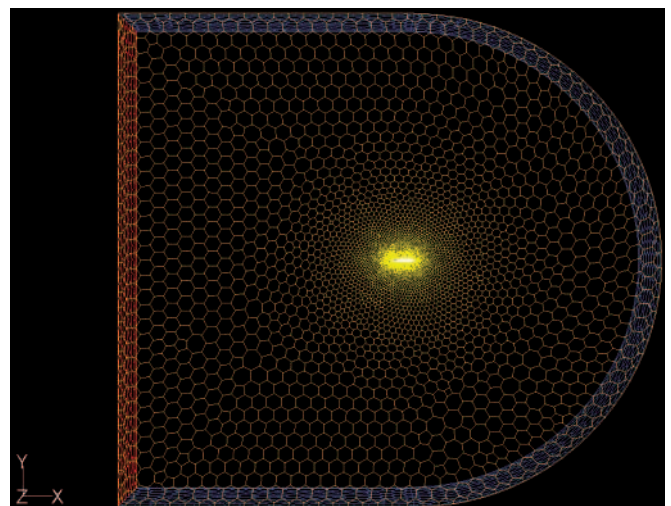


Fig. 6. The computational domain mesh. **Notation:** the blue area – velocity inlet, the yellow one – plane of symmetry, the red one – pressure outlet



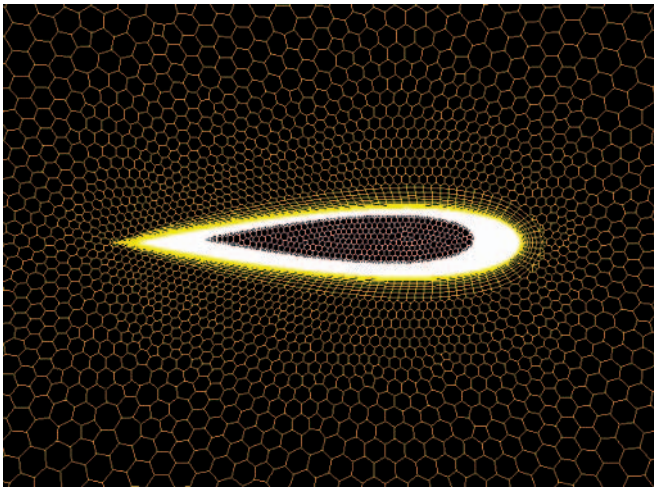


Fig. 7. The structural mesh in the boundary layer (view from the top of the rudder) Notation: the white area – the surfaces defining the rudder blade.

For the domain a polyhedral mesh (Fig. 6 and 7) refined in the vicinity of the rudder and fitted with structural boundary layer on surfaces modelling the rudder, was used.

### CALCULATIONS FOR THE RUDDERS WITHOUT ANY ADDITIONAL ELEMENTS

The calculations in question were conducted with the use of Fluent system. The example pressure distributions and streamlines for the rudder of IFS58-TR15 profile are presented in Fig. 8, 9 and 10.

In Fig. 11 are presented results of the calculations in the form of the lifting force  $L$  and drag force  $D$  versus rudder angle for the rudders based on the profiles shown in Fig. 1.

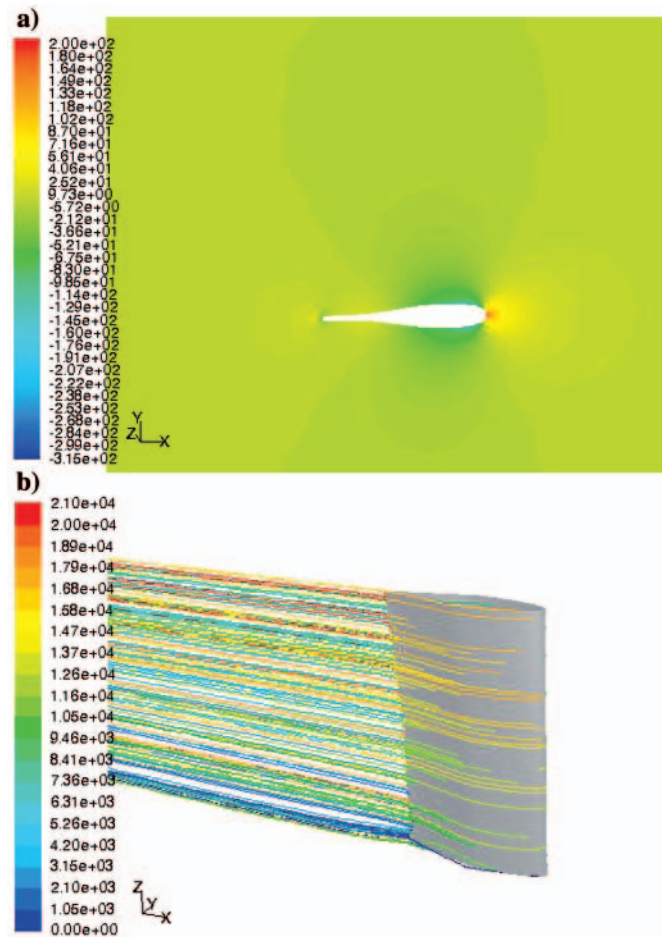


Fig. 8. The pressure distribution: a) and streamlines, b) for  $0^\circ$  angle of attack (the rudder of IFS58-TR15 profile)

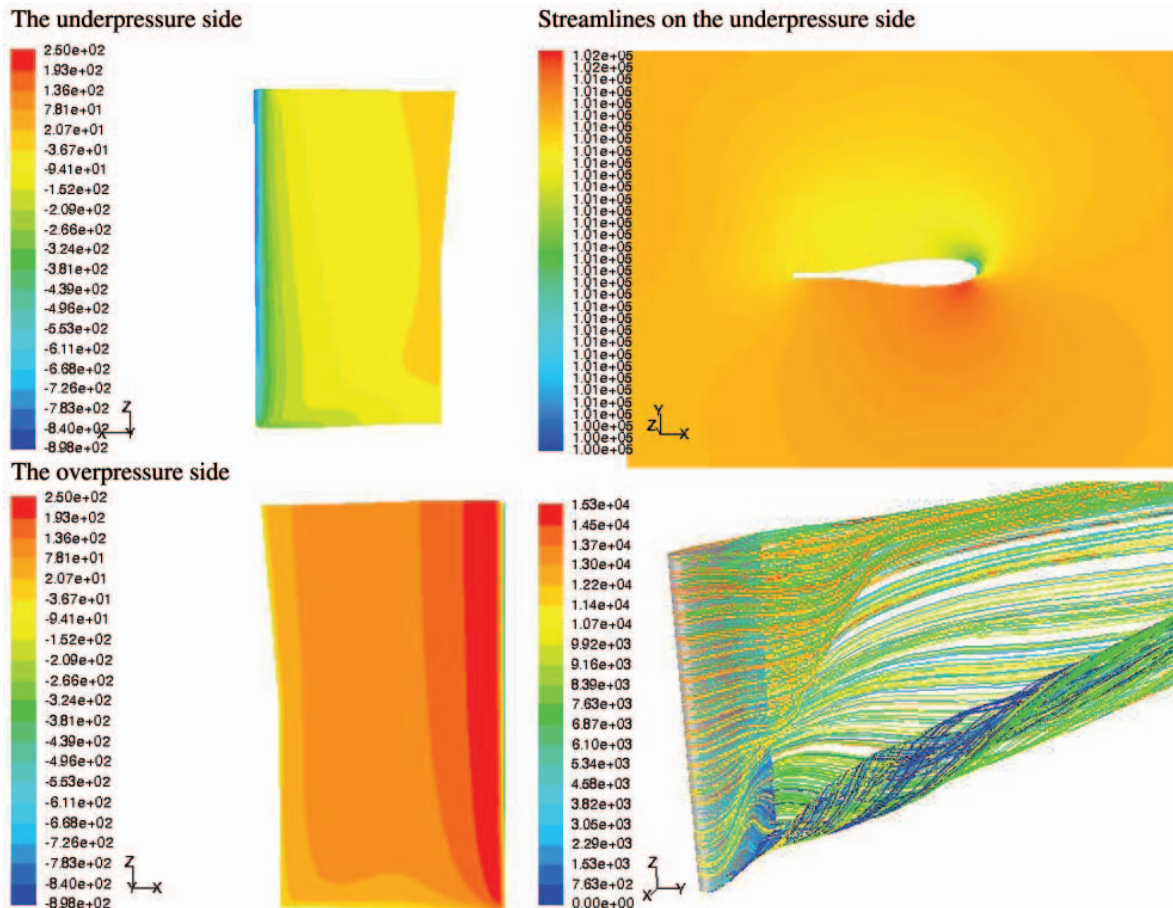


Fig. 9. The pressure distribution and streamlines for  $40^\circ$  angle of attack (the rudder of IFS58-TR15 profile)

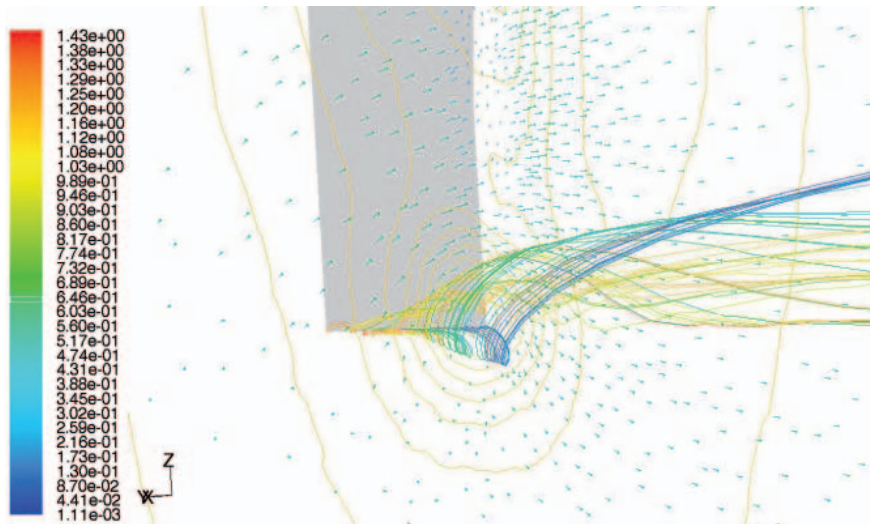


Fig. 10. The tip vortex generated on the rudder of IFS58-TR15 profile at 40° angle of attack. There are depicted streamlines, pressure profiles on iso-surface behind the rudder as well as velocity vectors on the surface

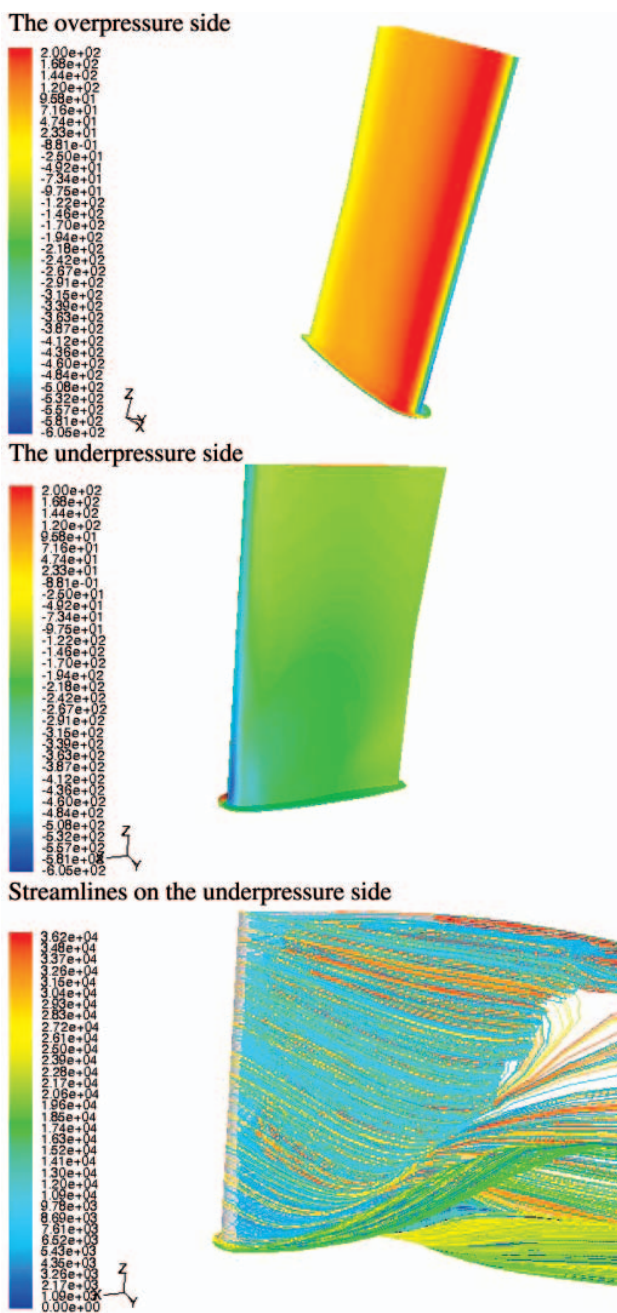


Fig. 12. The pressure distribution and streamlines for the IFS58-TR15 profile rudder at 40° angle of attack

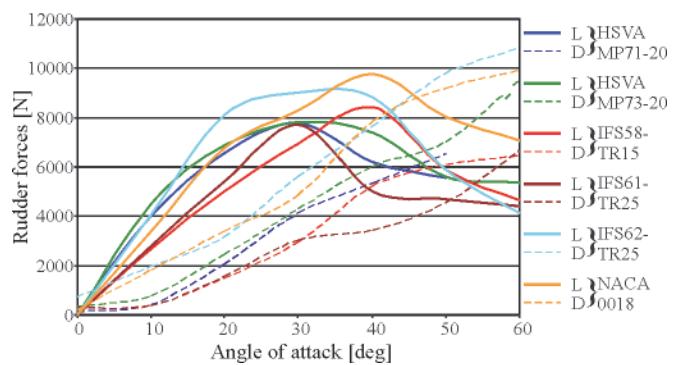


Fig. 11. Values of the lifting force  $L$  and drag force  $D$  versus rudder angle for the considered rudders

## CALCULATIONS FOR THE RUDDERS FITTED WITH ADDITIONAL ELEMENTS

Dimensions of the rudders with additional elements were the same as for the rudders without them. The domain for computation of hydrodynamic forces acting on the modified rudders as well as the scope of the calculations was the same as in the case of the rudders without any modification. The pressure distributions and streamlines for the Schilling rudder of IFS58-TR15 profile are presented in Fig. 12.

The calculation results of the lifting force  $L$  and drag force  $D$  are presented in Fig. 13 for the NACA 0018 profile rudder fitted with the additional flap, and in Fig. 14 – for the Schilling rudder of IFS58-TR15 profile.

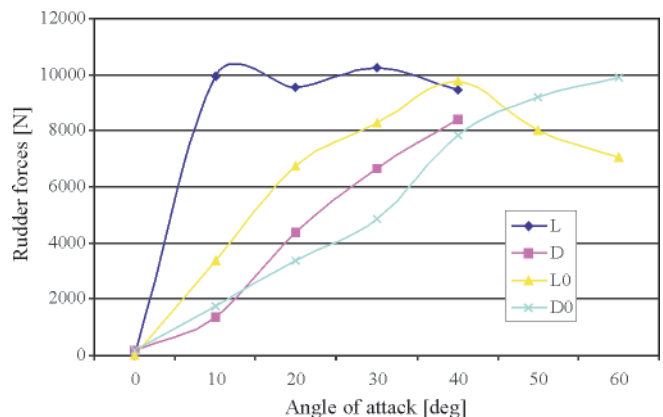


Fig. 13. The hydrodynamic characteristics of the rudder of NACA0018 profile. **Notation:**  $L$ ,  $D$  – for rudder with flap;  $L_0$ ,  $D_0$  – for standard rudder



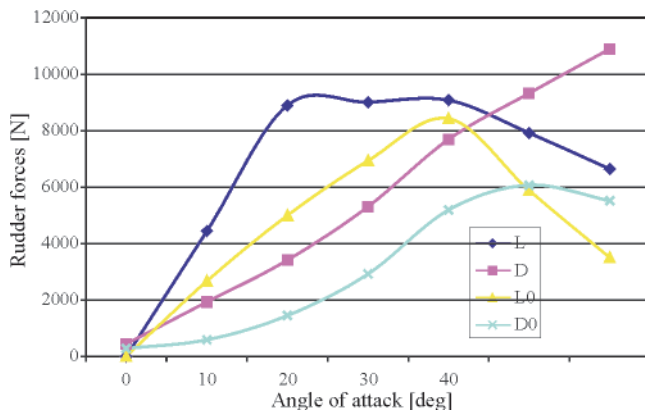


Fig. 14. The hydrodynamic characteristics of the rudder of IFS58-TR15 profile. Notation: L, D – for Schilling rudder; L0, D0 – for standard rudder

## CONCLUSIONS

1. The performed numerical experiment was aimed at demonstration of high usefulness of CFD methods in investigating and designing the streamline rudders. The calculations performed for rudders of different profiles showed how far selection of a profile is important for a designed ship to which various requirements concerning its manoeuvrability or limitations imposed on its rudder, may be assigned. The achieved results can be assessed only qualitatively (by comparing hydrodynamic characteristics for particular profiles) because results of model tests of the rudder installed on B 573 ship were lacking. There are available results of model tests of foils of given profiles but having a very large aspect ratio. However in the case in question the rudders of strictly determined dimensions have been analyzed.
2. The two modified rudders analyzed in the second phase of the numerical experiment revealed much more favourable characteristics in contrast to the same rudders without any modification – however the obtained results should be considered rather qualitative, but not quantitative ones as additional investigations should be performed to obtain more exact results. In spite of that the quantitative changes have been found in line with expectations.

3. The performed analysis showed that the NACA0018 profile rudder fitted with the flap has much more favourable characteristics at small values of rudder angle. Probably, at smaller values of flow velocity in the whole domain and at its large values in the surrounding of the rudder behind the propeller, the rudder has curved the flow behind the propeller changing direction of thrust, in consequence. Such situation can happen during ship's manoeuvres at a very small (or even zero) speed of the ship.
4. The Schilling rudder, i.e. the modified rudder of IFS 58-TR15 profile, exhibits also more favourable characteristics mainly at small values of angle of attack. The difference can be also observed at the angle values close to separation of flow where run of the characteristics is more stable than in the case of the standard rudder. This results from a reduced tip vortex effect; however, as observed in Fig. 12, the tip vortex has not been fully removed.
5. In the drawings of this paper only certain examples of the performed computations of pressure distribution and streamlines, have been presented. The complete set of results of numerical analyzes in question can be found in the final report on the R&D project [2].

## BIBLIOGRAPHY

1. Syrocki W.: *Ship B 575: Results of the Model Tests*. Ship Design and Research Centre, Technical Report No. RH-96/T-023A, Gdańsk 1995
2. Szlangiewicz T.: *Numerical investigations of rudder/propeller/ship stern interaction aimed at improving transport ship's propulsion and manoeuvrability qualities* (in Polish). Final report of the R&D project No. R 10 008 01, Szczecin 2009.

## CONTACT WITH THE AUTHORS

Tomasz Abramowski, Ph. D.  
 Tadeusz Szlangiewicz, Prof.  
 West Pomeranian University of Technology, Szczecin  
 Faculty of Marine Technology  
 Al. Piastów 41  
 71-065 Szczecin, POLAND  
 e-mail: tadeusz.szlangiewicz@ps.pl

# A fatigue life calculation method for structural elements made of D16CzATW aluminium alloy

Józef Szala, Prof.  
Grzegorz Szala, Ph. D.  
University of Technology and Life Science, Bydgoszcz

## ABSTRACT

*In the calculating of fatigue life of structural elements the methods based on hypotheses of fatigue damage summation are commonly applied. In using the methods, apart from choice of an appropriate hypothesis, it is necessary to know a loading spectrum which usually constitutes a set of sinusoidal cycles of variable parameters ( $S_a$ ,  $S_m$ ), as well as fatigue characteristics in the form of Wöhler fatigue diagram, as a rule. Knowledge of the above mentioned data is low during structural design process as designed material objects and possibility of performing measurements are lacking.*

*Hence in this work a calculation method of fatigue life of structural elements, based on the relations between fatigue life diagrams determined in constant-amplitude conditions (Wöhler diagrams) and those obtained under programmed or random loads, is described. The proposed method was experimentally verified by using results of fatigue tests on structural elements made of D16CzATW aluminium alloy.*

**Keywords:** fatigue life, structural elements, D16CzATW aluminium alloy

## INTRODUCTION

Lack of a coherent theory of fatigue process of materials including metals and their alloys makes that for engineering applications are used phenomenological hypotheses on summation of damages, whose description can be found a.o. in the monographs [1] and [2]. Out of many hypotheses, the oldest hypothesis, most comprehensively verified and commonly used is that based on linear summation of fatigue damages, given by Palmgren and Miner (P-M). In many cases its experimental verification showed a low conformity between results of fatigue life calculations and experimental tests, that has resulted in undertaking further efforts to elaborate new calculation methods [3, 4, 5, 6]. For the calculations with the use of the damage summation hypotheses it is necessary to know additionally operational loads (stresses or strains) given in the form of loading spectra, as well as an appropriate fatigue diagram. Such loading spectra are elaborated by applying the cycle - counting methods described in [7], in order to obtain a set of sinusoidal cycles equivalent, as regards fatigue life, to random loading. The third item necessary for the calculations is a Wöhler fatigue diagram of parameters appropriate to a type of loading spectrum. The diagram can be determined experimentally or, if not possible, selected from catalogues or literature sources [8, 9]. Out of the above mentioned main elements of the calculating algorithm, the largest uncertainty is associated with the fatigue damage summation hypothesis. Experimental verification of P-M hypothesis, performed by

means of a few hundred tests revealed the difference between results of the experiments and calculations ranging from 0,3 to 30-fold [10, 11]. The drawbacks of the method have been very clearly felt in structural design process where accurate data on operational loads, material cyclic properties and damage summation hypothesis, are lacking.

It is then necessary to elaborate, excepting damage summation hypothesis, a simple calculation method based on assessment of main loading spectrum parameters and basic cyclic properties of material. To the above mentioned conditions corresponds the method based on statistical relations between fatigue life determined under sinusoidal load conditions (described by Wöhler diagram) and that determined under random load conditions or programmed ones (described by Gassner diagram).

As observed in the fatigue life tests of structural elements under programmed load conditions (block spectra, usually) corresponding to operational loading, their test results depended on a level of variable loads and shape of loading spectra. Such relationship for steel elements was demonstrated in [10] and [12], and for aluminium elements - in [13]. The problem was also described in the monograph of Haibach [14] and the information bulletins of Germanischer Lloyd Group, a ship classification society, [15] and [16].

As proved in the experimental verification of the calculation method based on statistical relations between Wöhler and Gassner diagrams, performed on steel specimens and structural elements, the calculation results obtained with its use, have been



closer to results from experimental tests than those achieved from the calculations to which Palmgren-Miner hypothesis on damage summation was applied, [17].

In the work [17] was analyzed an influence of a shape of loading spectrum on results of experimental verification of calculation method of fatigue life of steel specimens and elements.

This work is aimed at extending the method onto aluminium-alloy elements, in which data determined from plain specimens are applied to calculation of geometrically notched elements and structural elements.

## FORMULATION OF THE PROBLEM

The method proposed in this paper is based on the following assumptions:

- damage cumulation process is qualitatively independent on loading spectrum,
- fatigue damage cumulation depends quantitatively on parameters of loading spectrum (its shape and maximum load),
- constant-amplitude loading is a special case of loading spectrum elaborated on the basis of random loads, e.g. block spectrum,
- if number of cycles in a loading spectrum (for a specimen or structural element) is reduced to one, then fatigue life diagrams intersect each other in the same point; it means that the spectral form loses its sense,
- for different loading spectra of the same maximum load value, fatigue life of a specimen or structural element depends mainly on a form of a spectrum.

In Fig. 1 the sinusoidal loading, random loading and loading spectra corresponding to them are schematically presented.

Loading spectrum form is characterized by the diagram filling factor calculated from the formula as follows [7]:

$$\zeta = \frac{1}{S_{a\max}} \sum_{i=1}^k S_{ai} t_i \quad (1)$$

which, in relation to the schematic spectrum diagram, is equivalent to the ratio of the areas  $F_1$  (under the block spectrum envelope) to the area of the rectangle having the sides:  $S_{a\max}$  and  $n_c$ . As results from the scheme (b) in Fig. 1 and the formula (1), the spectrum filling factor  $\zeta$  is equal to 1.0 for sinusoidal loading, and for random loading amounts to  $\zeta < 1.0$ . The smaller value of the diagram filling factor the slighter loading conditions for structural element; an example of mutual location of the fatigue-life diagrams for various values of the diagram filling factor is presented in Fig. 2.

The schematic procedure of the calculation complying with the above specified assumptions is presented in Fig. 3. The Wöhler diagram (W) and Gassner diagram (G) which intersect each other in the point  $c = c_0$ , are described by the expressions:

- for the Wöhler diagram:

$$\log S_a = -\frac{1}{m_0} \log N + c_0 \quad (2)$$

- for the Gassner diagram:

$$\log S_{a\max} = -\frac{1}{m} \log N_c + c \quad (3)$$

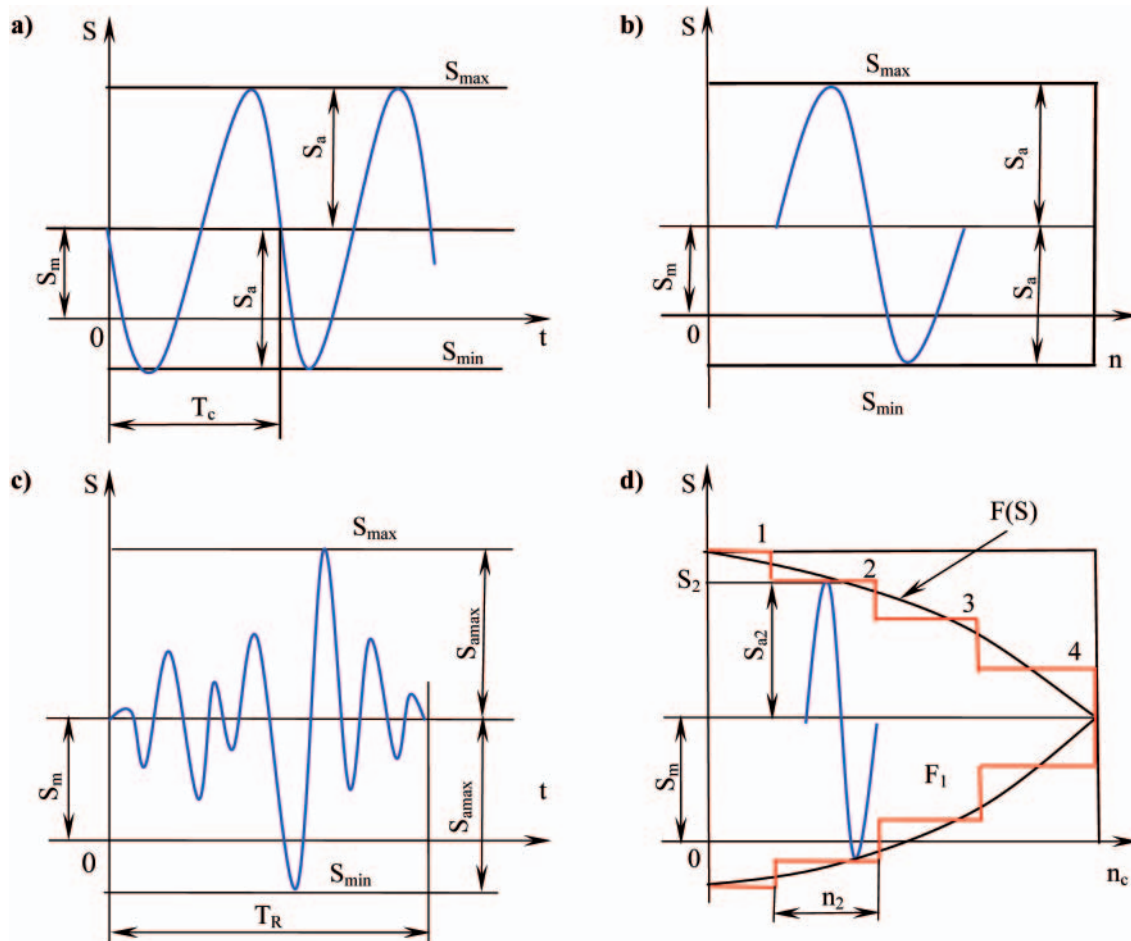


Fig. 1. Schematic loading diagrams and relevant loading spectra: a) sinusoidal loading, b) sinusoidal loading spectrum, c) random loading, d) random loading spectrum

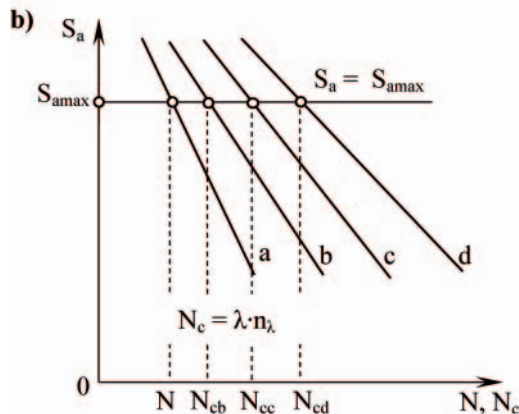
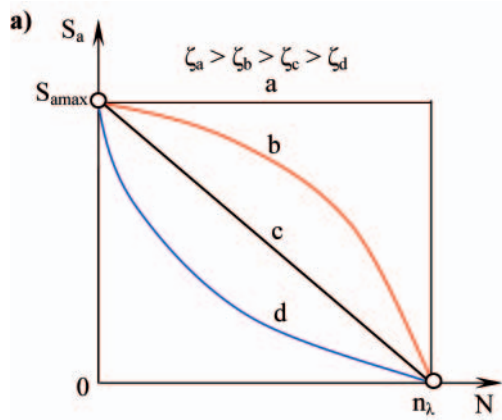


Fig. 2. Schematic diagram of fatigue life dependence on loading spectrum form

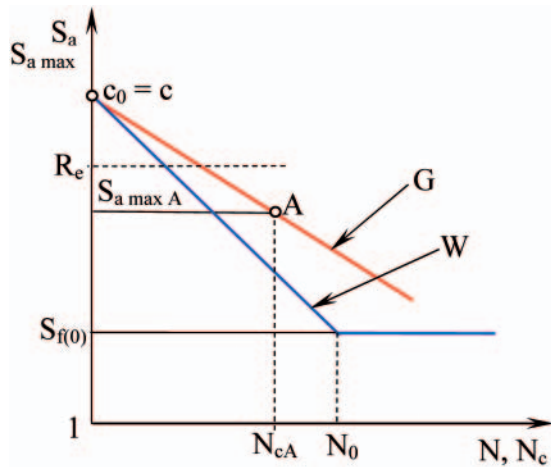


Fig. 3. Schematic diagram for fatigue life calculation

From the scheme of Fig. 3 results the possibility of determining Gassner diagram on the basis of knowledge of Wöhler fatigue diagram and an arbitrary point of the Gassner diagram under determination. The fact is of a great importance for shortening time of tests because it requires to perform programmed fatigue tests (which are time-consuming) for only one point of Gassner diagram (a few fatigue tests at only one, of maximum load, level of the spectrum).

For  $S_{amax} = S_a$  and  $c_0 = c$  1, by comparing the formulae (2) and (3) to each other the following is achieved:

$$\log N_c = \frac{m}{m_0} \log N \quad (4)$$

The relation  $m/m_0$  in function of the diagram filling factor  $\zeta$ , for different kinds of steel specimens and elements, was experimentally determined in the following form, [10, 17]:

$$\frac{m}{m_0} = \zeta^{-r} \quad (5)$$

The power exponent  $r$  is contained within the range of  $0.2 \div 0.4$ . It should be stressed that if one of the lower values of the range is assumed then conservative results (i.e. lower fatigue life values) are obtained.

On determination of  $N$  from the formula describing Wöhler diagram is obtained:

$$N = \left( \frac{C_0}{S_a} \right)^{m_0} \quad (6)$$

and on substitution of the formula (5) to the formula (4) the following is obtained, after transformations:

$$\log N_c = \zeta^{-r} m_0 \log \frac{C_0}{S_{amax}} \quad (7)$$

It should be explained that  $c_0$  which appears in the formula (2), is equal to  $\log C_0$  which appears in the formulae (6) and (7).

The experimental verification of the described calculation method, performed for specimens and bonded structural joints for three values of the diagram filling factor  $\zeta$  (0.34; 0.56 and 0.77), showed a conformity of the results obtained from the calculation in question with those from the tests higher than in the case of the results from the calculation where selected fatigue damage summation hypotheses were applied.

## TESTS AND CALCULATION RESULTS FOR SPECIMENS AND STRUCTURAL ELEMENTS MADE OF D16CZATW ALUMINIUM ALLOY

### Method and program of the tests

From the target of this work the necessity results to perform basic tests aimed at determination of static and cyclic properties of material used for objects to be tested, as well as verification tests of the calculation method of fatigue life of elements under variable random loads.

In the first group of the tests, apart from the monotonic tension test, Wöhler fatigue diagrams have to be determined, as well as the test aimed at determination of value of the power exponent  $r$  appearing in the formula (5), has to be performed with the use of plain specimens under random loading conditions.

The determination method of value of the power exponent  $r$  results from Fig. 3. For tests under random or programmed loading it is enough to have a Wöhler diagram, to determine a point on Gassner fatigue-life diagram, the point A in Fig. 3, and, to form a complete Gassner's diagram of fatigue life by drawing the straight line containing the points A and c.

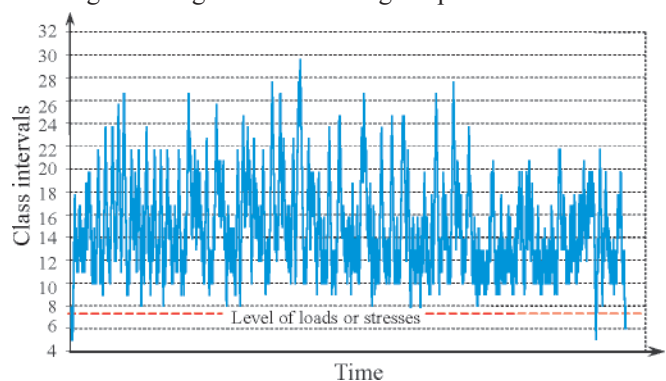


Fig. 4. Random loading assumed for the tests, according to the publication [18]

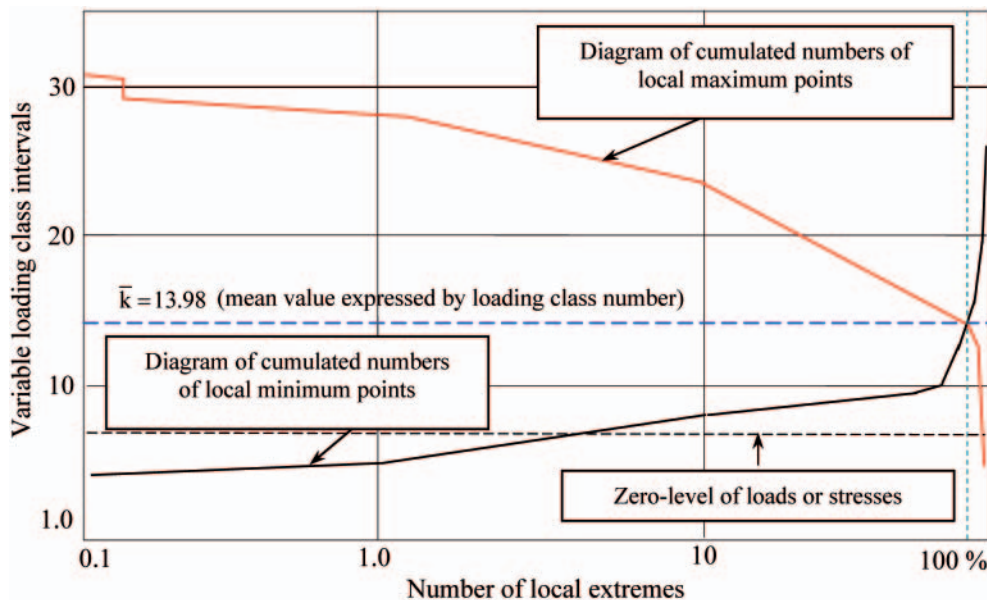


Fig. 5. Loading spectrum for the random loading of Fig. 4, obtained by using the method of counting local extremes

### Variable loading and its spectrum

As an example operational loading the data contained in the publication FALSTAFF-130 [18] were taken. Its graphical form is shown in Fig. 4, and Fig. 5 contains its spectrum achieved by applying the local extremes counting method [7]. On the ordinate axis of the loading diagram, in compliance with the assumption of the FALSTAFF project, are given class intervals within which local extremes have been counted. Such approach to loading spectrum makes performing the tests on various levels of the maximum stress  $S_{max}$ , easier, necessary to determine fatigue life diagram for a tested object. The tests were conducted on a few levels of the maximum stress  $S_{max}$  of the spectrum. The spectrum filling factor calculated from the formula (1) was equal to  $\zeta = 0.375$ .

### The testing objects

The testing objects made of D16CzATW aluminium alloy are shown in Fig. 6. Their basic mechanical properties including cyclic ones were determined with the use of the flat unnotched (plain) specimens whose shape and dimensions are given in Fig. 6a. The tests for verification of the calculation method in question were conducted on the plate specimens with rivet holes, Fig. 6b, as well as on the riveted structural element, Fig. 6c. The

chemical composition of D16CzATW alloy of which the tested objects were manufactured, is given in Tab. 1.

### Results of the tests

The monotonic tension test was conducted on the standard specimens acc. PN-EN 10002-1+AC1 standard (Fig. 6a) with the use of Instron 8502 test machine equipped with suitable instruments and programs. The test results are presented in Tab. 2.

In Tab. 3 are given the data concerning fatigue properties of D16CzATW aluminium alloy in the range of high-cyclic fatigue (HCF) under sinusoidal pulsating load conditions.

The complete Wöhler's diagram for the plain specimens, together with the depicted points of experimental results, is presented in Fig. 7.

The pulsating load conforms the best to the operational load assumed for the tests in question (Fig. 4).

### Experimental determination of value of the power exponent $r$

In order to obtain a value of the power exponent  $r$  the experiment was performed in compliance with the method above described in p. 3.1. To this end, the tests were conducted

Tab. 1. Chemical composition of D16CzATW aluminium alloy

Alloy	Cu	Mg	Mn	Zn(*)	Fe(*)	Si(*)	Other(*)
D16Cz	3.8 ÷ 4.9	1.2 ÷ 1.8	0.3 ÷ 0.9	0.1	0.3	0.2	0.05
Pure alloy (Cz). clad with AD1plating of normal thickness (A). in supersaturated and natural ageing state (T). intended for covering (W)							

Tab. 2. Static properties of plates made of D16CzATW aluminium alloy

Rm [MPa]	Re [MPa]	Rm [MPa]	E [MPa]	A [%]	Z [%]
460	336	613	68402	25.2	28.1

Tab. 3. Cyclic properties of plates made of D16CzATW aluminium alloy

Load	Wöhler equation		Fatigue limit [MPa]	Limit number of cycles
Pulsating R = 0	$S^m N = C$	$m = 5.3107$ $C = 2164.7$	$S_{r(0)} = 113.2$	$N = 6.4 \cdot 10^6$



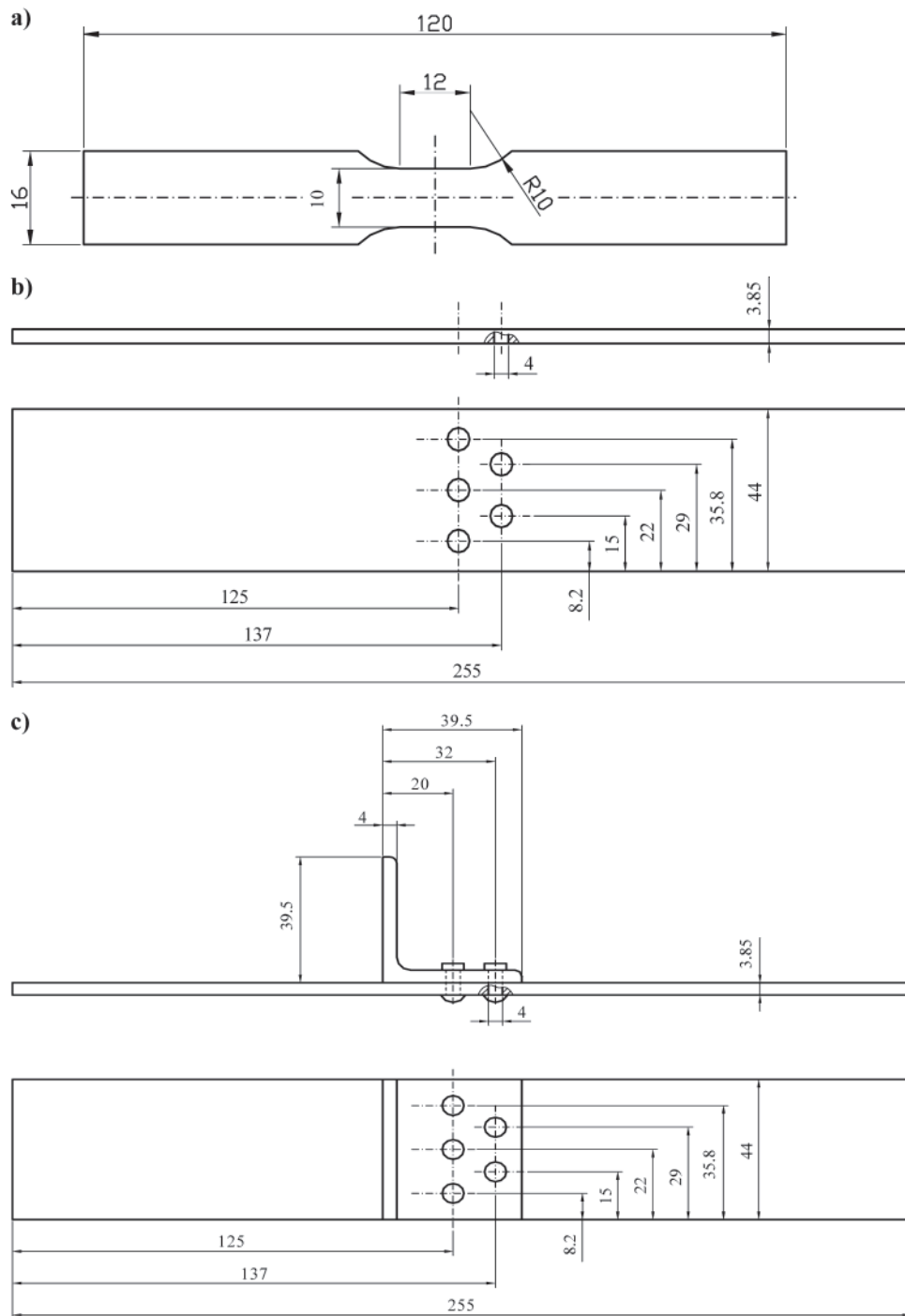


Fig. 6. The tested objects: a) the plain specimen prepared acc. PN-74/H-04327 standard, b) the specimen with rivet holes, c) the riveted structural element

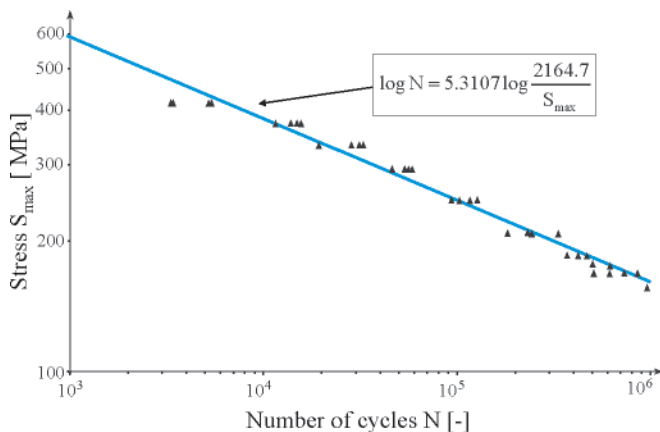


Fig. 7. Wöhler diagram for D16CzATW aluminium alloy, determined under pulsating stress conditions ( $R = 0$ )

on six specimens under random loading conditions (Fig. 4) on the mean level of the maximum stress  $S_{\max A} = 350$  [MPa]. The fatigue-life test results are presented in Tab. 4. The mean fatigue life value amounts to  $N_c = 0,953$ .

By transforming the formulae (4) and (5) the following is obtained:

$$\zeta^r = \frac{\log N}{\log N_c} \quad (8)$$

hence:

$$r = \log \left( \frac{\log N}{\log N_c} \right) \cdot \frac{1}{\log \zeta} \quad (9)$$

For  $S_{\max A} = 350$  [MPa],  $m = 5.3107$ , and  $C = 2164.7$  [MPa] (Tab.3), from the formula (6)  $N = 1.56 \cdot 10^4$  is calculated.

Tab. 4. Results of the fatigue-life tests under random loading conditions, for the stress value  $S_{max} = 350$  [MPa]

No. of specimen	1	2	3	4	5	6	Mean fatigue life value $N_c$
Fatigue life $N_{Ci}$	1.183	0.71	0.864	0.715	1.031	1.215	0.953

As results from the data contained in p. 3, the spectrum filling factor amounts to  $\zeta = 0.375$ .

On substitution of the above mentioned data to the formula (9)  $r = 0.36$  is obtained.

The value is contained within the variability limits  $r = 0.2 \div 0.4$  determined for steel specimens and elements, [10].

### Experimental verification of results of fatigue life calculation

#### Fatigue life calculations and tests of plain specimens

Comparison of results of calculations with those of fatigue life tests on the plain specimens made of D16CzATW alloy is mainly aimed at verification of the calculation method assumptions formulated in p. 2 of this work, throughout the whole variability range of the stresses  $S_{max}$  in the loading spectrum.

The following data were assumed for the calculations:

- the spectrum filling factor – in accordance with p. 3.2:  $\zeta = 0.375$
- the power exponent – in accordance with p. 3.5:  $r = 0.36$
- the Wöhler diagram – in accordance with the data of Tab. 3 - described by the formula:

$$\log N = 5.3107 \log \frac{2164.7}{S_{max}} \quad (6a)$$

The formula (7) for fatigue life calculation takes the form:

$$\log N_c^{obl} = 1.4235 \cdot \log N \quad (4a)$$

Results of the calculations are presented in Tab. 5, row 4 and 5.

The tests of the plain specimens made of D16CzATW alloy were performed under the random load conditions described in p. 3.2. The tests were conducted on 30 specimens, for 9 loading levels, namely: 450, 440, 400, 360, 350, 320, 300, 280 and 250 [MPa].

Results of the tests together with the Gassner diagram based on them are presented in Fig. 8.

The diagram is described by the formula:

$$\log N_c^{ex} = 7.4184 \log \frac{2248}{S_{max}} \quad (10)$$

Results of the calculations of  $N_c^{ex}$  values from the formula (10) for selected levels of  $S_{max}$ , are presented in Tab. 5, row 6 and 7.

Tab. 5. Results of the fatigue life calculations and tests of the plain specimens made of D16CzATW alloy

1.	$S_{max}$	150	200	250.4	300	350
2.	Log N	6.1443	5.4823	4.9687	4.5490	4.1944
3.	N	$1.4 \cdot 10^6$	$3.036 \cdot 10^5$	$9.3 \cdot 10^4$	$3.54 \cdot 10^4$	$1.56 \cdot 10^4$
4.	$\log N_c^{obl}$	8.7427	7.8041	7.0729	6.4755	5.9707
5.	$N_c^{obl}$	$5.53 \cdot 10^8$	$6.37 \cdot 10^7$	$1.18 \cdot 10^7$	$2.99 \cdot 10^6$	$9.35 \cdot 10^5$
6.	$\log N_c^{ex}$	8.7001	7.7759	7.0588	6.4728	5.9777
7.	$N_c^{ex}$	$5.014 \cdot 10^8$	$5.97 \cdot 10^7$	$1.1 \cdot 10^7$	$2.87 \cdot 10^6$	$9.5 \cdot 10^5$

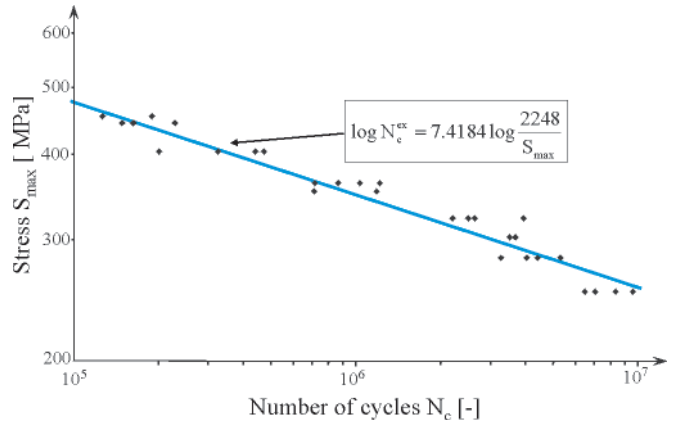


Fig. 8. Gassner fatigue life diagram (a) for plain specimens made of D16CzATW aluminium alloy

Comparison of the Gassner diagrams determined on the basis of the calculations and tests is shown in Fig. 9.

From the diagrams of Fig. 9 result only slight differences between the calculated fatigue life and the experimentally determined. The relative deviation calculated from the formula (11) amounts – in extreme cases – to:  $\delta_N = 5.4\%$  for  $S_{max} = 450$  [MPa],  $\delta_N = 10\%$  for  $S_{max} = 150$  MPa.

$$\delta_N = \frac{N_c^{ex} - N_c^{obl}}{N_c^{ex}} \cdot 100\% \quad (11)$$

The  $\delta_N$  values which do not exceed 10% in relation to the results of the fatigue life calculations, should be considered very small. The very high calculation accuracy results mainly from the way of determining the power exponent  $r$  in the formula (8) on the basis of the experiment for the mean values of  $S_{max}$ . However this analysis is aimed at showing that in the whole  $S_{max}$  variability range from 150 to 450 [MPa] the assumptions for the calculation method are correct.

#### Fatigue life calculations and tests of the notched specimens (acc. Fig. 6b)

The analysis described in this point is mainly aimed at demonstrating that the data concerning the exponent  $r$  determined from standard plain specimens can be used as the basis for the calculations in the case of notched specimens and complex structural elements.

The testing and calculating methods are the same as in p. 3.6a, it means that Wöhler fatigue diagram, loading spectrum

Plain specimen, material: D16CzATW aluminium alloy

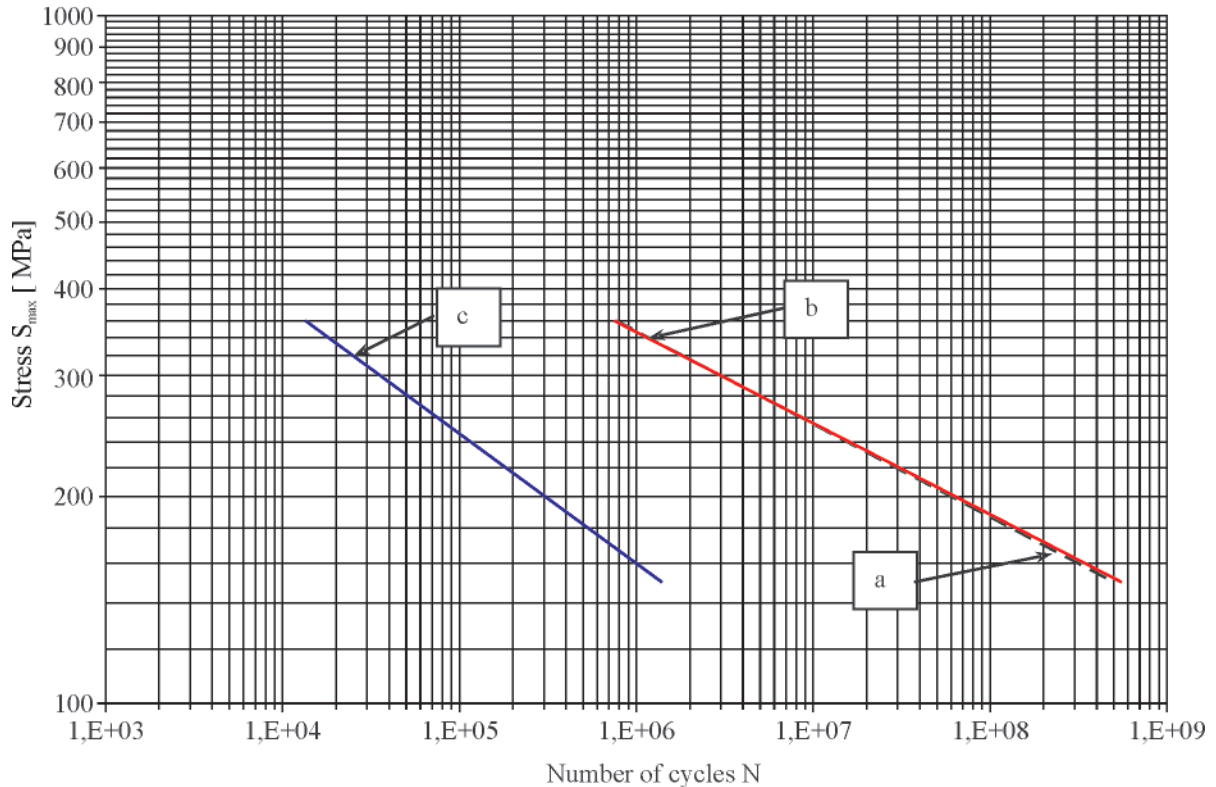


Fig. 9. Fatigue life diagrams for plain specimens made of D16CzATW aluminium alloy: **a)** experimentally determined under random loading conditions, **b)** based on calculations acc. formula (4a), shown against the Wöhler diagram **c)**

parameters as well as values of the power exponent  $r$  constitute the basis for the calculations. The experimental tests of the elements were conducted under the random loading conditions described in p. 3.2.

The Wöhler fatigue diagram for the plate with rivet holes, made of D16CzATW aluminum alloy, is shown in Fig. 10.

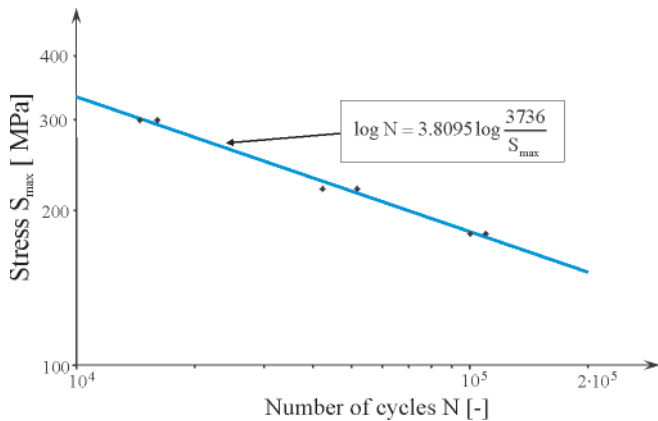


Fig. 10. The Wöhler fatigue diagram for the plate with rivet holes (acc. Fig.6b), made of D16CzATW aluminum alloy

The diagram is described by the formula:

$$\log N = 3.8095 \cdot \log \frac{3736}{S_{\max}} \quad (12)$$

Results of the fatigue life tests under operational loading are shown in the Gassner diagram form in Fig. 11, and the formula (13) provides its description.

Fig. 11. The Gassner fatigue diagram for the plate with rivet holes (acc. Fig.6b), made of D16CzATW aluminum alloy

$$\log N_c^{\text{ex}} = 4.052 \log \frac{9080}{S_{\max}} \quad (13)$$

The results of the calculations and tests are collected in Tab. 6, like in the case of the plain specimens. The data given in the row 4 and 5, Tab. 6, were calculated on the basis of the formula (4a).

The results of the calculations and tests given in Tab. 6 are graphically presented in the diagrams of Fig. 12.

The maximum relative differences between the calculation and test results, determined from the formula (11) amount to:  $\delta_N = -124\%$  for  $S_{\max} = 150$  [MPa], and  $\delta_N = 42\%$  for  $S_{\max} = 400$  [MPa].

Tab. 6. Results of the fatigue life calculations and tests of the plates with rivet holes (acc. Fig.6b), made of D16CzATW alloy

1.	$S_{\max}$	150	200	250	300	350
2.	Log N	5.3193	4.8433	4.4741	4.1725	3.9174
3.	N	$2.9 \cdot 10^5$	$6.97 \cdot 10^4$	$2.98 \cdot 10^4$	$1.49 \cdot 10^4$	$8.27 \cdot 10^3$
4.	$\log N_c^{\text{obl}}$	7.5720	6.8944	6.3689	5.9396	5.5764
5.	$N_c^{\text{obl}}$	$3.73 \cdot 10^7$	$7.84 \cdot 10^6$	$2.34 \cdot 10^6$	$8.7 \cdot 10^5$	$3.77 \cdot 10^5$
6.	$\log N_c^{\text{ex}}$	7.2206	6.7144	6.3217	6.0008	5.7296
7.	$N_c^{\text{ex}}$	$1.66 \cdot 10^7$	$5.18 \cdot 10^6$	$2.1 \cdot 10^6$	$1.0 \cdot 10^6$	$5.36 \cdot 10^5$



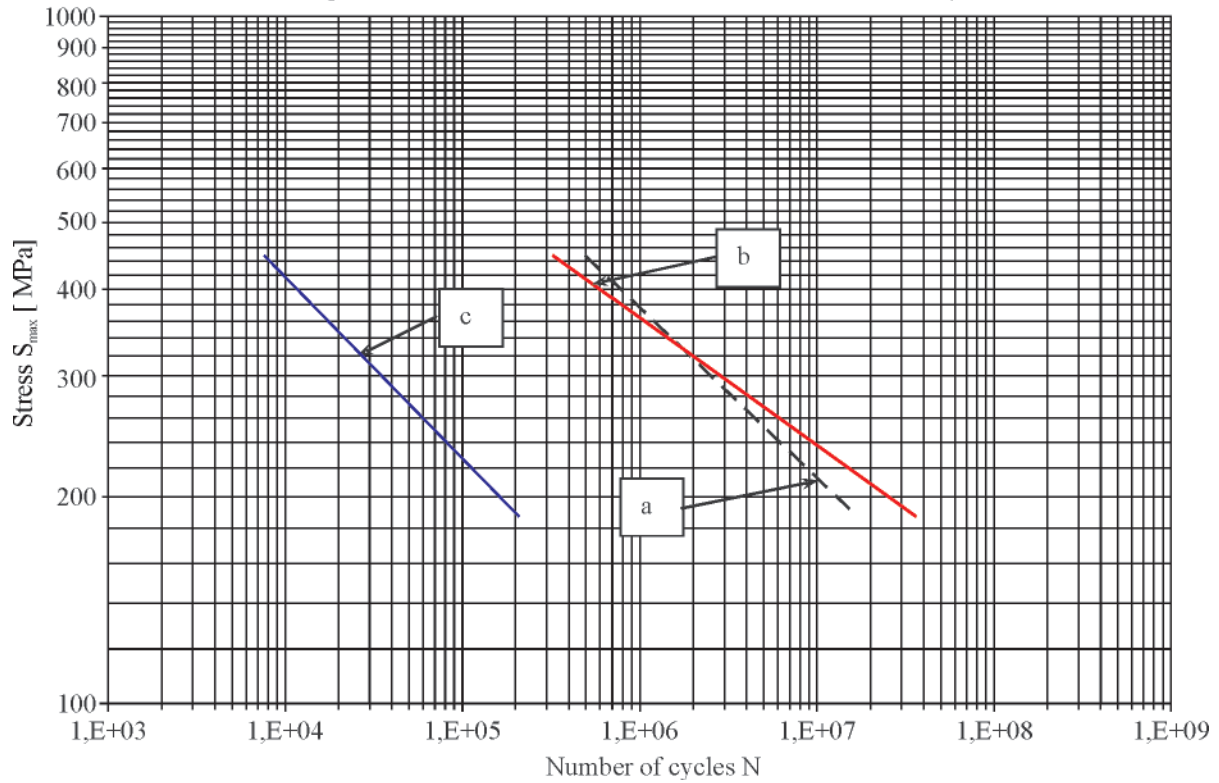


Fig. 12. Results of the fatigue life calculations and tests of the plates with rivet holes (acc. Fig. 6b), made of D16CzATW aluminum alloy: a) experimentally determined under random load conditions, b) based on the calculations, shown against the Wöhler diagram (c)

The above presented differences in the results of fatigue life analysis are relatively small as compared with the results available by means of other methods.

**Fatigue life calculations and tests of the riveted elements (acc. Fig. 6c)**

As the run of calculations and tests of the plates with rivet holes and the riveted elements is identical, in this point only the relevant formulae, diagrams and table are included.

In Fig. 13 the Wöhler diagram for the riveted element acc. Fig. 6c is presented, and in Fig. 14 – the results of the tests under operational loading conditions.

The diagrams of Fig. 13 and 14 are respectively described as follows:

- the Wöhler diagram

$$\log N = 5.048 \log \frac{2154.8}{S_{\max}} \quad (14)$$

- the Gassner diagram

$$\log N_c^{\text{ex}} = 4.529 \log \frac{6912}{S_{\max}} \quad (15)$$

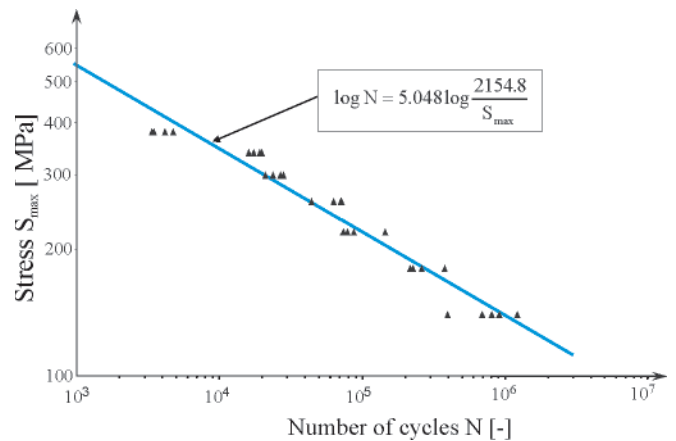


Fig. 13. The Wöhler diagram for the riveted element (acc. Fig. 6c) made of D16CzATW aluminum alloy

The fatigue life according to the proposed method was calculated by using the formula (4a).

In the diagrams of Fig. 15 the results of the calculations and tests given in Tab. 7 are graphically compared with the Wöhler diagram.

Tab. 7. Results of the fatigue life calculations and tests of the riveted elements (acc. Fig.6c), made of D16CzATW alloy

1.	$S_{\max}$	150	200	250	300	350
2.	Log N	5.8421	5.2114	4.7222	4.3225	3.9846
3.	N	$6.9 \cdot 10^5$	$1.6 \cdot 10^5$	$5.3 \cdot 10^4$	$2.1 \cdot 10^4$	$9.65 \cdot 10^3$
4.	$\log N_c^{\text{obl}}$	8.3162	7.4184	6.7220	6.1530	5.6721
5.	$N_c^{\text{obl}}$	$2.07 \cdot 10^8$	$2.6 \cdot 10^7$	$5.27 \cdot 10^6$	$1.4 \cdot 10^6$	$4.6 \cdot 10^5$
6.	$\log N_c^{\text{ex}}$	7.5340	6.9682	6.5293	6.1584	5.8675
7.	$N_c^{\text{ex}}$	$3.4 \cdot 10^7$	$9.3 \cdot 10^6$	$3.4 \cdot 10^6$	$1.4 \cdot 10^6$	$7.37 \cdot 10^5$

## SUMMARY

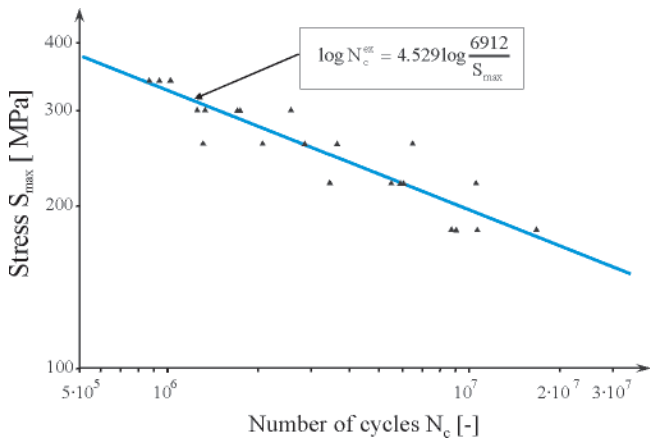


**Fig. 14.** The Gassner fatigue life diagram for the riveted element (acc. Fig. 6c) made of D16CzATW aluminum alloy

As results from the comparison, the greatest differences between the experimentally determined fatigue life and that calculated appear at the ends of the stress range used for the analysis in question. The relative values of the differences calculated according to the formula (11) amount to:  $\delta_N = 0.37$  for  $S_{max} = 250$  [MPa], and  $\delta_N = -5.08$  for  $S_{max} = 150$  [MPa].

The calculated differences for the riveted element are greater than those for the plate with rivet holes. The fact results from the greater spread of results of fatigue life tests of the riveted element which is deemed incommensurably more complex from the point of view of run of fatigue process depending on various factors.

If the spread band of the test results is taken into account on the confidence level of 0.95 then the fatigue life calculation results are contained within the band.

- The discussed calculation method for fatigue life of structural elements, based on statistical relations between the fatigue diagrams determined under constant - amplitude loading conditions (Wöhler diagrams) and those determined under random loading conditions characteristic for operational conditions of structural elements (Gassner diagrams), constitutes an essential contribution to the calculation methods based on phenomenological hypotheses of fatigue damage summation.
- Formulation of the assumptions for the proposed method is described in the publications [2] and [17] which also contain the experimental verification of the method, based on the comparison between the calculation results and those obtained from the tests on steel elements, performed in the loading conditions characterized by different values of the spectrum filling factor  $\zeta$  (0.34; 0.56; 0.77). The crucial conclusion resulting from the analysis is that the analyzed calculation method may be effectively applied to load spectra irrespective of values of their factor  $\zeta$ .
- In this work the applicability analysis of the specimens and structural elements made of the D16CzATW aluminum alloy used in aircraft industry, has been performed. And, its original element, as compared with earlier publications, is the proof that the parameters which appear in the formula for calculating the fatigue life determined from standard specimens, are also applicable to calculations of complex structural elements; the statement mainly concerns value of the power exponent  $r$  appearing in the formulae (5) and (7).
- The comparative analysis of the calculation and experimental test results showed a satisfactory conformity and possible practical application of the proposed method to structural

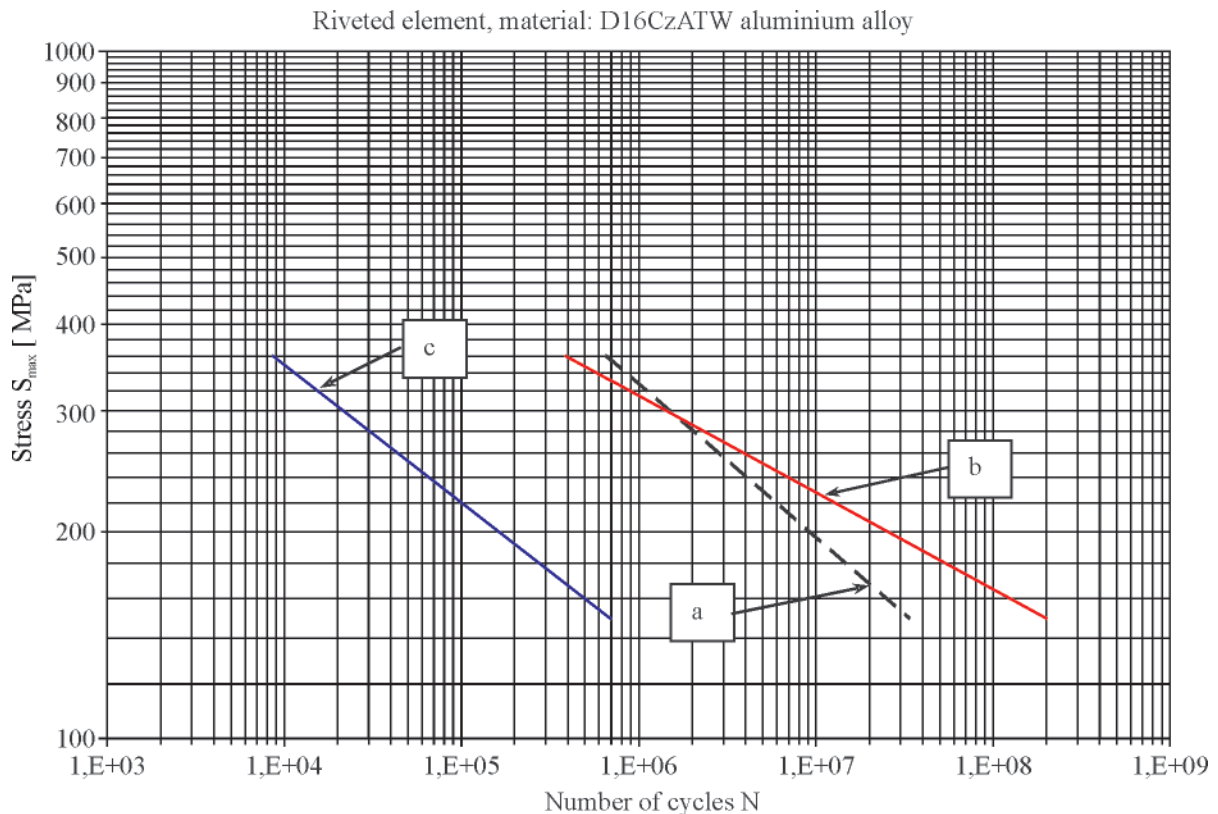


**Fig. 15.** Graphical comparison of the results of the calculations and tests presented in Tab.7: **a)** experimentally determined under random load conditions; **b)** based on the calculations; shown against the Wöhler diagram **c)**

design process when, as real material objects are lacking, only scarce data on operational conditions (data on measured loads) and on design features of such objects (being *in statu nascendi*), are at one's disposal.

*This work has been elaborated in the frame of the research project No. 7 T07B 01018 financially supported by the Ministry of Science and Higher Education.*

## NOMENCLATURE

$\zeta$	– spectrum filling factor
$S$	– stress (general notation), [MPa]
$S_{\max}$	– maximum stress: in a sinusoidal cycle, an analyzed section of random stresses (e.g. a measuring section of operational loading), loading spectrum, or loading programme, [MPa]
$S_{\min}$	– minimum stress: in a sinusoidal cycle, an analyzed section of random stresses (e.g. a measuring section of operational loading), loading spectrum, or loading programme, [MPa]
$S_m$	– mean stress value: in a sinusoidal cycle, an analyzed section of random stresses (e.g. a measuring section of operational loading), loading spectrum, or loading programme, [MPa]
$S_a$	– stress amplitude in a sinusoidal cycle
$S_{ai}$	– stress amplitude in loading cycles: sinusoidal of $i$ -th step, a loading spectrum or loading programme
$i$	– number of a step in a loading spectrum or loading programme
$t_i = \frac{n_i}{n_c} = \frac{n_{\lambda i}}{n_{\lambda c}}$	– fraction of number of $S_{ai}$ - amplitude cycles in total number of cycles appearing in a loading spectrum or programme
$n_i$	– number of $S_{ai}$ - amplitude cycles appearing in a loading spectrum
$n_c$	– total number of cycles within a loading spectrum
$n_{\lambda i}$	– number of $S_{ai}$ - amplitude cycles within a loading programme period
$n_{\lambda c}$	– total number of cycles within a loading programme
$\lambda$	– number of repetitions of a loading programme period up to fatigue fracture
$N$	– number of cycles (general notation)
$N_i$	– number of cycles to fatigue fracture in sinusoidal $S_{ai}$ – amplitude loading conditions
$N_c$	– fatigue life
$F(S)$	– distribution of values of sinusoidal cycles
$m_o$	– parameter in the formulae which describe Wöhler diagram
$C_i m$	– parameters in the formulae which describe Gassner fatigue life diagram, Eq. (3)
$C_o$	– constant value in the formula which describe Wöhler diagram of exponential form
$S_{f(0)}$	– fatigue limit at the stress ratio $R = 0$ (pulsating load)
$\delta_w$	– relative difference between fatigue life test and calculation results (see Eq. (11)).
<b>Indices</b>	
ex	– stands for operational results or values
obl	– stands for calculation results or values.

## BIBLIOGRAPHY

1. Manson S.S., Halford G.R.: *Re-Examination of Cumulative Fatigue Damage Analysis – an Engineering Perspective*. Engineering Fracture Mechanics, Vol.25, No. 5/6, 1986
2. Szala J., Boroński D.: *Material fatigue state assessment in diagnostics of machines and devices* (in Polish). Wydawnictwo ITE-PIB (Publishing House of Institute of the Technology of the Exploitation - State Research Institute), Bydgoszcz, 2008
3. Sevansson T., Johannesson P., de Mare J.: *Fatigue life prediction based on variable amplitude tests-specific applications*. International Journal of Fatigue, 27, 2005
4. Liu Y., Mahadevans S.: *Stochastic fatigue damage modeling under variable amplitude loading*. International Journal of Fatigue, 29, 2007
5. Buch A.: *Prediction of the comparative fatigue performance for realistic loading distributions*. Prog. Aerospace Sci. Vol. 33, 1997
6. Sonsino C.M.: *Fatigue testing under variable amplitude loading*. International Journal Fatigue, 29, 2007
7. Kocańda S., Szala J.: *Essentials of fatigue calculations* (in Polish). PWN (State Scientific Publishing House), Warsaw, 1997
8. *Soprotivlenie ustalosti metalom i splavov*. Kiev Naukowe Dumka, 1987
9. Boyer H. E.: *Atlas of Fatigue Curves*. American Society for Metals (ASM), Ohio, 2003
10. Szala J.: *Fatigue life assessment of machines under random and programmed loading conditions* (in Polish). Monograph, Mechanika 22, Wydawnictwo ATR (Publishing House of Technical Agricultural Academy), Bydgoszcz, 1980
11. Lehman R.: *Über die Gültigkeit der Hypothese der Linearen Schadens – akumulation*. Maschinenbautechnik 5, 1970
12. Haibach E.: *Probleme der Betriebsfestigkeit von metalischen Konstruktionsteilen*. VDI- Z133, 1971, Nr 5, 1.297/403
13. Osterman H.: *Die Lebensdauerabschätzung bei Sonderkollektiven*. LBF-Bericht Nr TB-80, 1968
14. Haibach E.: *Betriebs-Festigkeit*. VDI Verlag GmbH, Düsseldorf, 1989
15. Fricke W., Petershagen, Paetzold H.: *Fatigue Strength of Ship Structures, Part I: Basic Principles*. GL-Technology, Information from Germanischer Lloyd Group, Nr 1/97, Hamburg, 1997
16. Fricke W., Petershagen, Paetzold H.: *Fatigue Strength of Ship Structures, Part II: Examples*. GL-Technology, Information from Germanischer Lloyd Group, Nr 1/98, Hamburg, 1998
17. Szala J.: *On a fatigue calculation method for structural elements under stochastic loading conditions* (in Polish). Archiwum Budowy Maszyn (Archive of Machinery Engineering), Vol. XXIX, No. 3÷4, 1982
18. Szala J.: *Selected fatigue-life problems of elements of ship machines and devices* (in Polish). Proc. the Jubilee Scientific Conference: Research & Development – a chance for Polish shipbuilding industry, Ship Design and Research Centre, Gdańsk, 2001.

## CONTACT WITH THE AUTHORS

Józef Szala, Prof.,  
Grzegorz Szala, Ph. D.  
Faculty of Mechanical Engineering,  
University of Technology and Life Science,  
Prof. S. Kaliskiego 7  
85-763 Bydgoszcz, POLAND  
e-mail: jszpkm@utp.edu.pl



# Theoretical and mathematical models of the torque of mechanical losses in a hydraulic rotational motor for hydrostatic drive

Zygmunt Paszota, Prof.  
Gdansk University of Technology

Abstract



*The paper presents theoretical and mathematical models of the torque of mechanical losses in a hydraulic rotational motor with constant capacity  $q_{Mt}$  per one shaft revolution (with constant theoretical working volume  $V_{Mt}$ ) and with variable capacity  $q_{Mgv} = b_M q_{Mt}$  per one shaft revolution (with variable geometrical working volume  $V_{Mgv}$ ). The models are to be used in the laboratory and simulation investigations of motor energy losses aimed at evaluation of the motor energy efficiency and hydrostatic drive efficiency.*

**Keywords:** hydrostatic drive; hydraulic motor; energy efficiency

## INTRODUCTION

The paper is a continuation of references [1÷10], aimed at developing a method of evaluation of the losses and energy efficiency of the hydrostatic drives and displacement machines used in them. The method is based on the theoretical and mathematical descriptions of losses in the pumps, hydraulic motors and in other elements of a hydrostatic drive system.

Description of the hydraulic motor losses and energy efficiency is based on the diagram of the direction of increasing power stream in a rotational hydraulic motor, which is introduced instead of the Sankey diagram (Fig.1 [10]).

The aim of the paper is to present theoretical and mathematical models of torque of mechanical losses in the rotational hydraulic motor „shaft – working chambers” assembly. The motor is a displacement machine with constant theoretical capacity  $q_{Mt}$  per one shaft revolution (with constant motor theoretical working volume  $V_{Mt}$ ) or with variable geometrical capacity  $q_{Mgv} = b_M q_{Mt}$  per one shaft revolution (with variable motor geometrical working volume  $V_{Mgv}$ ).

The models are to be used in the laboratory and simulation investigation of the motor energy losses, motor energy efficiency and hydrostatic drive efficiency.

## THEORETICAL MODELS OF THE TORQUE $M_{Mi}$ OF MECHANICAL LOSSES IN THE MOTOR „SHAFT – WORKING CHAMBERS” ASSEMBLY

Torque  $M_{Mi}$  indicated in the rotational hydraulic motor working chambers must be greater than torque  $M_M$  loading the motor shaft (torque required by the driven machine (device)) because of the necessity of balancing also the

torque  $M_{Mm}$  of mechanical losses in the „shaft – working chambers” assembly. The assembly connects the shaft with working chambers, forms the working chambers and changes their capacity. Therefore, the torque  $M_{Mi}$  indicated in the motor working chambers is a sum of torque  $M_M$  loading the shaft and of torque  $M_{Mm}$  of mechanical losses:

$$M_{Mi} = M_M + M_{Mm} \quad (1)$$

Torque  $M_{Mm}$  of mechanical losses in a rotational hydraulic motor with variable geometrical capacity  $q_{Mgv}$  per one shaft revolution is, with maximum value of  $q_{Mgv}$ , i.e. with  $q_{Mgv} = q_{Mt}$  (with coefficient  $b_M = q_{Mgv}/q_{Mt} = 1$ ), equal to the torque of mechanical losses in the motor working with constant theoretical capacity  $q_{Mt}$  per one shaft revolution. The theoretical and mathematical models describing the torque  $M_{Mm}$  of mechanical losses in the „shaft – working chambers” assembly of a motor with variable capacity  $q_{Mgv}$  per one shaft revolution (with variable  $b_M$  coefficient) may be described with reference to models of the torque  $M_{Mm}$  of mechanical losses in the assembly of a motor with constant capacity  $q_{Mt}$  per one shaft revolution (with  $b_M = 1$ ).

Torque  $M_{Mm}$  of mechanical losses in a rotational hydraulic motor is mainly an effect of friction forces between elements of the „shaft – working chambers” assembly, dependent, among others, on the torque  $M_M$  loading the shaft.

Friction forces between the elements of the „shaft – working chambers” assembly are, to some extent, an effect of loading those elements by inertia forces from the rotational and reciprocating motion, dependent on the shaft rotational speed  $n_M$  and on the motor capacity  $q_{Mgv}$  per one shaft revolution ( $b_M$  coefficient).

There are also friction forces between the „shaft – working chambers” assembly elements and the working fluid, dependent on the fluid viscosity  $\nu$  and on the shaft rotational speed  $n_M$  and also on the motor capacity  $q_{Mgv}$  per one shaft revolution ( $b_M$  coefficient). The impact of working fluid viscosity  $\nu$  on the friction forces between elements of the „shaft – working chambers” assembly and the working fluid is visible mainly in the piston hydraulic motors with casing filled with fluid.

Torque  $M_M$  loading the motor shaft and the shaft rotational speed  $n_M$  required by the driven machine (device) change in the ( $0 \leq \bar{\omega}_M < \bar{\omega}_{Mmax}$ ,  $0 \leq \bar{M}_M < \bar{M}_{Mmax}$ ) hydrostatic drive operating range. The kinematic viscosity  $\nu$  of working fluid (hydraulic oil, oil – water emulsion) changes in the  $\nu_{min} \leq \nu \leq \nu_{max}$  range.

$M_M$ ,  $n_M$  and  $\nu$  are parameters independent of the motor and of the losses in that motor. In models applied to motor with variable capacity  $q_{Mgv} = b_M q_{Mt}$  per one shaft revolution, the change of  $q_{Mgv}$  ( $b_M$ ) is assumed in the  $0 \leq q_{Mgv} \leq q_{Mt}$  ( $0 \leq b_M \leq 1$ ) range, although in fact  $b_{Mmin}$  is of the  $0.2 \div 0.3$  order.

Torque  $M_{Mm|M_M=0, n_M, b_M, \nu}$  of mechanical losses in a hydraulic motor operating with torque  $M_M$  and speed  $n_M$  required by the driven machine (device) (the motor having capacity  $q_{Mgv}$  per one shaft revolution ( $b_M$  coefficient) and fed with working fluid of viscosity  $\nu$ ) can be described as a sum of torque  $M_{Mm|M_M=0, n_M, b_M, \nu}$  and increase  $\Delta M_{Mm|M_M=0, n_M, b_M, \nu}$ ; torque  $M_{Mm|M_M=0, n_M, b_M, \nu}$  of mechanical losses occurs in an unloaded motor (when the torque  $M_M$  required of the motor is equal to zero –  $M_M = 0$ ) and the increase  $\Delta M_{Mm|M_M=0, n_M, b_M, \nu}$  of the torque of mechanical losses is an effect of loading the „shaft – working chambers” assembly elements by the increasing shaft loading torque  $M_M$ :

$$\Delta M_{Mm|M_M=0, n_M, b_M, \nu} = M_{Mm|M_M=0, n_M, b_M, \nu} + \Delta M_{Mm|M_M=0, n_M, b_M, \nu} \quad (2)$$

In constructing the theoretical and mathematical models describing the torque  $\Delta M_{Mm|M_M=0, n_M, b_M, \nu}$  of mechanical losses in a rotational hydraulic motor, an assumption is made that the increase  $\Delta M_{Mm|M_M=0, n_M, b_M, \nu}$  of the torque of the mechanical losses in the „shaft – working chambers” assembly, as an effect of the increasing required torque  $M_M$  loading the motor shaft, is practically independent of:

- required shaft rotational speed  $n_M$ ,
- value of the  $b_M = q_{Mgv}/q_{Mt}$  coefficient of capacity per one shaft revolution,
- working fluid viscosity  $\nu$ .

An assumption was also made in the proposed models, that increase  $\Delta M_{Mm|M_M=0, n_M, b_M, \nu}$  of the torque of the mechanical losses is determined at the speed  $n_M = n_{Mt}$  i.e. equal to the motor shaft theoretical speed, at the coefficient  $b_M = 1$  (with  $q_{Mgv} = q_{Mt}$ ) and at  $\nu = \nu_n$  i.e. working fluid reference viscosity  $\nu_n$ :

$$\begin{aligned} \Delta M_{Mm|M_M=0, n_M, b_M, \nu} &= f(M_M) = \\ &= \Delta M_{Mm|M_M=0, n_{Mt}, b_M=1, \nu_n} \sim M_M \end{aligned} \quad (3)$$

In constructing the theoretical and mathematical models describing the torque  $M_{Mm|M_M=0, n_M, b_M, \nu}$  of mechanical losses in the „shaft – working chambers” assembly it was also assumed that:

- the impact of required shaft rotational speed  $n_M$  and value of the coefficient  $b_M = q_{Mgv}/q_{Mt}$  on the load of the assembly elements with inertia forces,
- the impact of working fluid viscosity  $\nu$ ,  $n_M$  and  $b_M$  on the friction forces between elements and working fluid,

in consequence, the impact of  $n_M$ ,  $b_M$  and  $\nu$  on the torque  $M_{Mm}$  of mechanical losses in the motor can be determined with the shaft loading torque equal to zero ( $M_M = 0$ ), because the inertia forces of the assembly elements and friction forces between the elements and working fluid are independent of the torque  $M_M$  loading the motor shaft:

$$M_{Mm|M_M=0, n_M, b_M, \nu} = f(n_M, b_M, \nu) \quad (4)$$

The above mentioned assumptions allow to describe the torque  $M_{Mm|M_M=0, n_M, b_M, \nu}$  of mechanical losses in the „shaft – working chambers” assembly by a theoretical model in the form:

$$\begin{aligned} M_{Mm|M_M=0, n_M, b_M, \nu} &= M_{Mm|M_M=0, n_M, b_M, \nu} + \\ &+ \Delta M_{Mm|M_M=0, n_M, b_M=1, \nu_n} \end{aligned} \quad (5)$$

In a hydraulic motor with theoretical (constant) capacity  $q_{Mt}$  per one shaft revolution ( $b_M = 1$ ), operating with theoretical (constant) shaft rotational speed  $n_{Mt}$  and the working fluid reference (constant) viscosity  $\nu_n$ , the theoretical model describing the torque of mechanical losses in the assembly takes the form (Fig.1):

$$\begin{aligned} M_{Mm|M_M=0, n_M, b_M=1, \nu_n} &= M_{Mm|M_M=0, n_{Mt}, b_M=1, \nu_n} + \\ &+ \Delta M_{Mm|M_M=0, n_M, b_M=1, \nu_n} \end{aligned} \quad (6)$$

The impact of inertia forces of the „shaft – working chambers” assembly elements performing the rotational and reciprocating motion on the torque  $M_{Mm|M_M=0, n_M, b_M, \nu}$  of mechanical losses in an unloaded motor may be presented as a function of the motor shaft rotational speed  $n_M$  and as a function of geometrical capacity  $q_{Mgv}$  ( $b_M$  coefficient) per one shaft revolution.

The impact of the friction forces between the „shaft – working chambers” assembly elements and the working fluid on the torque  $M_{Mm|M_M=0, n_M, b_M, \nu}$  of the mechanical losses in an unloaded motor may be presented as a function of the working fluid viscosity  $\nu$  and as a function of the motor shaft rotational speed  $n_M$  and of the capacity  $q_{Mgv}$  (coefficient  $b_M$ ) per one shaft revolution.

The proposed theoretical models describing the torque  $M_{Mm|M_M=0, n_M, b_M, \nu}$  of mechanical losses in the „shaft – working chambers” assembly of an unloaded hydraulic motor (with torque  $M_M = 0$ ), with changing shaft speed  $n_M$ , with theoretical (constant) capacity  $q_{Mt}$  ( $b_M = 1$ ) or geometrical (variable) capacity  $q_{Mgv}$  ( $b_M$ ) of the motor per one shaft revolution and with changing working fluid viscosity  $\nu$ , take the form:

- in a hydraulic motor with theoretical (constant) capacity  $q_{Mt}$  ( $b_M = 1$ ) per one shaft revolution (Fig. 2):

$$\begin{aligned} M_{Mm|M_M=0, n_M, b_M=1, \nu} &= M_{Mm|M_M=0, n_M, b_M=1, \nu_n} \left( \frac{\nu}{\nu_n} \right)^{a_{\nu m}} = \\ &= \left( M_{Mm|M_M=0, n_M=0, b_M=1, \nu_n} + \Delta M_{Mm|M_M=0, n_M, b_M=1, \nu_n} \right) \left( \frac{\nu}{\nu_n} \right)^{a_{\nu m}} \end{aligned} \quad (7)$$

where:

$$\begin{aligned} \Delta M_{Mm|M_M=0, n_M, b_M=1, v_n} &= M_{Mm|M_M=0, n_M, b_M=1, v_n} + \\ &- M_{Mm|M_M=0, n_M=0, b_M=1, v_n} = \\ &= (M_{Mm|M_M=0, n_M=n_{Mt}, b_M=1, v_n} - M_{Mm|M_M=0, n_M=0, b_M=1, v_n}) \frac{n_M}{n_{Mt}} \end{aligned} \quad (8)$$

- in a hydraulic motor with geometrical (variable) capacity  $q_{Mgv}$  ( $q_{Mgv} = b_M q_{Mt}$ ) per one shaft revolution (Fig. 5):

$$\begin{aligned} M_{Mm|M_M=0, n_M, b_M, v} &= M_{Mm|M_M=0, n_M, b_M, v_n} \left( \frac{v}{v_n} \right)^{a_{vm}} \\ &= (M_{Mm|M_M=0, n_M=0, b_M=0, v_n} + \Delta M_{Mm|M_M=0, n_M, b_M, v_n}) \left( \frac{v}{v_n} \right)^{a_{vm}} \\ &= (M_{Mm|M_M=0, n_M=0, b_M=1, v_n} + \Delta M_{Mm|M_M=0, n_M, b_M, v_n}) \left( \frac{v}{v_n} \right)^{a_{vm}} \end{aligned} \quad (9)$$

where:

$$\begin{aligned} \Delta M_{Mm|M_M=0, n_M, b_M, v_n} &= M_{Mm|M_M=0, n_M, b_M, v_n} + \\ &- M_{Mm|M_M=0, n_M=0, b_M=0, v_n} = \\ &= M_{Mm|M_M=0, n_M, b_M, v_n} - M_{Mm|M_M=0, n_M=0, b_M=1, v_n} = \\ &= (M_{Mm|M_M=0, n_M=n_{Mt}, b_M=1, v_n} - M_{Mm|M_M=0, n_M=0, b_M=1, v_n}) \frac{n_M}{n_{Mt}} b_M \end{aligned} \quad (10)$$

It is assumed in expressions (9) and (10) that the torque  $M_{Mm|M_M=0, n_M=0, b_M, v_n}$  of mechanical losses in the „shaft – working chambers” assembly of an unloaded hydraulic motor ( $M_M = 0$ ) with geometrical (variable) capacity  $q_{Mgv}$  ( $q_{Mgv} = b_M q_{Mt}$ ) per one shaft revolution and with zero shaft rotational speed ( $n_M = 0$ ) is practically independent of the coefficient  $b_M$  of capacity per one shaft revolution and can be determined for  $b_M = 1$ . Therefore the following simplifying assumption is accepted:

$$\begin{aligned} M_{Mm|M_M=0, n_M=0, b_M=0, v_n} &= M_{Mm|M_M=0, n_M=0, b_M, v_n} = \\ &= M_{Mm|M_M=0, n_M=0, b_M=1, v_n} \end{aligned}$$

In effect, the proposed **theoretical models describing the torque  $M_{Mm}$  of mechanical losses in a hydraulic rotational motor** take the forms:

- in a hydraulic motor with theoretical (constant) capacity  $q_{Mt}$  ( $b_M = 1$ ) per one shaft revolution (Fig. 3):

$$\begin{aligned} M_{Mm|M_M, n_M, b_M=1, v} &= \left[ M_{Mm|M_M=0, n_M=0, b_M=1, v_n} + (M_{Mm|M_M=0, n_M=n_{Mt}, b_M=1, v_n} - M_{Mm|M_M=0, n_M=0, b_M=1, v_n}) \frac{n_M}{n_{Mt}} \right] \left( \frac{v}{v_n} \right)^{a_{vm}} \\ &+ (M_{Mm|M_M=M_{Mt}, n_M=n_{Mt}, b_M=1, v_n} - M_{Mm|M_M=0, n_M=n_{Mt}, b_M=1, v_n}) \frac{M_M}{M_{Mt}} \end{aligned} \quad (13)$$

- in a hydraulic motor with geometrical (variable) capacity  $q_{Mgv}$  ( $q_{Mgv} = b_M q_{Mt}$ ) per one shaft revolution (Fig. 4 – with  $n_{Mt}$ ,  $v_n$ , Fig. 6 – with  $v_{min}$ ,  $v_n$ ,  $v_{max}$ ):

$$\begin{aligned} M_{Mm|M_M, n_M, b_M, v} &= \left[ M_{Mm|M_M=0, n_M=0, b_M=1, v_n} + (M_{Mm|M_M=0, n_M=n_{Mt}, b_M=1, v_n} - M_{Mm|M_M=0, n_M=0, b_M=1, v_n}) \frac{n_M}{n_{Mt}} b_M \right] \left( \frac{v}{v_n} \right)^{a_{vm}} \\ &+ (M_{Mm|M_M=M_{Mt}, n_M=n_{Mt}, b_M=1, v_n} - M_{Mm|M_M=0, n_M=n_{Mt}, b_M=1, v_n}) \frac{M_M}{M_{Mt}} \end{aligned} \quad (14)$$

In models describing the torque of mechanical losses in a rotational hydraulic motor, used for description of losses and energy efficiency of the motor and of the hydrostatic transmission system in the ( $0 \leq \overline{\omega}_M < \overline{\omega}_{Mmax}$ ,  $0 \leq \overline{M}_M < \overline{M}_{Mmax}$ ) operating field, the increase of torque of mechanical losses occurring in fact at the motor speed  $n_M$  approaching the zero value ( $n_M = 0$ ) is not taken into account. That increase occurs below the shaft critical speed  $n_{Mcr}$ . The motor rotational speed instability  $\delta n_M$  increases below the critical speed  $n_{Mcr}$  and in effect the torque  $M_{Mm}$  of mechanical losses in the „shaft – working chambers” assembly increases. Assessment of the value of torque  $M_{Mm|M_M=0, n_M=0, b_M, v_n}$  of mechanical losses in a motor with zero rotational speed  $n_M$  ( $n_M = 0$ ) is done by approximation of the function  $M_{Mm|M_M=0, n_M, b_M, v_n} = f(n_M)$  at  $n_M = 0$ .

Exponent  $a_{vm}$  in expressions (7) and (9) determines the impact of the ratio  $v/v_n$  of viscosity  $v$  to the reference viscosity  $v_n = 35 \text{ mm}^2 \text{ s}^{-1}$  of the working fluid on the value of torque of mechanical losses. The impact occurs mainly in a piston displacement machines with fluid filling the casing (in pumps and hydraulic motors).

The proposed **theoretical model of the increase of torque  $\Delta M_{Mm|M_M, n_M, b_M, v}$  of mechanical losses in a rotational hydraulic motor, the increase resulting from loading the motor shaft with torque  $M_M$ , takes the same form in the case of a motor with theoretical (constant) capacity  $q_{Mt}$  per one shaft revolution ( $b_M = 1$ ) and in the case of a motor with geometrical (variable) capacity  $q_{Mgv}$  per one shaft revolution ( $q_{Mgv} = b_M q_{Mt}$ ):**

- in a hydraulic motor with theoretical (constant) capacity  $q_{Mt}$  ( $b_M = 1$ ) per one shaft revolution (Fig. 1 and 3):

$$\begin{aligned} \Delta M_{Mm|M_M, n_M, b_M=1, v} &= \\ &= (M_{Mm|M_M=M_{Mt}, n_M=n_{Mt}, b_M=1, v_n} - M_{Mm|M_M=0, n_M=n_{Mt}, b_M=1, v_n}) \frac{M_M}{M_{Mt}} \end{aligned} \quad (11)$$

- in a hydraulic motor with geometrical (variable) capacity  $q_{Mgv}$  ( $q_{Mgv} = b_M q_{Mt}$ ) per one shaft revolution (Fig. 4 and 5):

$$\begin{aligned} \Delta M_{Mm|M_M, n_M, b_M, v} &= \\ &= (M_{Mm|M_M=M_{Mt}, n_M=n_{Mt}, b_M=1, v_n} - M_{Mm|M_M=0, n_M=n_{Mt}, b_M=1, v_n}) \frac{M_M}{M_{Mt}} \end{aligned} \quad (12)$$

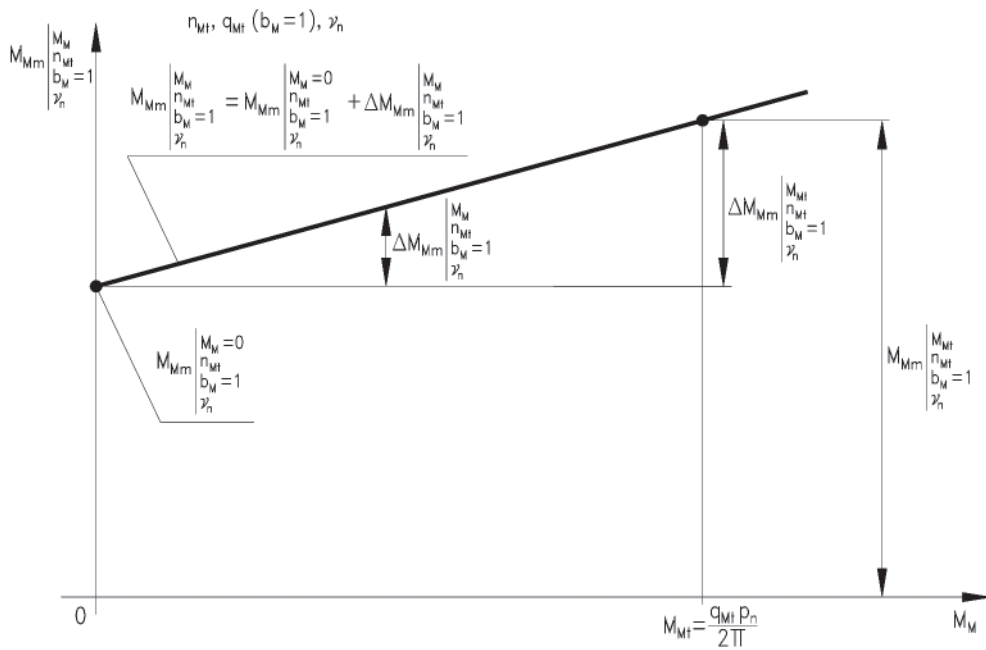


Fig. 1. Torque  $M_{Mm|M_M=n_M, n_M, q_{Mt}, v_n}$  of mechanical losses in the „shaft – working chambers” assembly of a rotational hydraulic motor with constant capacity  $q_{Mt}$  per one shaft revolution ( $b_M = 1$ ), at the shaft theoretical rotational speed  $n_{Mt}$  and at the working fluid reference viscosity  $v_n$ , as a function of the motor shaft torque  $M_M$  – graphical interpretation of the theoretical model (6)

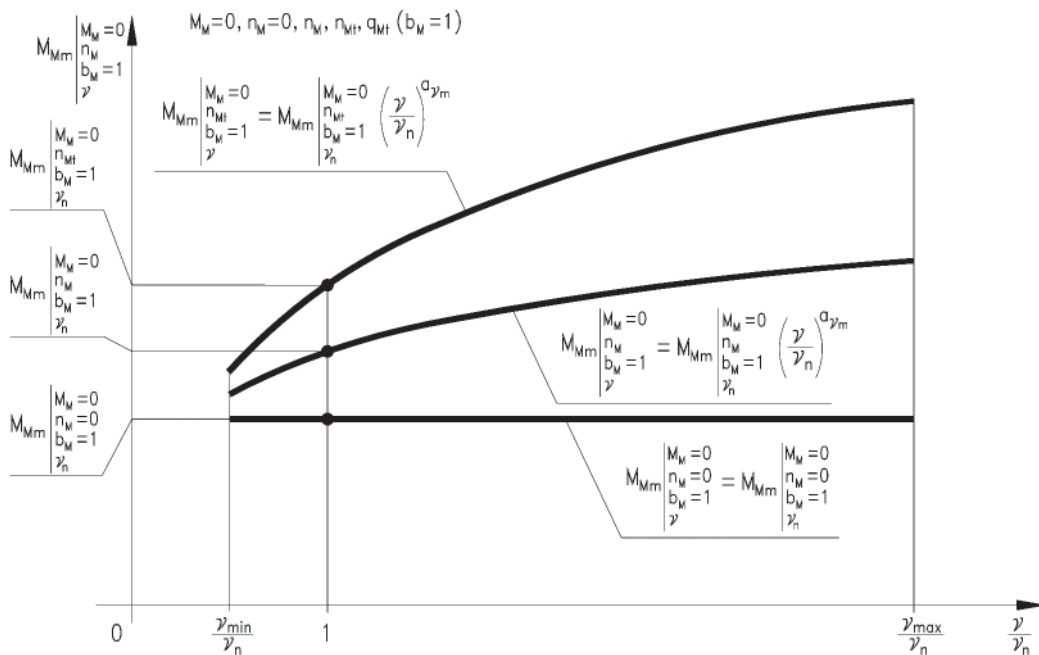


Fig. 2. Torque  $M_{Mm|M_M=0, n_M, n_Mt, q_{Mt}, v_n}$  of mechanical losses in the „shaft – working chambers” assembly of a rotational hydraulic motor with constant capacity  $q_{Mt}$  per one shaft revolution ( $b_M = 1$ ), at shaft torque  $M_M = 0$ , as a function of the ratio  $v/v_n$  of viscosity  $v$  to the working fluid reference viscosity  $v_n$  – graphical interpretation of the theoretical models (7) and (8); motor shaft speeds:  $n_M = 0, n_M, n_{Mt}$ . The impact of working fluid viscosity  $v$  on friction forces between the „shaft – working chambers” assembly elements and the working fluid occurs mainly in the piston hydraulic motors with casing filled with the working fluid.

## MATHEMATICAL MODELS OF THE TORQUE OF MECHANICAL LOSSES

In mathematical models describing the torque  $M_{Mm}$  of mechanical losses in a hydraulic rotational motor coefficients  $k_i$  of losses are used relating (comparing) the components describing the torque  $M_{Mm}$  of losses in theoretical models to the following reference values:

- theoretical torque  $M_{Mt} = \frac{q_{Mt} p_n}{2 \Pi}$  of a hydraulic motor with theoretical (constant) capacity  $q_{Mt}$  per one shaft resolution, determined at the decrease of  $\Delta p_M$  of pressure in the motor

equal to the system nominal pressure  $p_n$  ( $\Delta p_M = p_n$ ) and with assumption that there are no pressure and mechanical losses in the motor,

- theoretical rotational speed  $n_{Mt}$  of a hydraulic motor with constant capacity  $q_{Mt}$  per one shaft revolution resulting from the motor capacity  $Q_M$  equal to the theoretical pump  $Q_{Pt}$  ( $n_{Mt} = \frac{Q_{Pt}}{q_{Mt}}$ ),
- theoretical capacity  $Q_{Pt}$  of the hydraulic motor driving pump – a product of the theoretical capacity  $q_{Pt}$  per one shaft revolution of the constant capacity pump and the shaft speed  $n_{p0}$  of an unloaded pump ( $Q_{Pt} = q_{Pt} n_{p0}$ ).



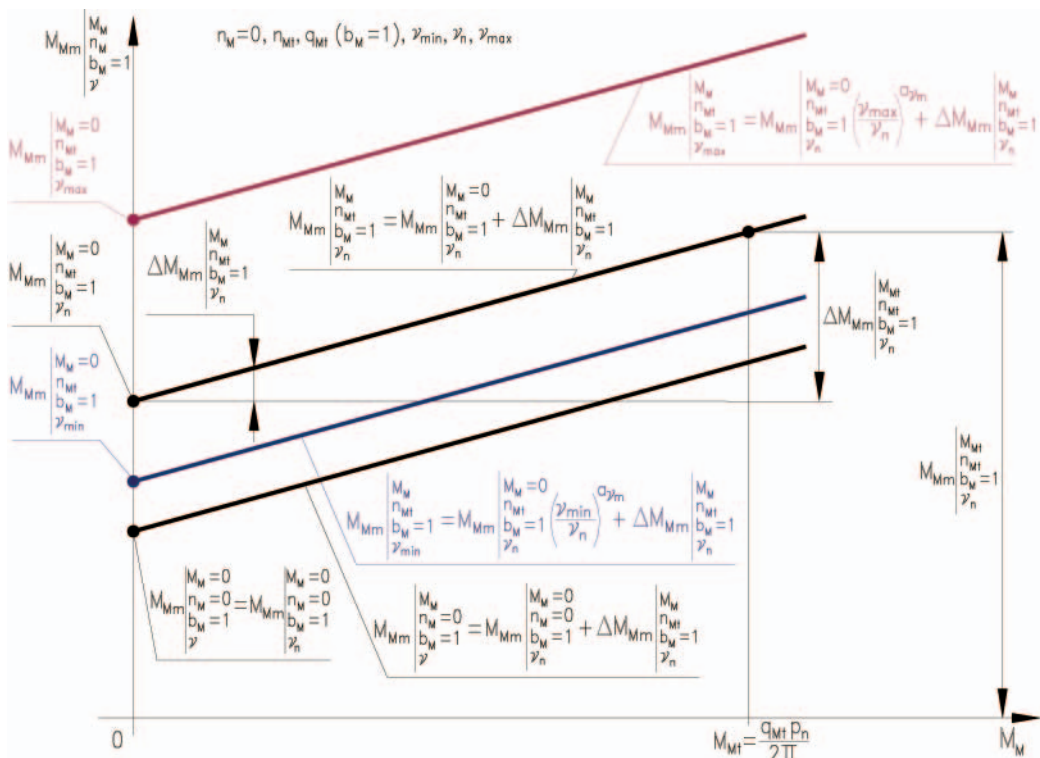


**Fig. 3.** Torque  $M_{Mm|M_M, n_M, b_M=1, \nu}$  of  $m$  mechanical losses in the „shaft – working chambers” assembly of a rotational hydraulic motor with constant capacity  $q_{Mt}$  per one shaft revolution ( $b_M=1$ ), as a function of the motor shaft torque  $M_M$  – graphical interpretation of the theoretical model (13); motor shaft speeds: theoretical speed  $n_{Mt}$ ,  $n_M=0$ ; working fluid viscosity  $\nu_{min}$ ,  $\nu_n$  and  $\nu_{max}$ . The impact of working fluid viscosity  $\nu$  on friction forces between the „shaft – working chambers” assembly elements and the working fluid occurs mainly in the piston hydraulic motors with casing filled with the working fluid.

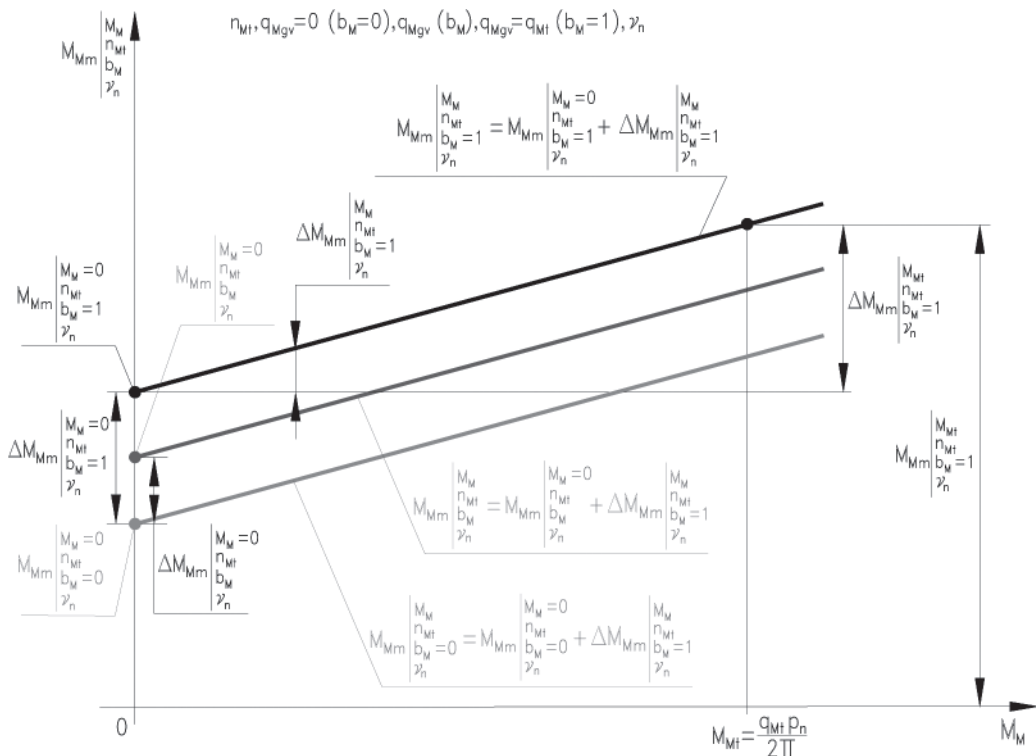


**Fig. 4.** Torque  $M_{Mm|M_M, n_M, b_M, \nu}$  of mechanical losses in the „shaft – working chambers” assembly of a rotational hydraulic motor with variable capacity  $q_{Mgv} = b_M q_{Mt}$  per one shaft revolution, at theoretical shaft rotational speed  $n_{Mt}$  and at working fluid reference viscosity  $\nu_n$ , as a function of the motor shaft torque  $M_M$  – graphical interpretation of the theoretical model (14); capacity  $q_{Mgv}$  per one shaft revolution (coefficient  $b_M$  of the change of capacity per one shaft revolution):  $q_{Mgv}=0$  ( $b_M=0$ ),  $q_{Mgv}(b_M)$ ,  $q_{Mgv}=q_{Mt}$  ( $b_M=1$ )

Theoretical and mathematical models describe the torque  $M_{Mm}$  of mechanical losses in a rotational hydraulic motor with theoretical (constant) capacity  $q_{Mt}$  per one shaft revolution or with geometrical (variable) capacity  $q_{Mgv} = b_M q_{Mt}$  per one shaft revolution:

–  $q_{Mt} = q_{M|\Delta p_{Mfi}=0, p_{M2i}=0, \nu_n}$  is a theoretical capacity per one shaft resolution of a constant capacity motor, determined at  $\Delta p_{Mfi} = 0$ ,  $p_{M2i} = 0$  and  $\nu_n$ , which is equal to the theoretical active volume of the working chambers during one shaft revolution,

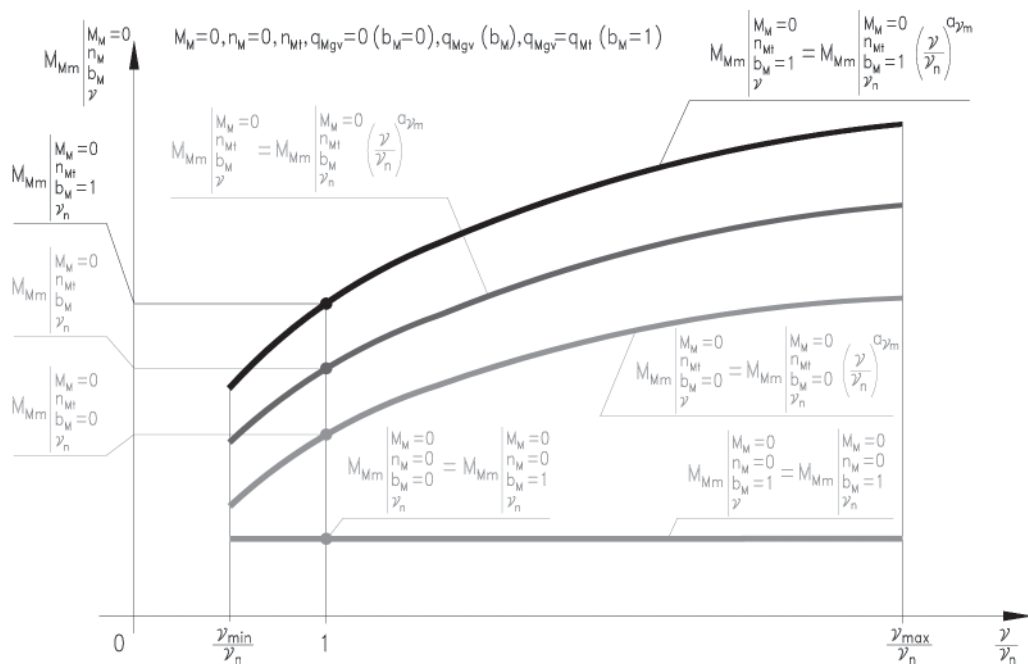


Fig. 5. Torque  $M_{Mm|M_M=0, n_M=0, b_M}$  of mechanical losses in the „shaft – working chambers” assembly of a rotational hydraulic motor with variable capacity  $q_{Mgv} = b_M q_{Mt}$  per one shaft revolution, at the shaft torque  $M_M = 0$  as a function of the ratio  $\nu/\nu_n$  of viscosity  $\nu$  to the working fluid reference viscosity  $\nu_n$  – graphical interpretation of the theoretical models (9) and (10); motor shaft speeds: theoretical speed  $n_M$ ,  $n_M = 0$ ; capacity  $q_{Mgv}$  per one shaft revolution (coefficient  $b_M$  of the change of capacity per one shaft revolution):  $q_{Mgv} = 0$  ( $b_M = 0$ ),  $q_{Mgv} = (b_M) q_{Mt}$ ,  $q_{Mgv} = q_{Mt}$  ( $b_M = 1$ ). The impact of working fluid viscosity  $\nu$  on friction forces between the „shaft – working chambers” assembly elements and the working fluid occurs mainly in the piston hydraulic motors with casing filled with the working fluid.

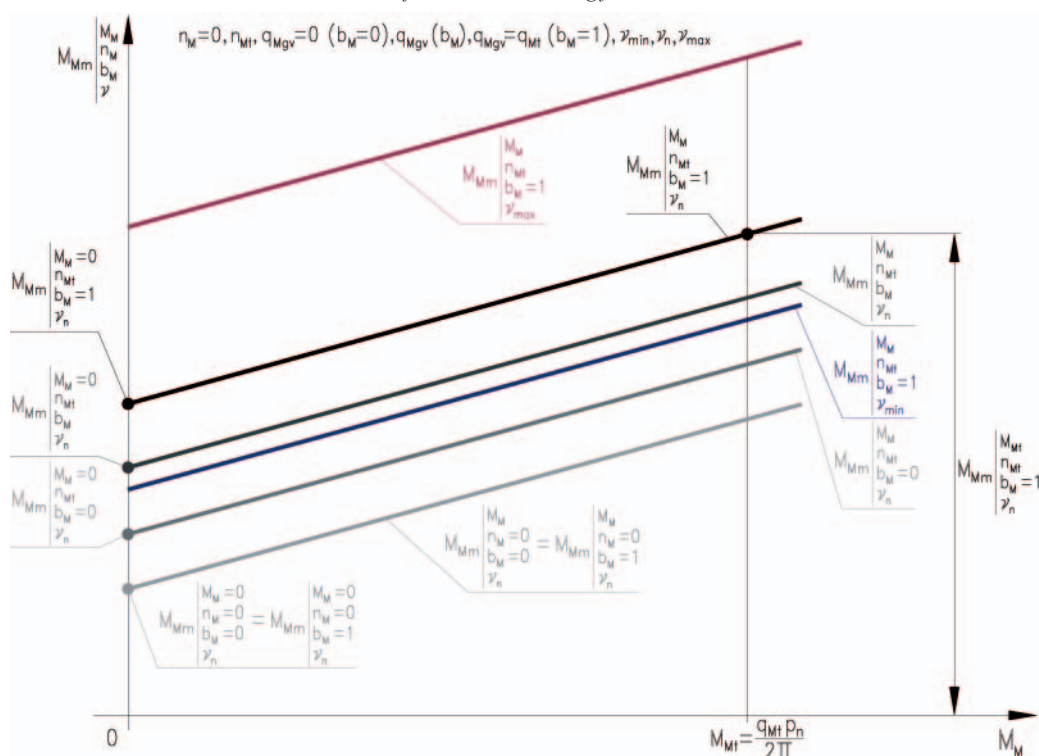


Fig. 6. Torque  $M_{Mm|M_M=0, n_M=0, b_M}$  of mechanical losses in the „shaft – working chambers” assembly of a rotational hydraulic motor with variable capacity  $q_{Mgv} = b_M q_{Mt}$  per one shaft revolution as a function of the motor shaft torque  $M_M$  – graphical interpretation of the theoretical model (14); motor shaft speeds: theoretical speed  $n_M$ ,  $n_M = 0$ ; capacity  $q_{Mgv}$  per one shaft revolution (coefficient  $b_M$  of the change of capacity per one shaft revolution):  $q_{Mgv} = 0$  ( $b_M = 0$ ),  $q_{Mgv} = (b_M) q_{Mt}$ ,  $q_{Mgv} = q_{Mt}$  ( $b_M = 1$ ). The impact of working fluid viscosity  $\nu$  on friction forces between the „shaft – working chambers” assembly elements and the working fluid occurs mainly in the piston hydraulic motors with casing filled with the working fluid

–  $q_{Mgv} = b_M q_{Mt}$  is a geometrical capacity per one shaft revolution of a variable capacity motor, determined at  $\Delta p_{Mi} = 0$ ,  $p_{M2i} = 0$  and  $\nu_n$ , which is equal to the geometrical active volume of the working chambers during one shaft revolution. In developing the models it is assumed that capacity  $q_{Mgv}$  per one hydraulic motor shaft revolution changes in the  $0 \leq q_{Mgv} \leq q_{Mt}$  range and coefficient  $b_M = q_{Mgv}/q_{Mt}$

of the variation of capacity per one motor shaft revolution changes in the  $0 \leq b_M \leq 1$  range.

The proposed mathematical models describing the torque  $M_{Mm}$  of mechanical losses in the „shaft – working chambers” assembly, related to the theoretical models of the torque of mechanical losses, take the form:

- in a hydraulic motor with theoretical (constant) capacity  $q_{M_t}$  ( $b_M = 1$ ) per one shaft revolution [referring to theoretical model (13)]:

$$M_{Mm|M_M, n_M, b_M=1, v} = \left( k_{7.1.1} + k_{7.1.2} \frac{n_M}{n_{M_t}} \right) M_{M_t} \left( \frac{v}{v_n} \right)^{a_{vm}} + k_{7.2} M_M = \left( k_{7.1.1} + k_{7.1.2} \frac{n_M}{n_{M_t}} \right) \frac{q_{M_t} p_n}{2\Pi} \left( \frac{v}{v_n} \right)^{a_{vm}} + k_{7.2} M_M \quad (15)$$

where:

$$k_{7.1.1} = \frac{M_{Mm|M_M=0, n_M=0, b_M=1, v_n}}{M_{M_t}} = \frac{M_{Mm|M_M=0, n_M=0, b_M=1, v_n}}{\frac{q_{M_t} p_n}{2\Pi}} \quad (16)$$

$$k_{7.1.2} = \frac{M_{Mm|M_M=0, n_M=n_{M_t}, b_M=1, v_n} - M_{Mm|M_M=0, n_M=0, b_M=1, v_n}}{M_{M_t}} \quad (17)$$

$$= \frac{M_{Mm|M_M=0, n_M=n_{M_t}, b_M=1, v_n} - M_{Mm|M_M=0, n_M=0, b_M=1, v_n}}{\frac{q_{M_t} p_n}{2\Pi}}$$

$$k_{7.2} = \frac{M_{Mm|M_M=M_{M_t}, n_M=n_{M_t}, b_M=1, v_n} - M_{Mm|M_M=0, n_M=n_{M_t}, b_M=1, v_n}}{M_{M_t}} \quad (18)$$

$$= \frac{M_{Mm|M_M=M_{M_t}, n_M=n_{M_t}, b_M=1, v_n} - M_{Mm|M_M=0, n_M=n_{M_t}, b_M=1, v_n}}{\frac{q_{M_t} p_n}{2\Pi}}$$

- in a hydraulic motor with geometrical (variable) capacity  $q_{M_{gv}}$  ( $q_{M_{gv}} = b_M q_{M_t}$ ) per one shaft revolution [referring to theoretical model (14)]:

$$M_{Mm|M_M, n_M, b_M, v} = \left( k_{7.1.1} + k_{7.1.2} \frac{n_M}{n_{M_t}} b_M \right) M_{M_t} \left( \frac{v}{v_n} \right)^{a_{vm}} + k_{7.2} M_M = \left( k_{7.1.1} + k_{7.1.2} \frac{n_M}{n_{M_t}} b_M \right) \frac{q_{M_t} p_n}{2\Pi} \left( \frac{v}{v_n} \right)^{a_{vm}} + k_{7.2} M_M \quad (19)$$

where: coefficient  $k_{7.1.1}$  is described by expression (16), coefficient  $k_{7.1.2}$  – by expression (17), coefficient  $k_{7.2}$  – by expression (18).

## CONCLUSIONS

1. Theoretical and mathematical models have been developed of the torque  $M_{Mm}$  of mechanical losses in the „shaft – working chambers” assembly of a rotational hydraulic motor with constant  $q_{M_t}$  ( $V_{M_t}$ ) and with variable  $q_{M_{gv}}$  ( $V_{M_{gv}}$ ) capacity per one motor shaft revolution. The models present dependence of the torque  $M_{Mm}$  of mechanical losses in the assembly on the torque  $M_M$  loading the shaft and on the shaft speed  $n_M$  [changing in the ( $0 \leq \bar{M}_M < \bar{M}_{Mmax}$ ,  $0 \leq \bar{\omega}_M < \bar{\omega}_{Mmax}$ ) motor (and the hydrostatic transmission system) operating range] and also on the working fluid viscosity  $v$  changing in the  $v_{min} \leq v \leq v_{max}$  range. Torque  $M_M$ , shaft speed  $n_M$  and working fluid viscosity  $v$  are independent of the motor and of the losses in it. The models present also the dependence of torque  $M_{Mm}$  on the capacity  $q_{M_{gv}}$  per one shaft revolution (coefficient

$b_M = q_{M_{gv}}/q_{M_t}$  of the capacity per one shaft revolution) in a variable capacity motor. In the models, the change of  $q_{M_{gv}}$  ( $b_M$ ) is assumed in the  $0 \leq q_{M_{gv}} \leq q_{M_t}$  ( $0 \leq b_M \leq 1$ ) range, although during the motor operation  $b_{Mmin}$  is of the order of  $0.2 \div 0.3$ .

2. Mathematical models of the torque  $M_{Mm}$  of mechanical losses are based on the defined coefficients  $k_i$  of energy losses, relating the torque of mechanical losses to the reference values:
  - theoretical torque  $M_{M_t}$  of the motor with theoretical (constant) capacity  $q_{M_t}$  per one shaft revolution determined at the system nominal pressure  $p_n$ ,
  - theoretical rotational speed  $n_{M_t}$  of the motor with theoretical (constant) capacity  $q_{M_t}$  per one shaft revolution resulting from the pump theoretical capacity  $Q_{Pr}$ .
3. Mathematical models of the torque  $M_{Mm}$  of mechanical losses in the „shaft – working chambers” assembly should correspond with models of volumetric losses in the motor working chambers and with models of pressure losses in the motor channels.

## BIBLIOGRAPHY

1. Paszota Z.: *Graphical presentation of the power of energy losses and power developed in the elements of hydrostatic drive and control system. Part I – Rotational hydraulic motor speed series throttling control systems*. Chapter in the monograph: „Research, design, production and operation of hydraulic systems” (in Polish), Adam Klich, Edward Palczak and Andrzej Meder editors. „Cylinder” Library. Komag Mining Mechanisation Centre, Gliwice 2008
2. Paszota Z.: *Graphical presentation of the power of energy losses and power developed in the elements of hydrostatic drive and control system. Part II – Rotational hydraulic motor speed parallel throttling control and volumetric control systems*. Chapter in the monograph: „Research, design, production and operation of hydraulic systems” (in Polish), Adam Klich, Edward Palczak and Andrzej Meder editors. „Cylinder” Library. Komag Mining Mechanisation Centre, Gliwice 2008
3. Paszota Z.: *Direction of increase of power stream in the hydrostatic drive and control system. Graphical presentation of the power of energy losses and power developed in the elements of hydrostatic drive and control system. Part I – Rotational hydraulic motor speed series throttling control systems*. (in Polish), Napędy i sterowanie, scientific monthly, No 10 (114), October 2008
4. Paszota Z.: *Direction of increase of power stream in the hydrostatic drive and control system. Graphical presentation of the power of energy losses and power developed in the elements of hydrostatic drive and control system. Part II – Rotational hydraulic motor speed parallel throttling control and volumetric control systems*. (in Polish), Napędy i sterowanie, scientific monthly, No 11 (115), November 2008
5. Paszota Z.: *Graphical presentation of the power of energy losses and power developed in the elements of hydrostatic drive and control system. Part I – Rotational hydraulic motor speed series throttling control systems*. Polish Maritime Research 03/2008
6. Paszota Z.: *Graphical presentation of the power of energy losses and power developed in the elements of hydrostatic drive and control system. Part II – Rotational hydraulic motor speed parallel throttling control and volumetric control systems*. Polish Maritime Research 04/2008
7. Paszota Z.: *The operating field of a hydrostatic drive system*. Chapter in the monograph: „Research, design, production and operation of hydraulic systems” (in Polish), Adam Klich, Antoni Kozieł and Edward Palczak editors. „Cylinder” Library. Komag Mining Mechanisation Centre, Gliwice 2009

8. Paszota Z.: *Parameters of the energy efficiency investigations of pumps and hydraulic motors. The operating field of a hydrostatic drive system.* (in Polish), Napędy i sterowanie, scientific monthly, No 11 (127), November 2009
9. Paszota Z.: *The operating field of a hydrostatic drive system parameters of the energy efficiency investigations of pumps and hydraulic motors.* Polish Maritime Research 04 / 2009
10. Paszota Z.: *Energy losses in the hydraulic rotational motor – definitions and relations for evaluation of the efficiency of motor and hydrostatic drive.* Polish Maritime Research 02/2010.

#### **CONTACT WITH THE AUTHOR**

Prof. Zygmunt Paszota  
Faculty of Ocean Engineering  
and Ship Technology  
Gdansk University of Technology  
Narutowicza 11/12  
80-233 Gdansk, POLAND  
e-mail: zpszota@pg.gda.pl



# Investigation of the underwater noise produced by ships by means of intensity method

**Eugeniusz Kozaczka**, Prof.  
Gdansk University of Technology  
**Jacek Domagalski**, Ph. D.  
**Ignacy Gloza**, Ph. D.  
Naval Academy of Gdynia

## ABSTRACT

*This paper presents results of research on spectral structure of underwater noise acoustic field radiated into water by selected ships moving in shallow waters. Underwater acoustic field of ships in motion is associated with acoustic activity of ship mechanisms and equipment under work. Vibration energy radiated by the mechanisms and devices is transmitted by ship structural elements to surrounding water where it is propagated in the form of acoustic waves of a wide frequency band. In this paper are presented results of the research on propagation of energy of acoustic waves in the near field, obtained from acoustic pressure measurements by means of two sensors located close to each other.*

**Keywords:** energy, propagation, hydroacoustics

## INTRODUCTION

Research on spectral structures of underwater noise generated to water by vessels of different classes have been used for many years in the detection, location and identification systems, and also in the homing guidance and initiation units of sea weapons systems.

Underwater sound field of the vessels is connected with the activity of acoustic wave sources installed on ships, i.e. ship mechanisms and equipment (main engines, generators, gears, pumps, shaft lines, pipes, ducts, etc.) and hydrodynamic sources such as screw propeller and water flow around the hull.

Theoretical estimation of the level of acoustic energy near the wave source and attempts to present the vertical and horizontal distribution of energy in the plane of trajectory are difficult and currently not very effective. This follows from the fact that the theoretical model of extended source, which is a superposition of several different types of sources of acoustic waves, namely those due to water flow (propeller flow, flow around the hull), ship hull vibration and cavitation, makes that their full description is extremely complicated and difficult to apply in practice. A great difficulty is the necessity to take into account the influence of surface limiting water environment (free surface and bottom of sea). The next difficulty is the fact that the waves generated by a ship to water near the sources are non-stationary and nonlinear. It seems that many unknown variable parameters which shape acoustics of the near field of ships make application of adequate numerical models to solve this problem, impossible. For this reason, in practice, the measurements are performed

in natural conditions at various depths of ship operation and various set of points of their propulsion systems, and then results of the measurements are recorded and archived in digital form in specialty systems.

To-be-archived sound pressure measurements should be recorded in the far field zone [1, 2] i.e. where the following condition is satisfied:

$$d^2 \gg r\lambda/2\pi \text{ or } \Delta r \ll \lambda \quad (1)$$

where:

- r - the distance between source and receiver,
- $\Delta r$  - distance between sensors,
- d - maximum linear dimension of the active part of transmitter,
- $\lambda$  - acoustic wave length.

For the assumed depth of the coastal water region, amounting from 10 to 70 m at which underwater noise measurements are made, the condition of the far field would be satisfied for the frequency  $f$  31000 [Hz] in the trial area situated at the depth of 10 m. This limitation is also dependent on radiating surface dimension and sound propagation velocity in water.

The sound pressure measurement performed on the measurement depths, does not allow to precisely characterize acoustic field distribution of vessel in motion. Characteristic components of the spectrum generated by the main and auxiliary mechanisms, propeller, shaft line of ships of different classes are contained in the frequency band up to about 150 [Hz]. Sample distributions of hydroacoustic fields of selected vessels are shown in Fig. 1.

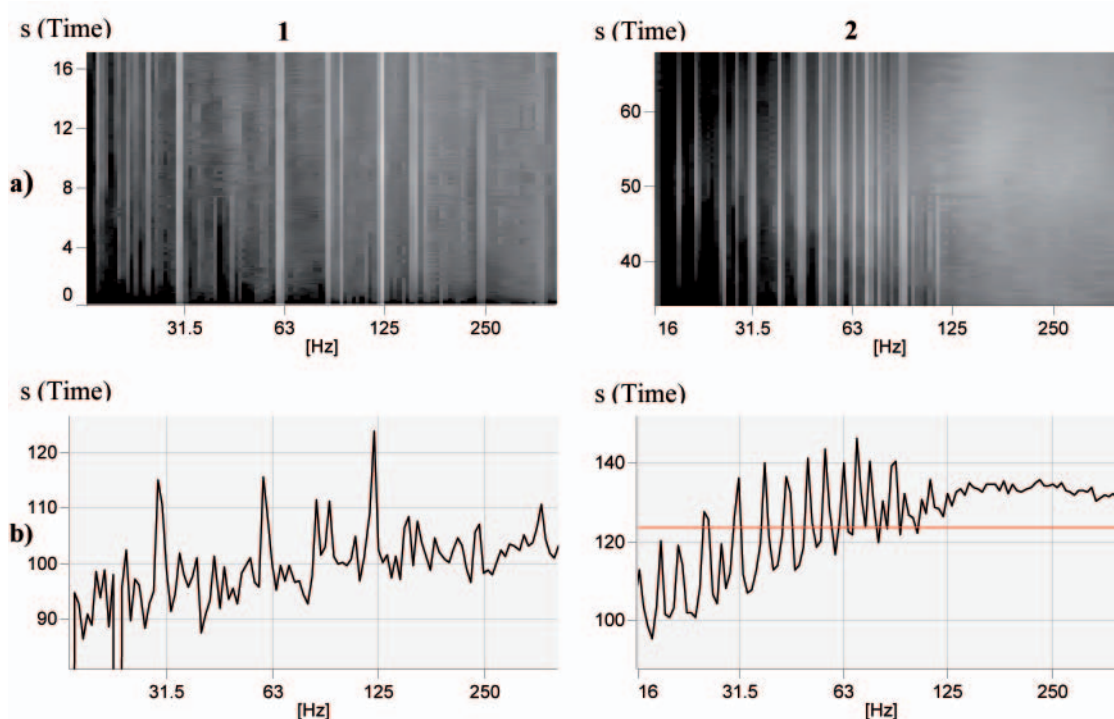


**Fig. 1.** Example acoustic spectrograms and power spectra of vessels, where:  
 1 - ship with turbine propulsion system, 2 - ship with conventional propulsion system,  
 a - the spectrograms made at the frequency band up to 500 [Hz] with resolution of 1/24 octave,  
 b - the underwater noise spectrum made in the place where the most noisy part of the ship was situated directly above the acoustic sensor

In the presented figures it is clearly visible that the characteristic spectral components, reflecting both the frequency and level of work of the main propulsion systems and auxiliary mechanisms, are located in the frequency band up to about 100 [Hz].

When taking into account the short characteristics of the acoustic field distribution of the above mentioned ships of different classes, it seems evident that that measurement ranges in the frequency domain should cover the whole range of length of acoustic waves propagating from the ships to surrounding water.

Sound intensity measurement of underwater noise enables to carry out more accurate research in this water region. Such measurement based on a suitable spacing of acoustic sensors and precise phase matching of hydrophones and measuring setups, will make it possible to process of recorded data in the frequency band of interest.

In order to determine spatial distribution of acoustic energy it is necessary to know vibration velocity distribution of acoustic wave sources. In the case of vessels to determine precisely vibration velocity distribution on hull shell plating is very difficult because of a complex form of hull surface and limited number of measurement points. In association with the technical and financial difficulties, in the available literature [3, 4] can be found a method for determining the acoustic wave velocity which makes it possible to determine a substitute vibration velocity distribution. Such distribution is determined experimentally by measuring the acoustic pressure and velocity. Measurement of acoustic pressure in an arbitrary point in space is easy to realize. For the measurement it is sufficient to process data from one sensor only, however the system consisted of at least two sensors is necessary to measure the acoustic velocity. The approximate component of acoustic velocity vector, directed along the vector  $\vec{r}$  determined from acoustic pressure measurements with the use of two sensors placed close to each other, can be determined from the following relation:

$$v_r = -\frac{1}{\rho \Delta r} \int (p_B - p_A) dt \quad (2)$$

where:

$p_B - p_A$  - pressure difference at the points A and B,  
 $\rho$  - density of medium.

The approximation can be applied to the far field in which the relation (1) is satisfied. During the acoustic velocity measurements the measured values of sound pressure are often converted from analogue to digital form.

$$v_r(n) = v_0 - \frac{\Delta t}{\rho \Delta r} [p_B(i) - p_A(i)] \quad (3)$$

where:

$v_0$  - constant component of velocity which can be determined after calculation of velocity values for the entire wave period.

The resulting acoustic velocity is used to determine the acoustic wave intensity which, for stationary signals, can be described by the dependence:

$$I(r) = \overline{p(r, t)v(r, t)} \quad (4)$$

Taking into account the dependence (3) we obtain:

$$I = \frac{1}{2\rho \Delta r} \overline{(p_A + p_B) \int (p_B - p_A) dt} \quad (5)$$

And, after an appropriate transformation the digital dependence (5) takes the form:

$$I = \frac{1}{2\pi k \rho \Delta r} \cdot \text{Im}[G_{xy}(k)] \quad (6)$$

where:

$0 < k < N$

$\text{Im}[G_{xy}(k)]$  - complex part of cross spectrum.

## LIMITATIONS OF THE PRESENTED METHOD

The method used to measure sound intensity with the use of two sensors located close to each other, has some limitations. The basic error of this method is connected with inaccuracy of measuring the derivative of hydroacoustic pressure. The error is observed in the higher frequency ranges. For a flat harmonic wave, the estimated value of related to the exact value of  $\hat{I}$  the sound intensity  $I$ , can be determined from the dependence (7):

$$\frac{\hat{I}}{I} = \frac{\sin(k\Delta r)}{k\Delta r} \quad (7)$$

where:

$k$  - wave number.

In the logarithmic form the dependence is as follows:

$$L = 10 \lg \left( \frac{\sin(k\Delta r)}{k\Delta r} \right) \quad (8)$$

For the spherical wave, the estimated value of  $\hat{I}$  related to the exact value of the sound intensity  $I$ , can be determined from the dependence (9):

$$\frac{\hat{I}}{I} = \frac{\sin(k\Delta r)}{k\Delta r} \left( 1 - \frac{1}{4} \left( \frac{\Delta r}{r} \right)^2 \right)^{-1} \quad (9)$$

An essential error of the method in the low frequency ranges is a deviation resulting from the phase mismatch of measuring setups [2, 3]. For this reason, we should tend to exactly match the phases of all the measuring setups at which  $\varphi \rightarrow 0$ . If the phase mismatch occurs between the two setups for flat wave then the estimate of  $\hat{I}$  - value related to the exact sound intensity  $I$ , can be determined by using the relation (10):

$$\frac{\hat{I}}{I} = \frac{\sin(k\Delta r \pm \varphi)}{k\Delta r} \quad (10)$$

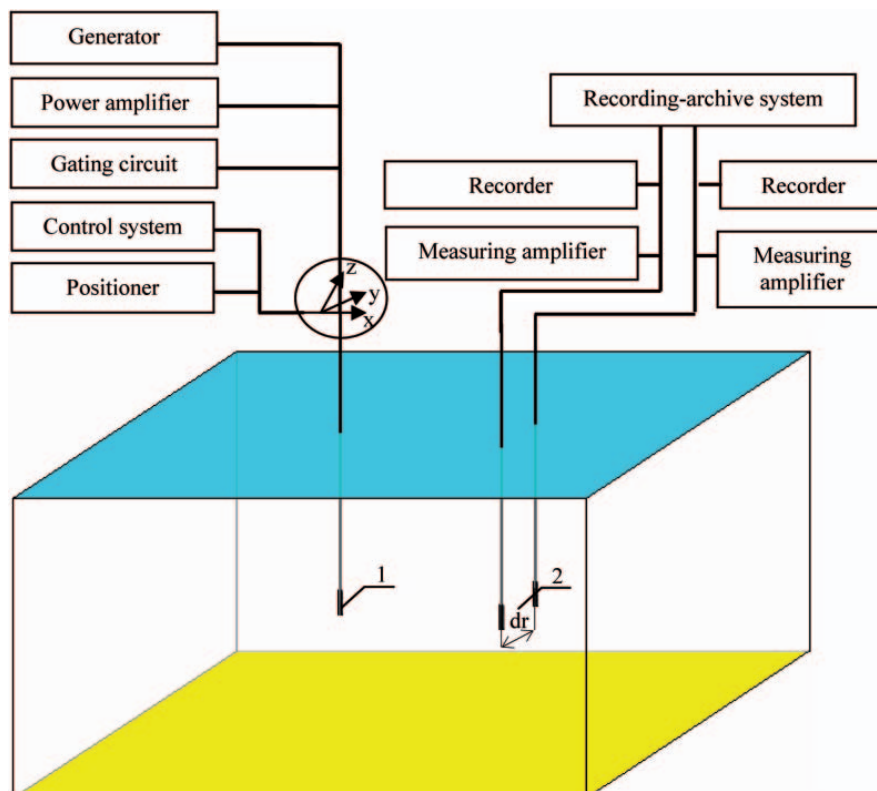


Fig. 2. Block diagram of the measuring system including the tank. Notation: 1 - sending hydrophone, 2 - receiving hydrophones

## CALIBRATION OF MEASURING SETUPS

In order to obtain authentic results of measurements it is necessary to perform accurate calibration of measuring setups to determine the exact phase difference of measuring setups. To determine the differences the method of submission of mutually perpendicular harmonic signals has been used. The curve obtained as a result of the composing of signals is dependent on frequency and phase of the signals as well as values of their amplitudes. Results of the composing of signals were published first by Lissajous, a French scientist, at the end of 19<sup>th</sup> century.

The laboratory calibration tests of the measuring setup of the probe for underwater, measuring the sound intensity have been performed in a measuring tank. The block diagram of the measuring system including the tank, is shown in Fig. 2.

In order to eliminate the waves reflected from the tank walls and water surface the system has been applied for calibrating the sensor by means of the impulse method [2], which makes it possible to eliminate unfavorable reflected waves by suitable selection of duration time of pulses of harmonic waves generated in appropriate time intervals. The duration times of sending pulses resulted from the basin's geometry and were determined for the reflections from the tank walls from the dependence:

$$\tau \leq \frac{l-r}{c}, \quad \tau \leq \frac{\sqrt{r^2 + b^2} - r}{c} \quad (11)$$

- for reflections from the bottom and surface:

$$\tau \leq \frac{\sqrt{r^2 + h^2} - r}{c} \quad (12)$$

- for the reflections between hydrophones:

$$\tau \leq \frac{2r}{c} \quad (13)$$

where:

$\tau$  - duration time of a signal free from reflected signals,

$c$  - sound velocity in water.

From the far field condition (1.1), by knowing the maximum linear dimension of the transmitter,  $d \leq 0.1$  m, and the sound velocity in water,  $c = 1480$  m/s, the minimum distance from the receiving hydrophones to the sending one, has been determined at the frequency for which the measurement system has been controlled.

Tab. 1. The length of the near field transmitter for

f [kHz]	5	6	7	8	9	10
$d^2f/c$ [m]	0.033	0.041	0.047	0.054	0.061	0.068

The measurements were performed for the distance between receiving and sending hydrophones,  $r \leq 0.4$  m, and the pulse duration which could not be longer than  $t \leq 0.4$  s, taking into account the dependence (11), (12) and (13).

The tested probe consisted of two 4032 RESON hydrophones spaced at the distance  $\Delta r = 38$  mm, and having the sensitivity values:

A - no. 3702080: 170.4 dB at 250 Hz ; 169,1 dB at 8 kHz,  
 B - no. 3702082: 170.3 dB at 250 Hz ; 169 dB at 8 kHz.

The difference in sensitivity of the sensors in the band of interest, up to 10 kHz, is negligible. The significant differences in the indicated levels, reaching from 3 to 10 dB, occurred in the frequency band from 20 to 100 kHz. The 8100 Brüel & Kjar hydrophone which generated acoustic wave in the frequency ranges given in Tab. 1, served as a source of harmonic waves. The sinusoidal signal from the generator was transmitted to the 4440 Brüel & Kjar gate which controlled the length and pulse repetition frequency. The signal from the gate was properly amplified by 2713 Brüel & Kjar power amplifier and then transmitted in the form of short pulses of harmonic wave, to the surrounding water by the sending hydrophone. The acoustic wave produced by the hydrophone was received by two receiving hydrophones placed at equal distances from the sending sensor. Signals received by them were amplified by 2636 Brüel & Kjar amplifiers, and then recorded and processed in a analyzer which made it possible to determine mismatch of the tested phases of the system. The extensive results of the performed calibration of the probe are contained in the report from realization of this work [2] performed at the Radiolocation and Hydrolocation Department of Polish Naval Academy in Gdynia. The publication presents only

representative results of the probe calibration, recorded in the form of Lissajous curves.

From the measurements performed for the probe in question it can be concluded that the phase mismatch of the measuring setups did not exceed  $0.2^\circ$  for the tested wave length. The level of phase mismatch was enlarged to  $0.3^\circ$  after taking into account the specific conditions of measurements conducted in the dynamic trial areas. The lower frequency range for different distances between sensors was calculated for this value (acc. Eq. 10).

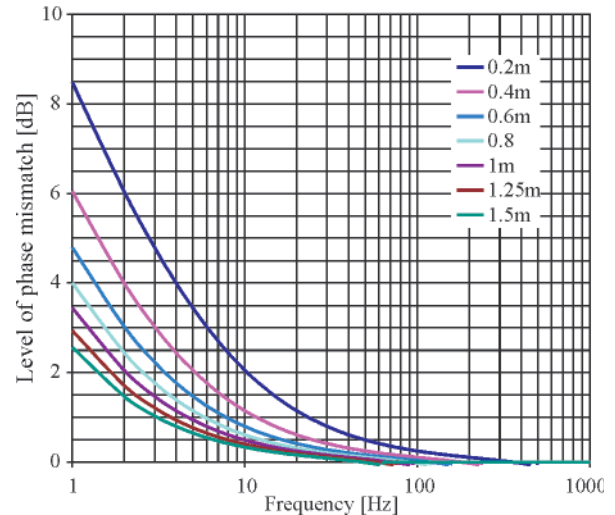


Fig. 4. The values of the phase mismatch level of the lower frequency range for the distance between sensors  $\Delta r = 0.2, 0.4, 0.6, 0.8, 1, 1.25, 1.5$  m, respectively

The upper frequency range for the same distance was determined in the same way by taking into account the dependence (7). On the basis of those frequency ranges the frequency range at which the error does not exceed 1 [dB], was determined.

On the basis of the performed research it can be concluded that, for the phase mismatch level of  $0.3^\circ$ , measurements in dynamic trial areas can be conducted in the frequency range from  $10$  [Hz]  $\pm 2$  [dB] to  $1325 \pm 1$  [dB] and at the spacing between hydrophones equal to  $0.2$  [m]. The described sound intensity measuring method makes performing the tests within the specified frequency band in the coastal zone, possible.

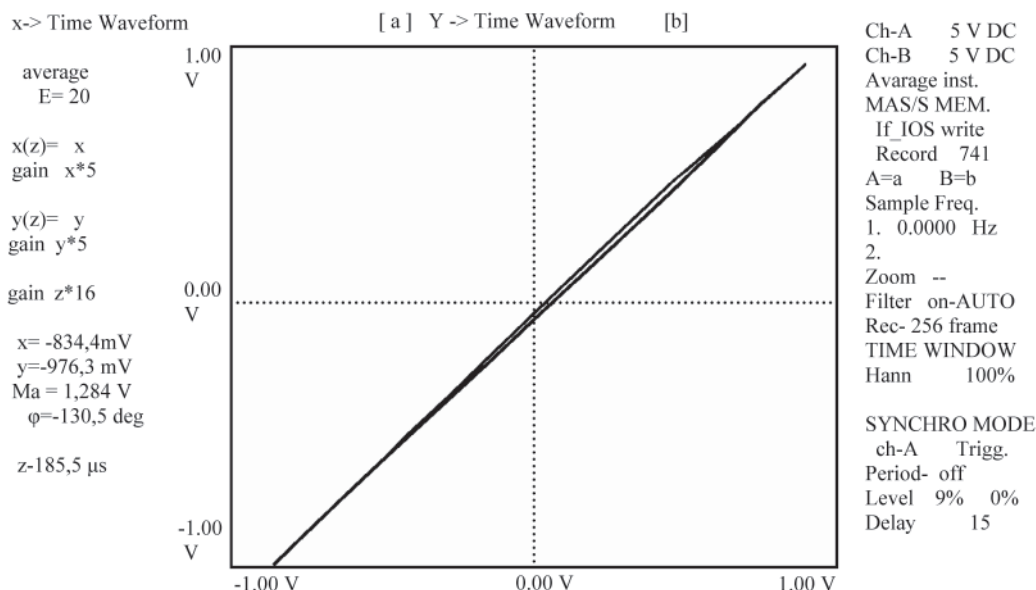


Fig. 3. The result of probes calibration matching



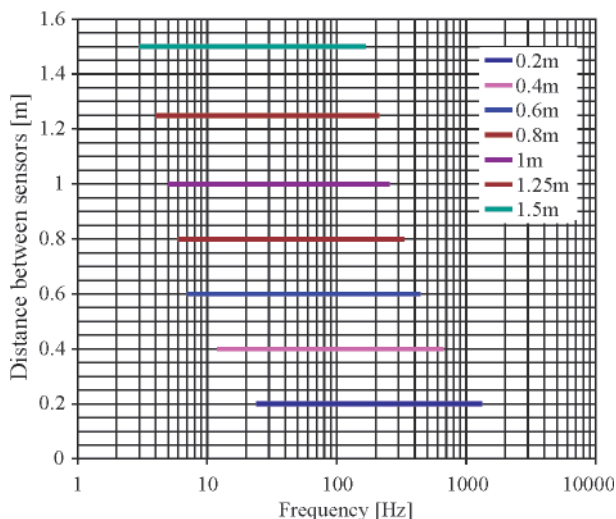


Fig. 5. The frequency ranges of the sound intensity measurement at which the error does not exceed 1 [dB]

## DYNAMIC MEASUREMENTS

The acoustic noise measurements of submarines are repeated periodically during operation of each ship. During the measurements ships pass at least twice through the trial area with the set work parameters of the propulsion system. The determined ship parameters are reached at the distance of 300 m at least before the trial area and maintained over the distance of 600 m at least (300 m behind the buoys). Sound pressure measurements are made at a distance afore and astern the ship to make it possible to characterize underwater disturbances of the ship. The passage of ship through the trial area is very often presented in the form of sound pressure in function of time and frequency. The spectrogram of the performed recording is presented in Fig. 6.

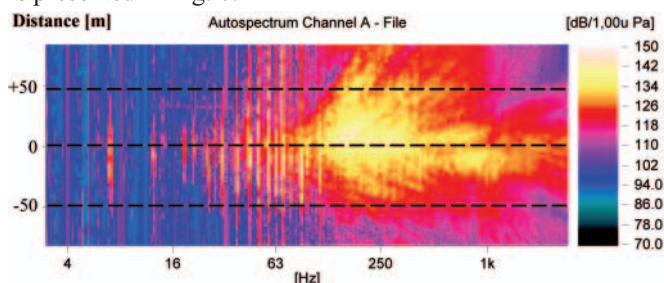


Fig. 6. The acoustic field spectrogram of the ship moving with forward speed of 4 kn

The spectrogram consists of 299 spectra recorded every 312 [ms] with the resolution of 0.04167 octave in the frequency range from 3[Hz] to 2.818[kHz]. Broken lines mark the distance of the ship from the acoustic sensor.

In the spectrogram two areas are clearly visible. The first area contains frequencies to about 100[Hz]. In this area the characteristic spectrum components resulting from working ship mechanisms, can be observed. The second area of the frequency range from 100[Hz] to 2.8[kHz] contains a continuous spectrum. The spectrum is connected with work of cavitating propeller, turbulent flow in pipelines, flow around the hull, airflow in ventilators, etc. Such analysis makes it possible to select, out of the spectrogram, a spectrum in an arbitrary area covered by the measurements.

Fig. 7 presents the ship's spectra taken from the places pointed in the spectrogram. The first of them was recorded when the most noisy part of the ship was situated about 50[m] before the acoustic sensor. The second - when the disturbance source

was just above the sensor, and the third one - corresponds with the distance of 50[m] behind the sensor.

The two previously discussed areas are also visible in the spectrum in question. From them it can be also observed that before the trial area the ship generates mainly waves connected with work of mechanisms and ship equipment, and behind it the waves connected with work of the propeller are dominant. To more clearly present the figures, the signal recorded when the ship passed just above the acoustic sensor, was suppressed by 30[dB], and that corresponding with the distance of 50[m] behind the trial area - by 60[dB].

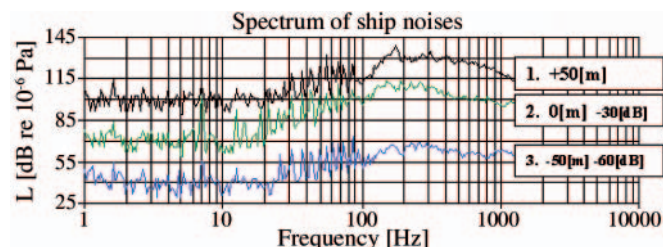


Fig. 7. The spectra obtained at some distance before and behind the trial area, as well as during passing just above the acoustic sensor.

**Notation:** 1 - the spectrum of the ship taken 50[m] behind the trial area, 2 - the spectrum recorded when the most noisy part of the ship passes above the acoustic sensor, 3 - the spectrum of the ship taken 50[m] before the trial area

The characteristic components visible in the first area can be unambiguously assigned to working mechanisms and equipment of the ship. Examination of ship spectrum is one of the methods for identification of ship underwater noise. In order to carry out identification of the components such tests are usually performed in two stages. The first contains measurements carried out on anchored ship. The measurements consist in the measuring of vibration of main mechanisms and auxiliary equipment of the ship, accompanied with the simultaneous measuring of sound pressure in water depth. In the second stage the ship crosses dynamic trial areas, under various operational settings of its propulsion system. During the measurements both underwater noise and vibration of selected mechanisms and equipment, are recorded. On the basis of the measurements it is possible to characterize the components visible in the first presented field. To identify the components, an analysis with using constant band width filters for the tested frequency band, is often performed. A representative identification analysis of the spectrum of the ship in motion is shown in Fig. 8.

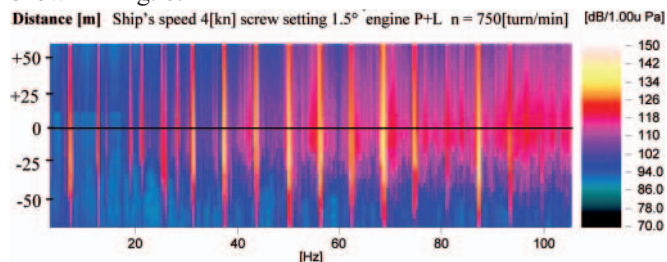


Fig. 8. The acoustic field spectrogram of the ship with forward speed of 4 kn, recorded in the frequency band up to 100[Hz]

The spectrogram consists of 74 spectra recorded every 1.333[s] with the resolution of 0.25[Hz] in the frequency band up to 100[Hz]. From the figure was selected the spectrum when the ship's power plant was situated just above the acoustic sensor (the place distinguished with black line at the spectrogram).

The figure clearly shows discrete spikes coming from working main engines, shaft lines and propeller, and a single spike marked "I" in red color, coming from an electric generating

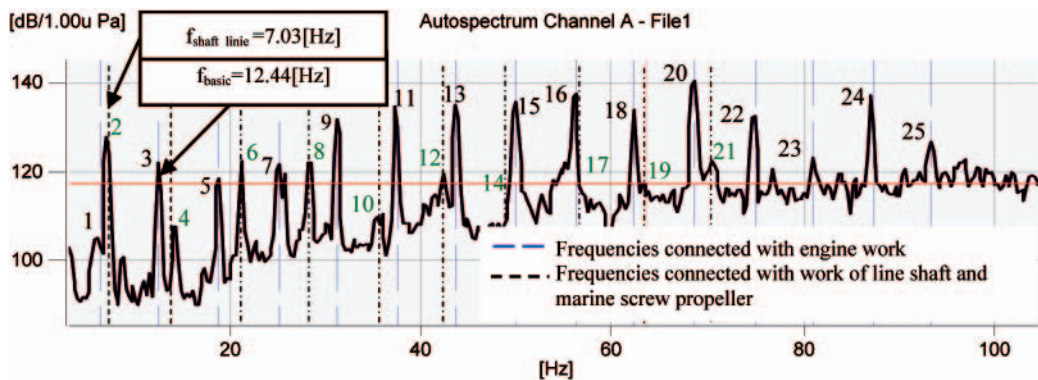


Fig. 9. The ship acoustic power spectrum recorded at the distance marked "0" in Fig. 8

set under operation. Each discrete spike was distinguished by a successive number, namely green numbers indicate spikes coming from propeller and shaft lines, and black numbers show spikes coming from working main engines. Additionally, each discrete spike was distinguished by broken line, namely blue lines stand for the frequencies connected with work of main engines, and black lines - the frequencies connected with rotation of shaft line and propeller. The identification results obtained by using the method in question have been published many times [8, 12, 16]. This paper presents only a single analysis performed for a given working regime of ship propulsion system. The authors' archive contains results of identification of ships of different classes, made for various working regimes of their propulsion systems.

Among the relationships which are most commonly elaborated on the basis of such measurements, can be numbered the above presented characteristics of the sound pressure level in function of frequency, obtained for an arbitrary phase of ship's passing through the trial area, as well as the following:

- the sound pressure level in function of distance,
- the sound pressure level in function of ship forward speed and water depth,
- the relation between underwater noise and vibration of ship mechanisms.

The sample characteristic relation of sound pressure level in function of distance between ship and sensor, and of ship forward speed, is shown in Fig. 10 and 11. The curves were determined on the basis of many repeated measurements performed in the trial area located in the same place, and during the measurements of the ship crossing the trial area under the same work regime of its propulsion system. Results of the measurements were then subjected to relevant statistical

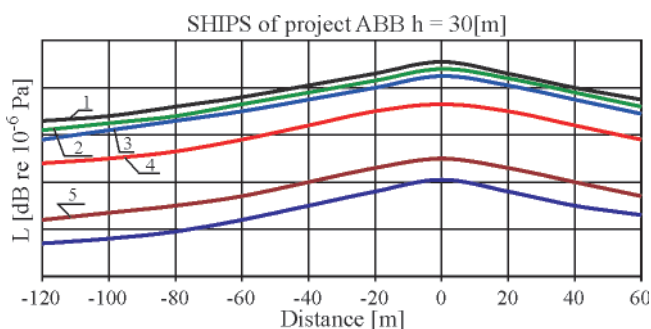


Fig. 10. The characteristic relation of the sound pressure level in function of distance between ship and acoustic sensor. Measurements of the ships were performed at the water depth  $h = 30$  [m]. **Notation:**  
 1 - the measurements performed at the speed  $v = 14.5$  [kn],  
 2 - the measurements performed at the speed  $v = 12.5$  [kn],  
 3 - the measurements performed at the speed  $v = 8.5$  [kn],  
 4 - the measurements performed at the speed  $v = 5.5$  [kn],  
 5 - the measurements performed at the speed  $v = 2.5$  [kn]

processing and approximating procedure. The approximation by means of polynomial of the second or third order is most commonly used to approximate the relation of pressure levels in function of ship distance, water depth and ship forward speed.

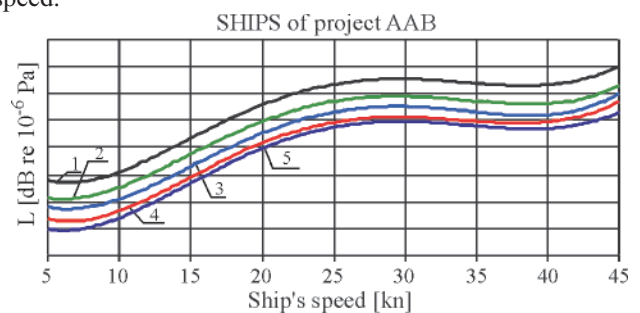


Fig. 11. The relation of the sound pressure level as a function of ship's forward speed. **Notation:**  
 1 - the measurements performed at the water depth  $h = 10$  [m],  
 2 - the measurements performed at the water depth  $h = 20$  [m],  
 3 - the measurements performed at the water depth  $h = 30$  [m],  
 4 - the measurements performed at the water depth  $h = 40$  [m],  
 5 - the measurements performed at the water depth  $h = 50$  [m]

In the paper possible ways of extending the measuring range due to a change in measurement methods, are mainly presented. To make performing the sound intensity measurements possible, the trial area was additionally equipped with a pair of sensors tested in laboratory, and positioned along the assigned path of ship through the area. In order to verify correctness of indications of the probe, the measurement results of noise propagating from the sensors of the probe were compared to each other, and the hydroacoustic pressure levels in the selected frequency bands were also compared.

The equal values of the levels obtained from the sensor probe, in the considered frequency bands, and given in the point ( $L = 138$  [dB],  $f = 930,6$  [Hz],  $t = 23,10$  [s]) distinguished by the cursor at the spectrograms, and the character of underwater noise distribution confirmed the possibility of conducting mutual analyses by the tested probe, which should enrich in consequence knowledge on underwater noise.

One of the fundamental features which differed the sound intensity measurement from the sound pressure one is the possibility of determining the phase differences between active and passive part of the sound field [3], which allows to determine direction of propagation of acoustic waves in water.

In view of the limitations imposed on the application of the measurement method in question, revealed by the equations (10) and (12), the frequency band for processing the measurement results was reduced from 6.9 [Hz] to 1.334 [kHz]. The accuracy of value of the level for the frequency of 6.9 [Hz] should not exceed 3 [dB], and for the upper frequency: 1 [dB].



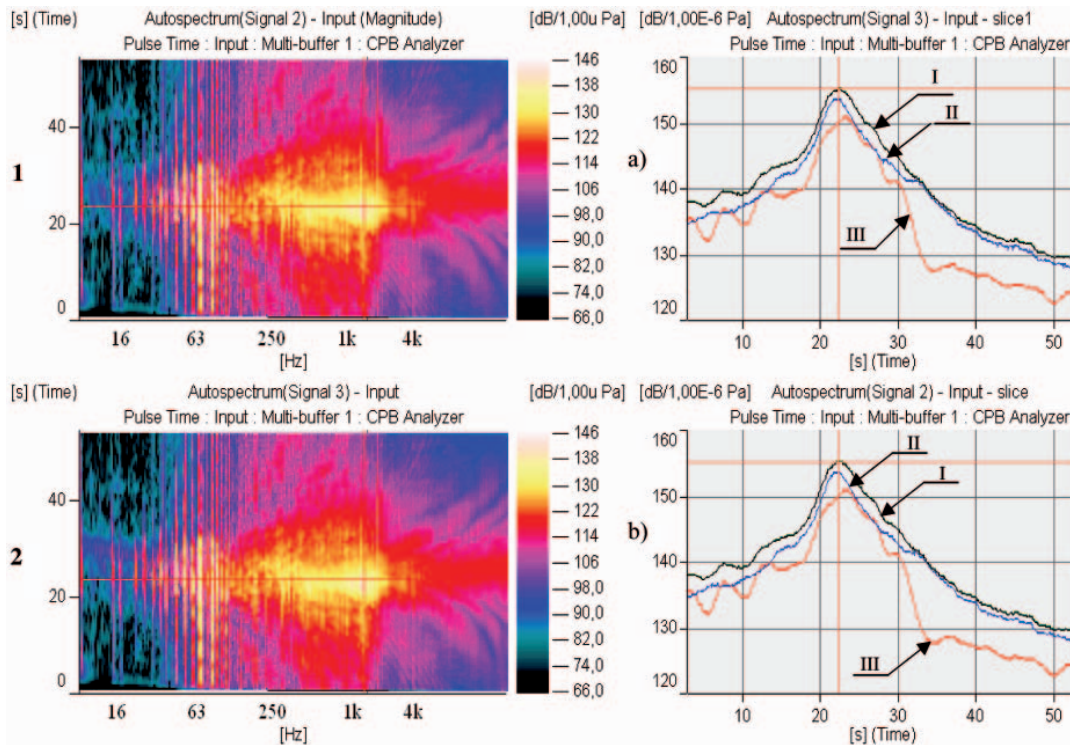


**Fig. 12.** The measurement results of hydroacoustic pressure recorded by using the probe for measuring the sound intensity of the ship moving with forward speed of 6.6 kn.

**Notation:** 1, 2 - the spectrograms of the ship acoustic field obtained from the sensor probe at the frequency band from 6.9 [Hz] to 11.22 [kHz],  
a, b - the relation of the pressure levels in function of duration time of ship passage through the trial area, obtained for the following frequency bands:  
I - the pressure value  $L = 155$  [dB] in the band from 6,9 [Hz] to 11.22 [kHz],  
II - the pressure value  $L = 154$  [dB] in the band from 100 [Hz] to 11.22 [kHz],  
III - the pressure value  $L = 151$  [dB] in the band from 6.9 [Hz] to 100 [Hz].

From the pressure measurements presented in the spectrogram of Fig. 12 the sound intensity was determined in accordance with the equation (1.6).

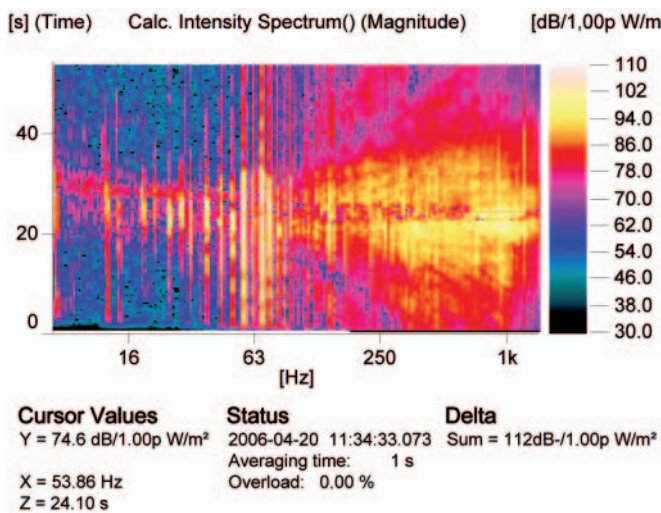


**Fig. 13.** The spectrogram of underwater noise intensity obtained in the frequency band from 6.9 [Hz] to 1.334 [kHz]

When testing the sound intensity amplitude of passage of the ship with the course of 0° relative to the location of the axis of the sensor probe, it should be demonstrated that on the basis of measurements in real conditions it is possible to precisely locate the place of passage of the ship above the set of acoustic sensors. To determine the location is possible because in laboratory conditions the value of sound pressure level falls to "0" for perpendicular position of the sound source relative to the probe. The phenomenon is described in many publications [4, 5, 6], and confirmed in laboratory tests carried out on the probe. A local depreciation of sound intensity revealed on the spectrogram are

visible for about 24 [s] duration time of passage of the ship above the probe. For different wave lengths we can observe of course different instants in which such local reduction of the sound intensity level would occur. The sound pressure level spectrum in function of time for the previously selected frequency ranges was produced to accurately reveal the local minimum values. In the spectra shown in Fig. 14, are clearly visible the local minimum values of the sound intensity level, by which perpendicular direction of hydroacoustic wave propagation relative to the probe in selected areas, is determined.

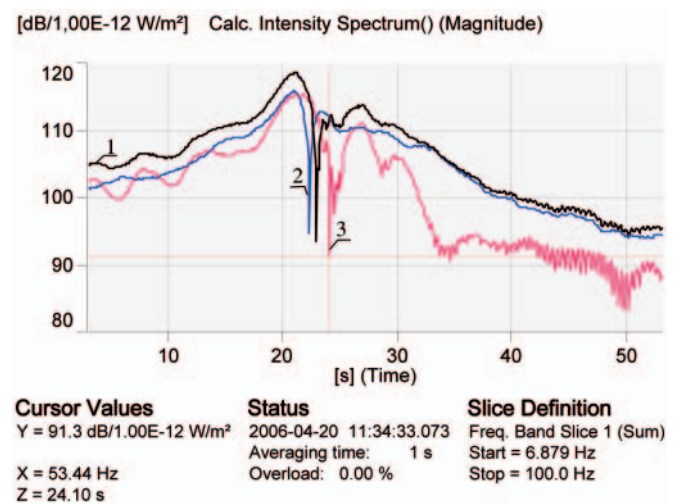


**Fig. 14.** The spectra of sound intensity level as a function of duration time of passage of the ship above the probe, obtained for the selected frequency bands: I - the minimum value of sound intensity level  $L = 93.4$  [dB], for the time  $t = 22.90$  [s], in the frequency band from 6.9 [Hz] to 1.334 [kHz]; 2 - the minimum value of sound intensity level  $L = 94.7$  [dB], for the time  $t = 22.30$  [s], in the frequency band from 100 [Hz] to 1.334 [kHz]; 3 - the minimum value of sound intensity level  $L = 91.3$  [dB], for the time  $t = 24.10$  [s], in the frequency band from 6.9 [Hz] to 100 [Hz]

The places of occurrence of local minimum values of sound intensity level determine a change of direction of energy flow to the probe. The change of direction can be showed by using the analysis of real part of complex spectra of sound intensity level. Results of the performed analysis is shown in Fig.15.

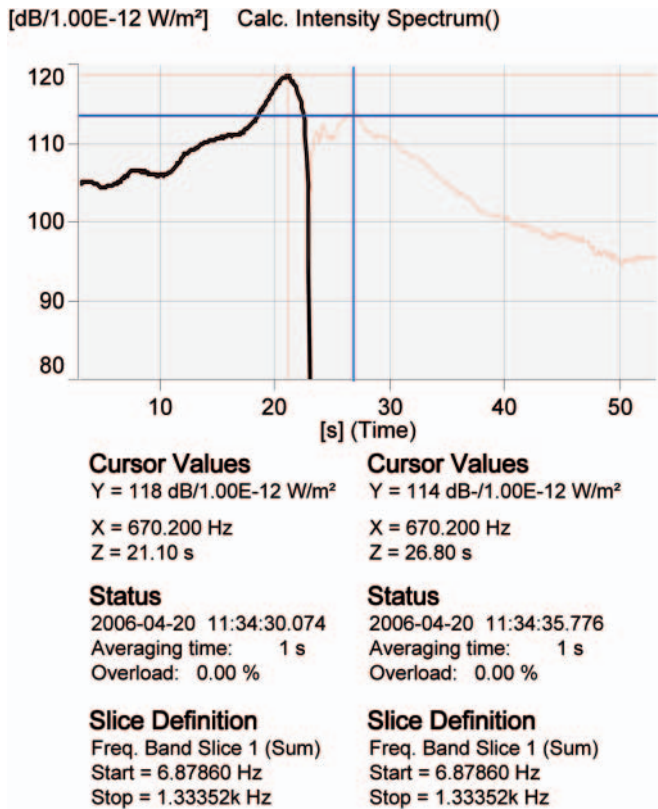


Fig. 15. The spectrum of real part of complex spectra of sound intensity level, performed in the frequency range from 6.9 [Hz] to 1.33 [kHz]

On the presented diagram of the analysis of absolute value of sound intensity level in function of duration time of passage of the ship above the probe the discussed change in energy flow direction is clearly visible. Positive value of sound pressure can be observed up to 22.90 [s] of duration time of passage of the ship through the trial area, represented by the black curve in Fig. 15. The black curve shows negative value of sound intensity. And, the maximum value of sound intensity  $L = +118$  [dB] re  $10^{-12}$  [W/m<sup>2</sup>] ( distinguished by cursor ) is observed at  $t = 21.10$  [s], and the minimum value  $L = -114$  - at  $t = 26.80$  [s]. The spectra obtained from the spectrogram presented in Fig. 13, which were taken for an arbitrary approaching time of ship to the probe and during its departure from the trial area, can also show the reversal of sign of sound intensity level.

From the spectra presented in Fig.16 and 17, the summary sound intensity levels equal to  $L = +113$  [dB] for the upper spectrum and  $L = -103$  [dB] for the lower spectrum, respectively, can be read. The reversal of sign of sound intensity level constitutes a confirmation that reversal of direction of energy flow to the sensor probe takes also place.

Reversal of direction of energy flow, determined from the measurement of difference of pressure values obtained from two hydroacoustic sensors makes it possible to determine direction of the source relative to location of the probe, within the sector from  $-90^\circ$  to  $+90^\circ$ . Determination of the source direction by means of this method is rather inaccurate.

Such measurement informs only whether the acoustic noise source is situated before the perpendicular plane located in half-distance between sensors, or behind it.

A more accurate bearing of the probe equipped with a pair of sensors can be obtained by testing both the sign of sound intensity and phase of the signal between the active and passive part of the sound field. For this purpose the tested noise was so processed as to obtain the spectrogram of amplitude of underwater noise phases, from which it was possible to determine the phase [°] within the considered frequency ranges.

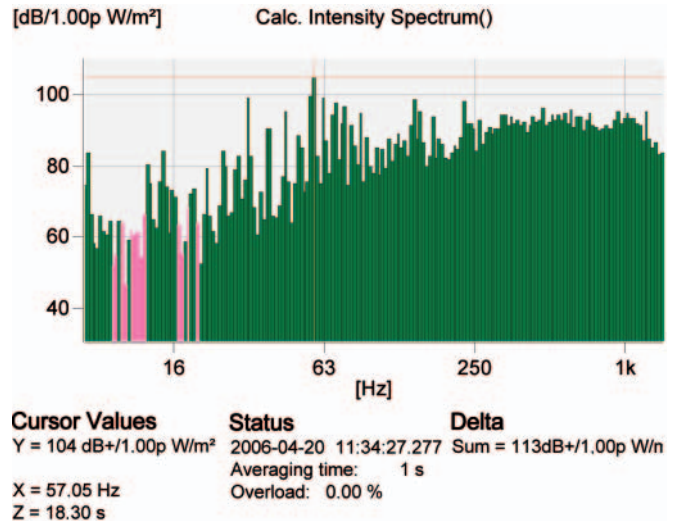


Fig. 16. Spectrum of sound intensity in function of frequency, obtained during approaching the ship to the probe.

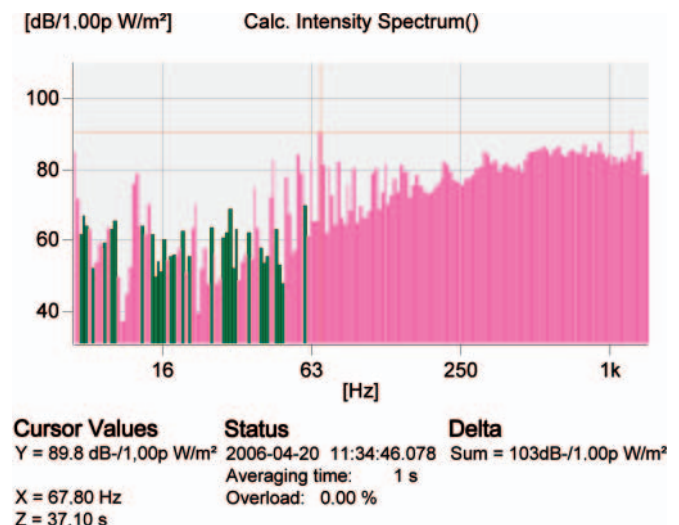


Fig. 17. The spectrum of sound intensity in function of frequency, obtained during departing the ship from above the probe

The spectrogram of phase amplitude of underwater noise (phase-assigned auto-spectrum) was calculated from the dependence:

$$\varphi_{xy} = \frac{\varphi_{xy}}{|\varphi_{xy}|} \quad (14)$$

where:

x = the active component of sound field,

y = the reactive component of sound field.

The spectra of underwater noise phases were determined in the selected frequency bands, Fig. 18.III. They are only useful in determining the sign of phase during performance of the measurement. The spectra were determined from the underwater noise phases, Fig. 18.II, for the whole duration time of the measurement. Examining the figures we can observe that



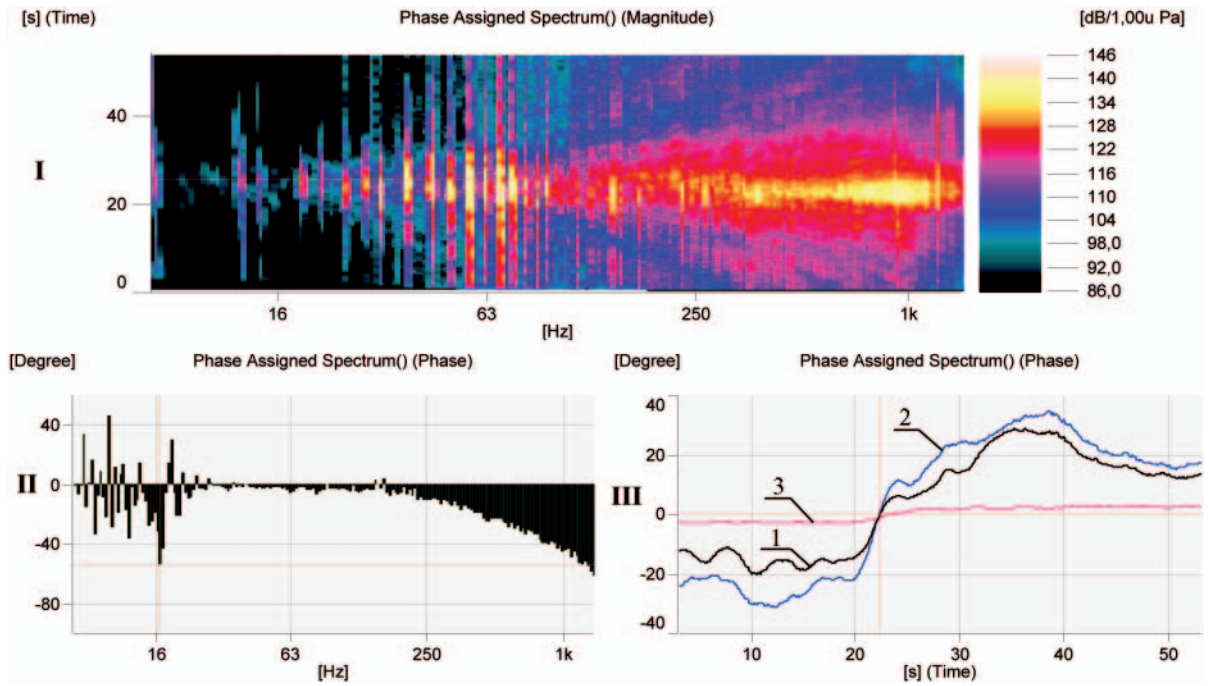


Fig. 18. I - the spectrogram of phase amplitude of underwater noise, II - the spectrum of phases of underwater noise, III - the spectrum of noise phases calculated for the selected frequency bands: 1 - that from 6.9 [Hz] to 1.334 [kHz], 2 - that from 100 [Hz] to 1.334 [kHz], 3 - that from 6.9 [Hz] to 100 [Hz]

during approaching the trial area by the ship to, at  $t = 23$  [s], the phase sign was negative, and behind the area - positive.

By comparing the spectra of sound intensity and signal phases it can be observed that during approaching the probe by the ship the sound intensity level obtains positive value and the phase - negative. The obtained positive values of sound intensity do not require any comments. The phenomenon is precisely described in many literature sources [1, 2, 4, 5, 6].

The auxiliary Fig. 19 can be used to explain how to use sign value for a more accurate location of sound sources.

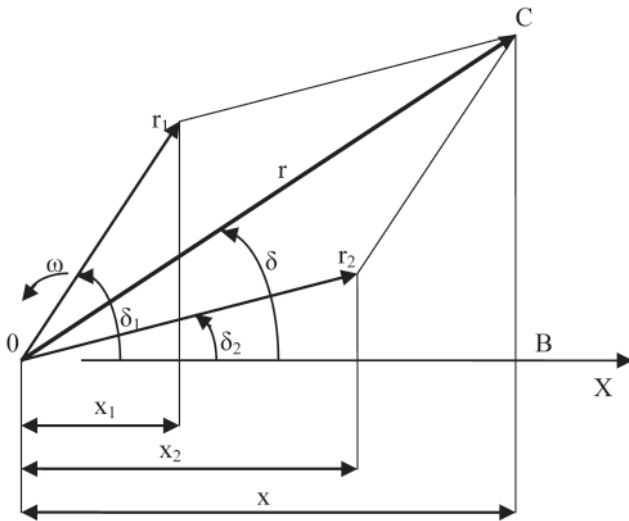


Fig. 19. Summation of vectors of waves of different amplitudes and initial phases. **Notation:**  $x_1$  - the deflection of the active component of the sound field wave amplitude  $r_1$ , initial phases  $\delta_1$  and angular velocity  $\omega$ ,  $x_2$  - the deflection of the passive component of the sound field wave amplitude  $r_2$ , initial phases  $\delta_2$  and angular velocity  $\omega$ ,  $x$  - the deflection of wave resulted from summation of component vectors of active and passive sound field

From Fig. 19 we can easily determine the phase of the signal by using the dependence:

$$\operatorname{tg} \delta = \frac{BC}{OB} = \frac{r_1 \sin \delta_1 + r_2 \sin \delta_2}{r_1 \cos \delta_1 + r_2 \cos \delta_2} \quad (15)$$

From principles of trigonometry it is known that tangent function takes positive values in the 1st and 3rd quadrant, and negative - in the 2nd and 4th one.

Based on the knowledge of sign of sound intensity level and signal phase, a sound source can be located in an appropriate quadrant determined by the coordinates of sensor probe. The pictorial scheme of the location of the sound source in the relevant quadrant determined by pair of acoustic sensors, is shown in Fig. 20.

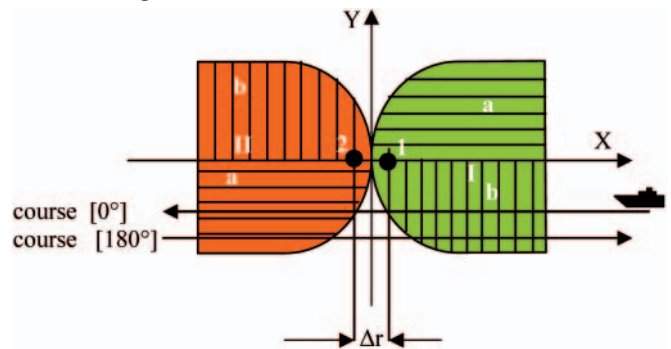


Fig. 20. The location of ship in the relevant quadrant determined by the sensor probe coordinates, during ship's passage trough trial area. **Notation:** I - the area of positive values of sound intensity level, II - the area of negative values of sound intensity level, a - the quadrant of positive values of the sound field phase, b - the quadrant of negative values of the sound field phase, 1, 2 - the hydroacoustic sensors

After the measurements carried out for the course of  $0$  [°] relative to the location of probe acoustic sensors, the measurements for the course of  $180$  [°] were performed. During the measurements the ship did not changed the area covered by the tests, against the location of the sensors axis, as shown in Fig. 18. From the tests the spectrogram of underwater noise intensity and spectrum of sound intensity in function of duration time of ship passage through the trial area, were achieved. In the spectrum it is clearly visible that when the ship approaches the probe (up to  $t = 43$  [s]) sound pressure levels take negative values, and positive ones during the ship's departure from it. From comparison of the results of the measurements taken for

the course of 0 [°] and 180 [°], the difference in signs of the sound intensity level and phase during approaching the probe by the ship and departing from it, is clearly visible.

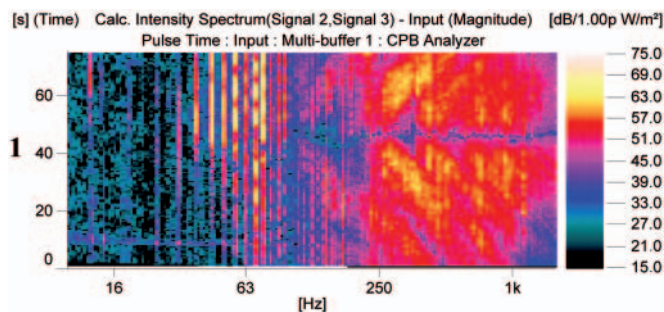


Fig. 21. The spectrogram of underwater noise intensity recorded in the frequency band from 6.9 [Hz] to 1.334 [kHz]

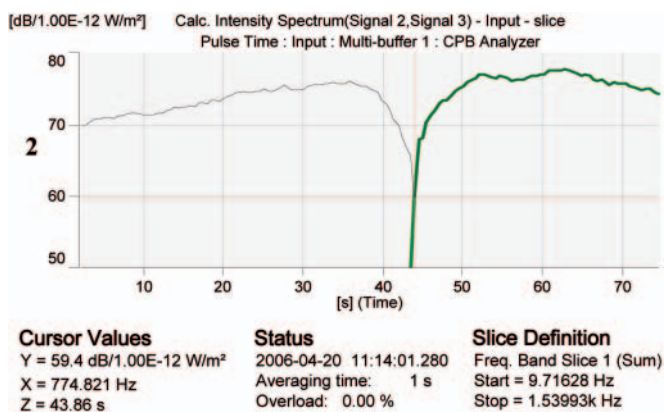


Fig. 22. The analysis of the real part of complex spectrum of sound intensity, performed in the frequency band from 6.9 [Hz] to 1.33 [kHz]

On determination of the sound intensity, the determining of signal phases whose results are presented in Fig. 23 and 24, has been started.

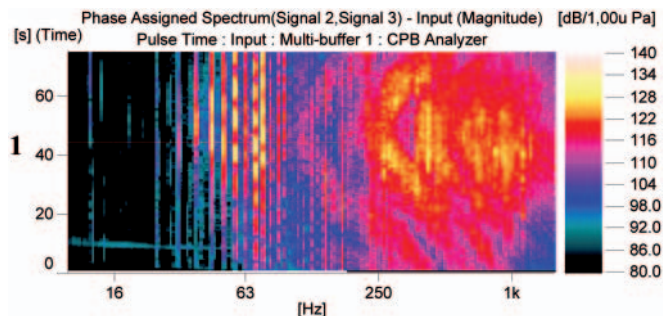


Fig. 23. The phase amplitude spectrogram of underwater noise, recorded in the frequency band from 6.9 [Hz] to 1.334 [kHz]

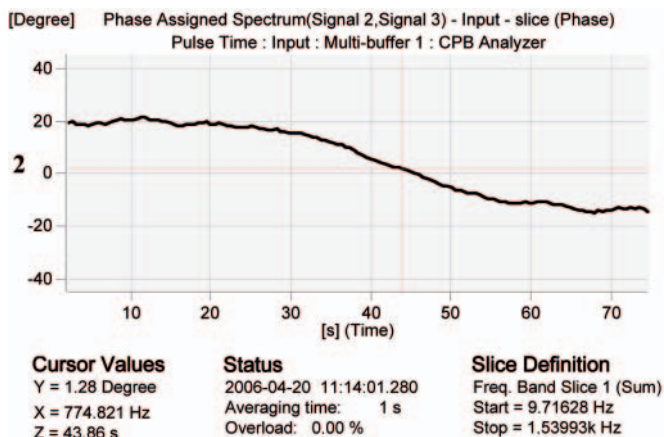


Fig. 24. The spectra of phase amplitude signals of underwater noise, recorded in the frequency band from 6.9 [Hz] to 1.334 [kHz]

Comparing the results of phase measurements carried out for the tested courses, one obtained also the difference in signs, which confirms that to determine ship's course relative to sensors is possible.

## CONCLUSIONS

The results of the performed research have demonstrated that by testing the sign of the sound intensity level and phase of noise signals it is possible to locate sound source just in a relevant quadrant determined by the sensor probe coordinates. To achieve a better accuracy is possible by increasing the number of pairs of sensors and spacing them properly. The use of three sensors located in an equilateral triangle will make it possible to reduce the sector of sound source location to 30 [°].

As demonstrated in the paper, the probe applied to measuring the sound intensity will make it possible to supplement the so far collected results of underwater noise investigations carried out in shallow waters by knowledge on direction of propagation of hydroacoustic waves.

On the basis of known values of sound pressure and intensity it is possible to elaborate the following characteristics:

- the noise spectral structures of vessels,
- the results of vibration of mechanisms and equipment installed on ships, which greatly affect spectral structure of ship acoustic field (main engines, generators, shaft lines, screw propeller),
- the results of research on the relationship between ship underwater noise and vibration of ship mechanisms,
- initial assessment of technical state of ship machinery,
- estimation of the energy transmission coefficient,
- the measurement results of sound pressure level changes in function of ship's forward speed,
- the results of sound pressure level changes in function of distance,
- presentation of the acoustic wave propagation model made for water depth values selected along ship's trajectory,
- determination of direction of propagation of hydroacoustic waves.

This paper has an experimental character and constitutes a continuation of many other investigations in the subject-matter area [7 ÷ 18].

In the future a series of extensive studies should be conducted, on the basis of which the maximum distance from which to identify and locate particular vessels is still possible, could be determined. The investigations should be performed in the coastal zone, at different sea states and different levels of hydroacoustic background noise, as well as in the trial areas located in the Gdansk Bay, at different water depths.

## BIBLIOGRAPHY

- Kozaczka E., Grelowska G., Bittner P., Baranowska A., Milanowski W., Dobrzaniecki J.: *Spatial distribution of underwater noises radiated by ship to hemisphere and its standardization* Gdynia 1997
- Kozaczka E., Grelowska G., Gloza I., Dobrzaniecki J.: *Determination of phase displacement of hydrophone. Control measurements in a test tank and at sea*, Hydroacoustics, Volume 3, Gdynia 2000
- Bulletin of Brüel & Kjær, 1973
- Elliot S.J.: *Errors in Acoustic Intensity Measurements*. Journal of Sound and Vibration 1982
- Thompson J.K. & Tree D. R.: *Finite difference approximation errors in acoustic intensity measurements*. Journal of Sound and Vibration 1981

6. Jacobson F.: *Measurement of sound intensity*. Acoustics Laboratory of the Danish Technical University.
7. Kozaczka E., Grelowska G., Bittner P., Baranowska A., Kiciński W., Milanowski W.: *Spatial distribution of underwater noise radiated by ship to hemisphere*. STAGE II, Proceedings of 9th Symposium on Hydroacoustics, Gdynia 1992
8. Baranowska A., Gloza I.: *Identification of underwater disturbance sources with using the coherence function*. Proceedings of 48th Open Seminar on Acoustics, Wroclaw 2001
9. Dobrzaniecki., Gloza I., Domagalski J.: *Preliminary research on monitoring the own ship noise*, Proceedings of 50th Open Seminar on Acoustics, Szczyrk – Gliwice 2003.
10. Gloza I.: *The investigation of changes of ships underwater noise in shallow sea*, Doctoral thesis, Polish Naval Academy, Gdynia 1994
11. Gloza I.: *Experimental research of noise generated by ship's engine*, Proceedings of 6th Symposium on Hydroacoustics, Gdynia 1989
12. Gloza I.: *Assessment of technical state of ships propulsion system on the basis of measurement of hydroacoustic noise*. Proceedings of 10th Symposium on Hydroacoustics, Gdynia 1993
13. Gloza I., Malinowski S.: *Identification of ships underwater noise sources in the coastal region*. Hydroacoustics, Vol. 5/6, 2003.
14. Gloza I., Domagalski J.: *The investigation of propagation of acoustic waves generated by moving ship*. Hydroacoustics, Vol. 5/6, 2003.
15. Gloza I., Domagalski J., Malinowski S.: *The character of underwater noise radiated by small vessels*. Hydroacoustics, Vol. 4, 2001.
16. Gloza I., Domagalski J., Malinowski S.: *Identification of ships underwater noise sources in near field*. Proceedings of 49th Open Seminar on Acoustics, Warszawa - Stare Jablonki 2002
17. Gloza I., Domagalski J., Dobrzaniecki J.: *The structure of acoustics field of vessel's underwater noise in near field*. Proceedings of 48th Open Seminar on Acoustics, Wroclaw 2001
18. Grelowska G., Bittner P.: *The processing of underwater signals produced by ship with the possibility of increasing the frequency resolution*. Scientific Bulletin of Polish Naval Academy, vol. XXXIV, 4, 1994.

---

#### CONTACT WITH THE AUTHORS

Eugeniusz Kozaczka, Prof.,  
Faculty of Ocean Engineering  
and Ship Technology  
Gdansk University of Technology  
Narutowicza 11/12  
80-233 Gdansk, POLAND  
fax: (058) 347-21-81,  
e-mail: kozaczka@pg.gda.pl

Jacek Domagalski, Ph. D.  
Ignacy Gloza, Ph. D.  
Faculty of Navigation and Naval Weapons,  
Polish Naval Academy  
Śmidowicza 69  
81-103 Gdynia POLAND  
e-mail: i.gloza@amw.gdynia.pl



# Mathematical model of radial passive magnetic bearing

**Leszek Matuszewski**, Ph.D.  
Gdansk University of Technology  
**Krzysztof Falkowski**, Ph.D.  
Military University of Technology, Warsaw

## ABSTRACT

*In the article a mathematical model of radial passive magnetic bearings applicable to ocean engineering units has been presented. The application of the bearings in ship thrusters should increase durability of propulsion systems and give lower maintenance costs. The rotor of thruster's electric motor is suspended in magnetic field generated by radial passive magnetic bearings. However the maintaining of axial direction of the rotor must be controlled with electromagnets equipped with a high-dynamic controller. The risk of application of the magnetic bearings results from very low stiffness of the unit in comparison with rolling bearings. Also construction of the bearing should be different due to gyroscope effect and high forces generated during ship manoeuvring. The physical model performs correctly if electromagnets are controlled properly; and, technological problem with sealing system seems more significant than power supply to electromagnets winding. The equations presented in the article are necessary to build algorithms of a digital controller intended for on-line controlling magnetic bearing in axial direction.*

**Keywords:** propeller, ring motor, magnetic bearing

## INTRODUCTION

Possible application of magnetic bearings to ocean engineering units has been considered and tested for several years. Their low resistance to rolling and very long life time is of a great advantage. However because of a small stiffness they require introducing constructional changes into existing devices and new designed ones to be fitted with the so-called floating rotor. The bearing system presented in this paper is superior, as regards its durability, to traditional mechanical bearings both sliding and rolling ones. The most promising example of application of such bearing is the using it for ship main propulsion shaft line or thruster. In recent years fast development of engineering of polymer materials and their growing application to sea-water-lubricated slide bearings, has been observed. However the application of passive magnetic bearing of Halbach's configuration provides a comparably high stiffness of supporting, and simultaneously lack of wear-out phenomenon of interacting surfaces under operation.

The magnetic bearing is a device which makes use of repelling forces between homopolar magnets simultaneously placed in front to each other and coaxially, which keep rotor against stator in the state of levitation. Multi-row arrangement of magnetic rings provides a higher stiffness of bearing unit and more stable work in the neighbourhood of point of operation [1]. The levitation means keeping the rotor supported without any mechanical contact between it and stator. The main advantage of such bearings is elimination of friction forces between interacting elements. In the commonly used rolling and sliding bearings friction phenomena as such is not eliminated but only reduced. Moreover, in the traditional bearing systems

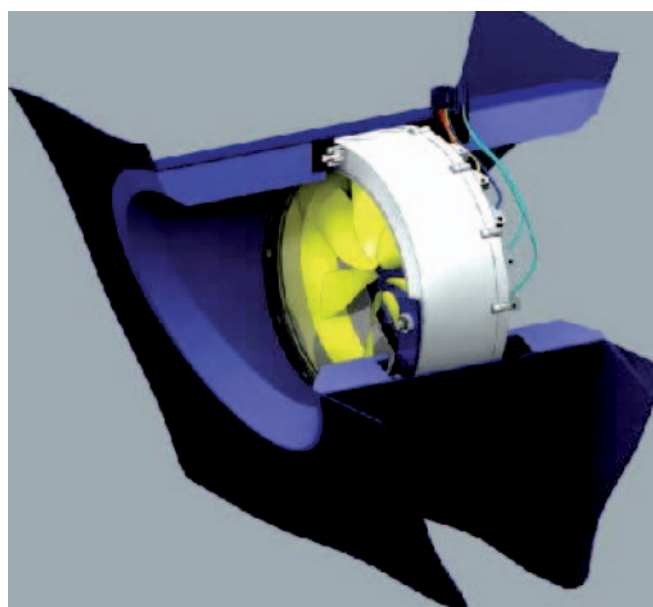


*Fig. 1. Thruster based on a slip-ring motor*

additional systems responsible for lubricating, cooling and discharging wear products are necessary. As results from the presented characteristics the application of classical bearings to operation in the environments more aggressive to materials or in a high vacuum meets significant difficulties and limitations. Therefore it is recommended, wherever justified, to apply magnetic suspensions which do not require additional systems, can operate in chemically active environments, and eliminate friction, extending this way life time of traditional bearings.



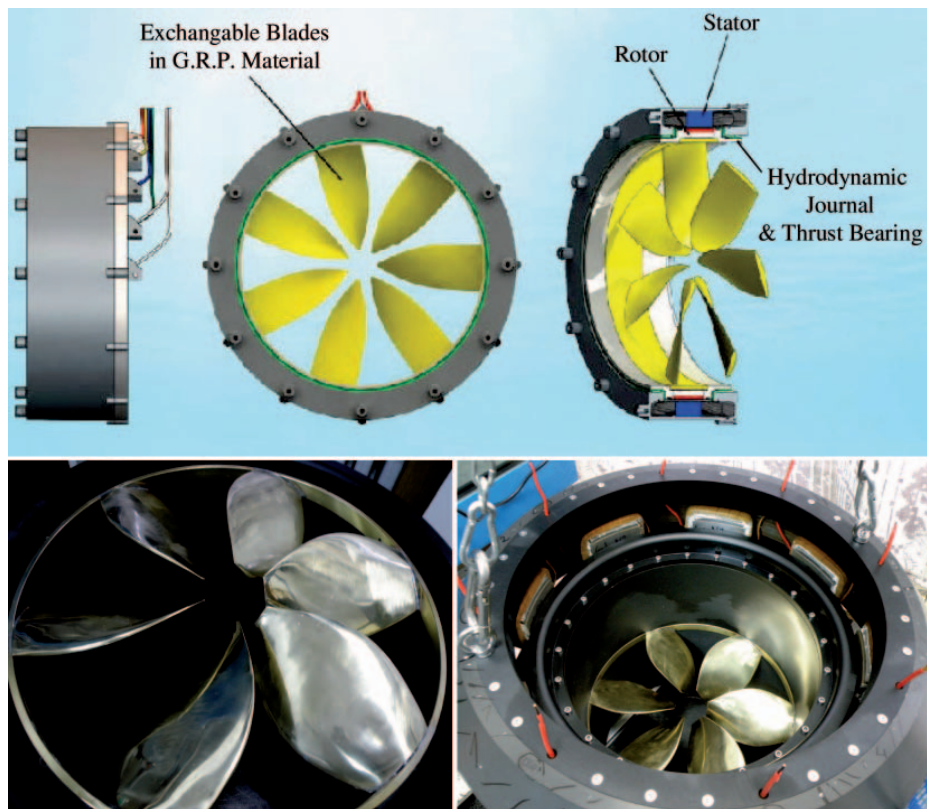


Fig. 2. Overall view of a Rim Drive device and the model intended for trials

Magnetic bearings are split in two basic groups: active and passive ones. The first group covers active bearings in which magnetic force value is proportional to position of rotor centre against hole centre and this way inversely proportional to value of a gap between interacting parts. In active bearing system the following items can be always found [3]:

- a sensor intended for the measuring of rotor position within air gap,
- a controller which transforms information on rotor position into steering signals,
- an amplifier which, on the basis of the steering signals, changes value of magnetic force by changing value of electric current flowing through active bearing coils in axial direction.

As results from the presented design of magnetic bearing, the rotor position stabilization is realized by the system of feed-back between rotor position and magnetic force.

Passive magnetic bearings belong to the second group. In design of such bearings there is no feed-back system between rotor position within air gap and value of magnetic force. In design of passive bearings permanent magnets are used to produce magnetic forces [4].

The main advantage of passive bearings is its simple design, very high efficiency (as such bearings do not absorb energy during operation and provide simultaneously magnetic levitation) and relatively low cost. Nevertheless the lack of a feed-back system does not ensure a stable position of rotor around a given working point and does not make it possible to control its position within air gap. Active bearings are to be used in any case where a decisive condition is to maintain high precision in rotor positioning. Moreover it is not possible to build a fully isolated magnetic suspension system on the basis of only passive magnetic bearings (acc. Earnshaw theorem) [5]. Therefore in any solution of magnetically suspended rotor at least one actuator is to be active, and the remaining can be passive ones [6].

Hence for the bearing system of water propeller rotor it was proposed to apply two radial passive magnetic bearings and one axial active bearing. The bearing system is presented in Fig. 3.

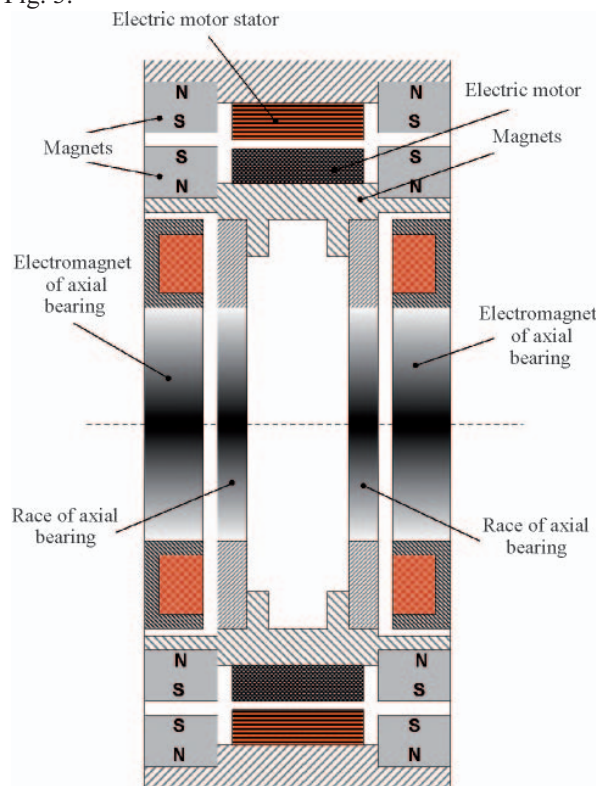


Fig. 3. Bearing system for water propeller rotor

In this paper a mathematical model of radial passive magnetic bearing is presented. Evaluation of the model is necessary to elaborate design algorithms for passive magnetic bearings.

## PASSIVE MAGNETIC BEARING

Two magnets or two sets of magnets are used to form a passive magnetic bearing [5]. In the simplest case two magnets repelling each other are used. One of them is rigidly connected with casing of rotary motor. It cannot displace. The other one is placed onto free rotor and can do, together with it, a complex motion being a sum of translational and rotational displacements. The moving magnet has six degrees of freedom and behaves as a magnetic compass needle which tries to be always lined up along external magnetic field lines (Fig. 4). As in the classical magnetic bearing there is a stator fixed in machine casing (motionless magnet) and a race placed in rotor (moving magnet). Between races of rolling bearing there are balls placed in bearing cage, and in slide bearing oil film appears between its races. In passive magnetic bearing a medium in which the bearing operates, is used. If a bearing operates in high vacuum conditions then between its races vacuum occurs, and a bearing immersed in water contains water between its races. This feature of magnetic bearing is one of its crucial merits. Obviously, apart from an environmental medium also magnetic field occurs between bearing stator and race.

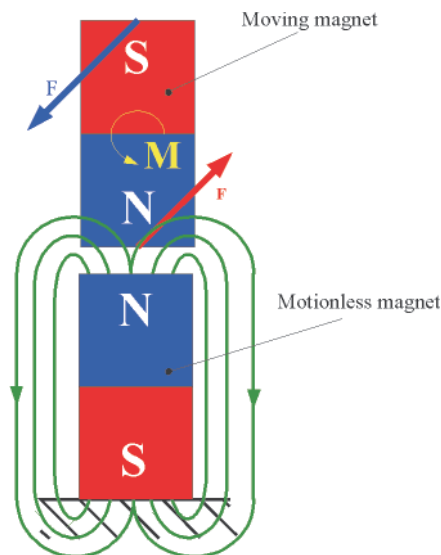


Fig. 4. Arrangement of magnets in repelling system

It can be assumed that in passive magnetic bearing the permanent magnet which does not displace is a source of non-uniform magnetic field. And, the permanent magnet connected with the rotor lines up along lines of external magnetic field generated by the magnet fixed in rotary machine casing [7].

As the magnet fixed in rotor behaves like a magnetic needle it tries to rotate its north pole towards south pole of the motionless magnet and shift its south pole so as to place it close to north pole of the motionless magnet. Magnet placed in a non-uniform magnetic field does a complex motion and its trajectory depends on initial position of moving magnet against that motionless. If magnets point to each other with opposite poles then they will try to be mutually connected. After connection the two magnets will behave as one magnet which becomes a magnetic dipole. If an orientation of the magnets is different from that above mentioned, then the magnet will rotate until they point to each other with opposite poles and then connect mutually. The connection of the magnets means that they reach state of equilibrium, hence such mutual position of the two magnets appears stable [7].

Any rotary displacement of rotor within magnetic bearing and mutual connection of its magnets would lead to a failure of rotary machine and its bearing. Only the maintaining of magnets in the position in which repelling forces between magnets occur, makes bearing work correct. The mutual repelling process of the magnets is a state of instable equilibrium, i.e. the state in which the system maintains its stability but with no stability margin.

The bearing intended for the transferring of radial loads consists of two magnets concentrically located (Fig. 5a). The bearing magnets are radially magnetized. The same magnetic pole takes place both on the outer circumference wall of the magnet fixed in machine rotor and on the inner circumference wall of the magnet fixed in machine casing. Such solution makes it possible to generate mutual repelling the magnets and this way magnetic levitation of the rotor to be suspended. As the manufacturing of uniform radially magnetized ring magnets is difficult, also bearings of rings built with segments, can be found. Such segment is a ring sector which is to be magnetized radially (Fig. 5b). Due to technological reasons it is not possible to produce an one-sided radial bearing. Radial bearings are always manufactured in a differential system.

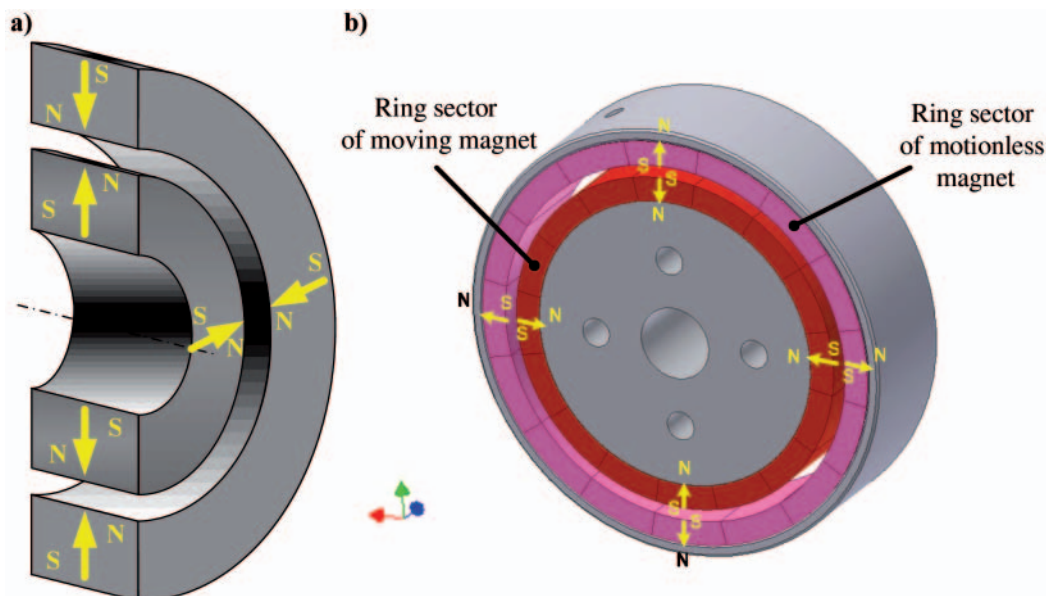


Fig. 5. Radial passive magnetic bearing

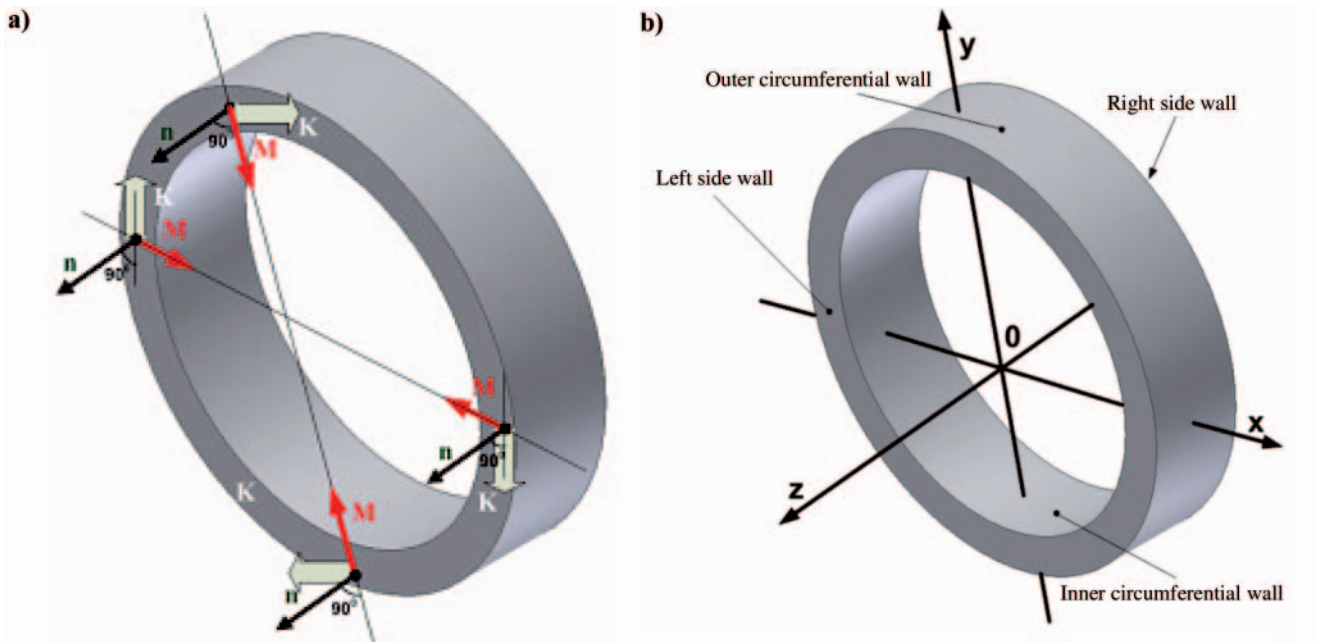


Fig. 6. Surface current constrained within side wall (6a), coordinate frame orientation in the magnet (6b)

### MODEL OF RADIAL PASSIVE BEARING

Amper model was used for description of a model of magnetic interaction between two ring magnets. As assumed in the model in the magnet walls flow constrained currents being a source of magnetic field. Value of the constrained currents depends on the product of magnetization vector and that perpendicular to magnet wall [2]:

$$\vec{K} = \vec{M} \times \vec{n} \quad (1)$$

where:

$\vec{M}$  – magnetization vector

$\vec{n}$  – vector perpendicular to magnet wall.

Fig. 6 illustrates surface currents constrained within ring magnet. As results from the relation (1) the currents will occur in side walls only. They will not occur on the outer and inner circumferential walls of the magnet.

In compliance with Lorentz principle [2] the magnetic interaction force depends on the vector product of the surface constrained current and the vector of magnetic induction which penetrates the moving magnet:

$$\vec{F}(x, y, z) = \int (\vec{K}' \times \vec{B}) da' \quad (2)$$

where:

$\vec{K}'$  – surface constrained current flowing through a given sector of the moving magnet,  $da'$

$\vec{B}$  – vector of magnetic induction which penetrates the moving magnet sector of the surface area  $da'$  [in the point of the coordinates  $(x, y, z)$ ].

Fig. 6a presents the ring magnet with depicted surface currents. In the ring magnets the currents appear both in the left and right wall (Fig. 6b).

For radially magnetized ring magnet the magnetization vector is equal to [4]:

$$\vec{M}' = [M'_x \quad M'_y \quad 0] = [M' \cos \varphi \quad M' \sin \varphi \quad 0]$$

The normal vector can be expressed as:

$$\vec{n} = [0 \quad 0 \quad 1]$$

The surface current in the left wall amounts to:

$$\vec{K}'_1 = \begin{bmatrix} \vec{i} & \vec{j} & \vec{k} \\ M' \cos \varphi' & M' \sin \varphi' & 0 \\ 0 & 0 & 1 \end{bmatrix} = M' \sin \varphi' \vec{i} - M' \cos \varphi' \vec{j} \quad (3)$$

$$\vec{K}'_2 = [M' \sin \varphi' \quad -M' \cos \varphi' \quad 0]$$



The surface current in the right wall of moving magnet is described as follows:

$$\vec{K}'_p = \begin{bmatrix} \vec{i} & \vec{j} & \vec{k} \\ M' \cos \varphi' & M' \sin \varphi' & 0 \\ 0 & 0 & -1 \end{bmatrix} = -M' \sin \varphi' \vec{i} + M' \cos \varphi' \vec{j} \quad (4)$$

$$\vec{K}'_p = [-M' \sin \varphi' \quad M' \cos \varphi' \quad 0]$$

The vector product of the surface current flowing through the left wall of moving magnet and the magnetic induction in the point of the coordinates  $(x, y, z)$ , is equal to:

$$\vec{K}'_1 \times \vec{B} = \begin{bmatrix} \vec{i} & \vec{j} & \vec{k} \\ M' \sin \varphi' & -M' \cos \varphi' & 0 \\ B_x(x, y, z) & B_y(x, y, z) & B_z(x, y, z) \end{bmatrix} = \quad (5)$$

$$= -B_z(x, y, z) M' \cos \varphi' \vec{i} - B_z(x, y, z) M' \sin \varphi' \vec{j} + M' (B_y(x, y, z) \sin \varphi' + B_x(x, y, z) \cos \varphi') \vec{k}$$

The surface area  $da'$  of an elementary sector of magnet side wall can be estimated as follows (Fig.7):

$$da' = r' d\varphi' dr' \quad (6)$$

where:

$r'$  – the mean radius changeable within the interval  $r'_1 < r' < R'$

$\varphi'$  – the angle changeable within the interval  $0 < \varphi' < 2\pi$

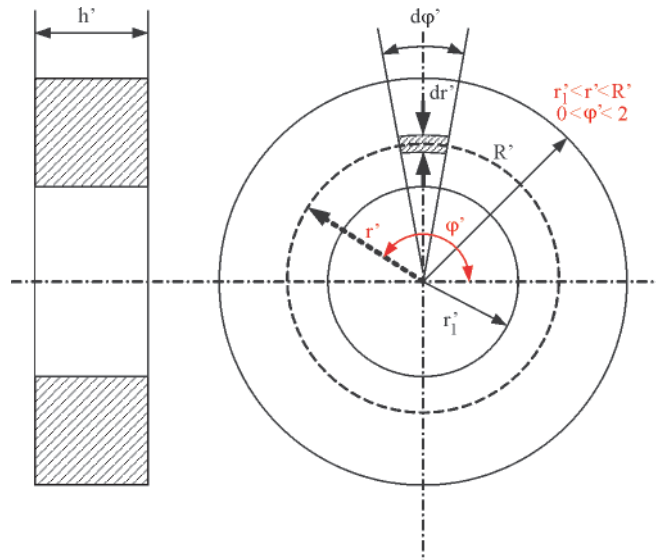


Fig. 7. The sector considered on the moving magnet side wall

By taking into account the above given relations in the Lorentz force (2) the following value of the force on the left wall is obtained:

$$\vec{F}_1(x, y, z) = - \iint B_z(x, y, z) M' \cos \varphi' r' d\varphi' dr' \vec{i} - \iint B_z(x, y, z) M' \sin \varphi' r' d\varphi' dr' \vec{j} + \iint M' (B_y(x, y, z) \sin \varphi' + B_x(x, y, z) \cos \varphi') r' d\varphi' dr' \vec{k} \quad (7)$$

In the same way the magnetic force value in the points located on the moving magnet right wall, can be found:

$$\vec{F}_p(x, y, z) = \iint B_z(x, y, z) M' \cos \varphi' r' d\varphi' dr' \vec{i} \iint B_z(x, y, z) M' \sin \varphi' r' d\varphi' dr' \vec{j} + \iint M' (B_y(x, y, z) \sin \varphi' + B_x(x, y, z) \cos \varphi') r' d\varphi' dr' \vec{k} \quad (8)$$

By using Biot-Savart principle magnetic induction in the point  $p$  of the coordinates  $(x, y, z)$  located in the space around motionless magnet (magnetic field source), can be determined. Points for which magnetic induction is calculated for further analysis are placed on the moving magnet. Biot-Savart principle for surface currents flowing through motionless magnets takes the following form [2]:



$$\vec{B}(\mathbf{p}) = \frac{\mu_0}{4\pi} \int \frac{\mathbf{K}(\mathbf{p}') \times \vec{P}}{|\vec{P}|^2} d\mathbf{a} \quad (9)$$

where:

$\hat{P}$  - versor of vector directed opposite to the surface on which surface constrained current flows to the point for which value of magnetic induction has to be determined.

The vector  $\vec{P}$  can be written as follows:

$$\vec{P} = |\vec{P}| \hat{P} \quad (10)$$

The relation can be transformed into the form:

$$\hat{P} = \frac{\vec{P}}{|\vec{P}|} \quad (11)$$

By accounting for Eq.(11) in Eq.(9) the relation for magnetic induction is obtained as follows:

$$\vec{B}(\mathbf{p}) = \frac{\mu_0}{4\pi} \int \frac{\mathbf{K}(\mathbf{p}') \times \vec{P}}{|\vec{P}|^3} d\mathbf{a} \quad (12)$$

Value of the magnetic induction depends on the vector  $\vec{P}$ , therefore its coordinates between the point located on the circular loop circumference and the spatial point  $p'$  ( $x, y, z$ ), should be estimated. The coordinates of the point  $p'$  located on the circular loop circumference are as follows:

Coordinates for the left wall, $p'_1(x'_1, y'_1, z'_1)$	Coordinates for the right wall, $p'_p(x'_p, y'_p, z'_p)$
$x'_1 = r \cos \varphi$	$x'_p = r \cos \varphi$
$y'_1 = r \sin \varphi$	$y'_p = r \sin \varphi$
$z'_1 = \frac{h}{2}$	$z'_p = -\frac{h}{2}$

The coordinates of the vector  $\vec{P}$  for the left wall are equal to:

$$\vec{P}_1 = [x - x'_1 \quad y - y'_1 \quad z - z'_1]$$

and, for the right wall, as follows:

$$\vec{P}_p = [x - x'_p \quad y - y'_p \quad z - z'_p]$$

where:

$x, y, z$  – coordinates of the point for which value of magnetic induction has to be determined.

Finally the coordinates of the vector  $\vec{P}$  take the form:

$$\vec{P}_1 = \left[ x - r \cos \varphi \quad y - r \sin \varphi \quad z - \frac{h}{2} \right]$$

$$\vec{P}_p = \left[ x - r \cos \varphi \quad y - r \sin \varphi \quad z + \frac{h}{2} \right]$$

The module of the vector  $|\vec{P}_1|$  takes the value:

$$|\vec{P}_1| = \sqrt{x^2 + y^2 + z^2 - 2r(x \cos \varphi + y \sin \varphi) - zh + r^2 + \frac{h^2}{4}} \quad (13)$$

And, the vector  $|\vec{P}_p|$  is equal to:

$$|\vec{P}_p| = \sqrt{x^2 + y^2 + z^2 - 2r(x \cos \varphi + y \sin \varphi) + zh + r^2 + \frac{h^2}{4}} \quad (14)$$

For the radially magnetized ring vector the magnetization vector amounts to:

$$\vec{M} = [M_x \quad M_y \quad 0] = [M \cos \varphi \quad M \sin \varphi \quad 0]$$

The values of surface current in the motionless magnet left and right walls are the following, respectively:

$$\vec{K}_1 = [M \sin \varphi \quad -M \cos \varphi \quad 0]$$

$$\vec{K}_p = [-M \sin \varphi \quad M \cos \varphi \quad 0]$$

The vector product of the surface current  $\vec{K}_1$  and the vector  $\vec{P}_1$  is equal to:

$$\vec{K}_1 \times \vec{P}_1 = \left[ -M \cos \varphi \left( z - \frac{h}{2} \right) \quad -M \sin \varphi \left( z - \frac{h}{2} \right) \quad M(x \cos \varphi + y \sin \varphi - r) \right] \quad (15)$$

In the similar way the vector product of the surface current  $\vec{K}_p$  and the vector  $\vec{P}_p$  can be determined:

$$\vec{K}_p \times \vec{P}_p = \left[ M \cos \varphi \left( z + \frac{h}{2} \right) \quad M \sin \varphi \left( z + \frac{h}{2} \right) \quad -M(x \cos \varphi + y \sin \varphi - r) \right] \quad (16)$$

For the analysis is used the magnet sector  $da$  limited by the arc of the angle  $d\varphi$  and the vector increment  $dr$ .

The surface area of the sector is equal to:

$$da = r d\varphi dr$$

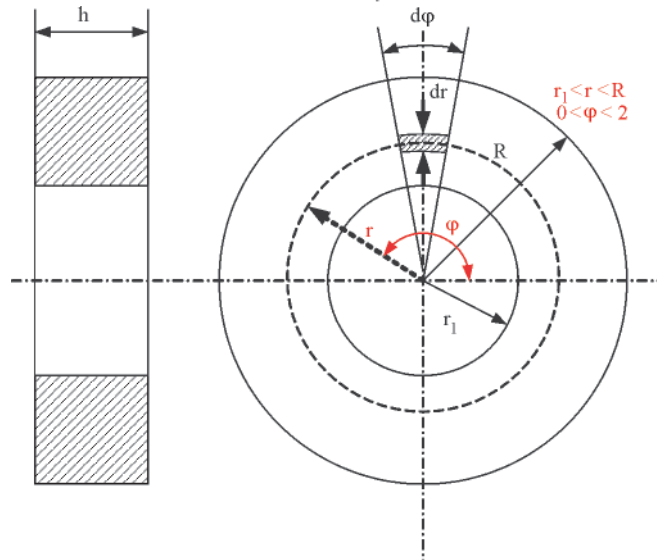


Fig. 8. The sector considered for the motionless magnet side wall

The magnetic induction value in the point p of the coordinates (x, y, z) is equal to:

$$\vec{B}(x, y, z) = \frac{\mu_0}{4\pi} \left\{ \int \frac{\vec{K}_1 \times \vec{P}_1}{|\vec{P}_1|^3} da + \int \frac{\vec{K}_p \times \vec{P}_p}{|\vec{P}_p|^3} da \right\} \quad (17)$$

By taking into (17) account the relations (13), (14), (15) and (16) the following magnetic induction value can be obtained:

$$\vec{B}(x, y, z) = \frac{\mu_0}{4\pi} \{ (C_{11} + C_{21})\vec{i} + (C_{12} + C_{22})\vec{j} + (C_{13} + C_{23})\vec{k} \}$$

$$\vec{B}(x, y, z) = [B_x \quad B_y \quad B_z]$$

where:

$$C_{11} = \iint \frac{-M \cos \varphi \left( z - \frac{h}{2} \right) r}{\left( x^2 + y^2 + z^2 - 2r(x \cos \varphi + y \sin \varphi) - zh + r^2 + \frac{h^2}{4} \right)^{\frac{3}{2}}} d\varphi dr$$

$$C_{12} = \iint \frac{-M \sin \varphi \left( z - \frac{h}{2} \right) r}{\left( x^2 + y^2 + z^2 - 2r(x \cos \varphi + y \sin \varphi) - zh + r^2 + \frac{h^2}{4} \right)^{\frac{3}{2}}} d\varphi dr$$

$$C_{13} = \iint \frac{M(x \cos \varphi + y \sin \varphi - r)r}{\left( x^2 + y^2 + z^2 - 2r(x \cos \varphi + y \sin \varphi) - zh + r^2 + \frac{h^2}{4} \right)^{\frac{3}{2}}} d\varphi dr$$

$$C_{21} = \iint \frac{M \cos \varphi \left( z + \frac{h}{2} \right) r}{\left( x^2 + y^2 + z^2 - 2r(x \cos \varphi + y \sin \varphi) + zh + r^2 + \frac{h^2}{4} \right)^{\frac{3}{2}}} d\varphi dr$$

$$C_{22} = \iint \frac{M \sin \varphi \left( z + \frac{h}{2} \right) r}{\left( x^2 + y^2 + z^2 - 2r(x \cos \varphi + y \sin \varphi) + zh + r^2 + \frac{h^2}{4} \right)^{\frac{3}{2}}} d\varphi dr$$

$$C_{23} = \iint \frac{-M(x \cos \varphi + y \sin \varphi - r)r}{\left( x^2 + y^2 + z^2 - 2r(x \cos \varphi + y \sin \varphi) + zh + r^2 + \frac{h^2}{4} \right)^{\frac{3}{2}}} d\varphi dr$$

By solving the above given integrals and accounting for magnetic induction values in Lorentz force it is possible to determine lifting force of the bearing.

### SUMMARY

- The elaborated mathematical model makes it possible to assess magnetic force value and direction. Such model is necessary for determination of maximum magnetic force generated by radial passive magnetic bearing. Moreover the model can be applied to assessing dynamic parameters of active magnetic suspension.
- The presented approach leads to analytical solutions which make analyzing magnetic bearings by means of mathematical programs in a simple way, possible. The model has been adjusted to the Matlab-Simulink engineering software which enables analyzing dynamic processes.
- The software based on the finite elements method (FEM), commonly used for solving static magnetic fields and magnetic forces do not make it possible to perform a comprehensive dynamic analysis of radial passive magnetic bearing.
- Basing on the elaborated model these authors conduct, by means of Matlab software, design process of passive suspensions applicable to water propellers. The elaborated models and relevant design algorithms will be verified during experimental tests and analyses with the use of FEM-based programs (static analyses).
- Elaboration of comprehensive mathematical models and then determination of their allowable simplification would make it possible to build algorithms capable of facilitating implementation of passive magnetic suspensions in practice.
- Apart from the elaboration of passive models of radial magnetic bearing, it is intended to elaborate models of axial bearings. Such bearings will be applicable to a bearing system of water propeller rotor, based on another configuration of magnetic bearings.

### BIBLIOGRAPHY:

1. ISO14839-2:2004 Standard: *Mechanical vibration -Vibration of rotating machinery equipped with active magnetic bearings. Part 2: Evaluation of vibration*. Edition: 1 | Stage: 90.93 | TC 108/SC 2 ICS: 17.160
2. D. Griffiths: *Introduction to Electrodynamics*. Prince Hall, Upper Saddle River, New Jersey 07458, USA, 1999
3. Gosiewski Z., Falkowski K.: *Multifunctional magnetic bearings. Monograph*. Wydawnictwo Naukowe Instytutu Lotnictwa (Scientific Publishing House of Aviation Institute), Warsaw, 2003
4. Falkowski K.: *Modelling passive magnetic bearings* (in Polish). The Conference Automaticon 2006, Warsaw, March 2006
5. Falkowski K., Gosiewski Z.: *Analytical Method of the Magnetic Forces Estimation in Passive Magnetic Bearings*. The 8<sup>th</sup> International Conference on Motion and Vibration - Control MOVIC 2006, Korea, September 2006
6. Falkowski K.: *Passive magnetic bearing* (in Polish). The Conference Automaticon 2007, electronically edited proceedings, Warsaw, March 2007
7. Falkowski K., Gosiewski Z.: *The differential passive magnetic bearing for high-speed flexible rotor*. The 3<sup>rd</sup> International Conference on Mechatronic Systems and Materials (MSM 2007), 27 - 29 September, 2007, Kaunas, Lithuania, Published in the Solid State Phenomena Journal, Special topic volume on Mechatronic Systems and Materials II, Vol. 144, 2009.
8. Jarzyna H., Koronowicz T., Szantyr J.,A.: *Design of Marine Propellers*. Maszyny Przepływowe, vol.20, Ossolineum 1996.

### CONTACT WITH THE AUTHORS

Leszek Matuszewski, Ph. D.  
Faculty of Ocean Engineering  
and Ship Technology  
Gdansk University of Technology  
Narutowicza 11/12  
80-233 Gdansk, POLAND  
e-mail: leszekma@pg.gda.pl

Krzysztof Falkowski, Ph. D.  
Faculty of Mechatronics,  
Military University of Technology  
Gen. Sylwestra Kaliskiego 2  
00-908 Warsaw 49, POLAND  
e-mail: krzysztof.falkowski@wat.edu.pl

# Problems of welding in shipbuilding - an analytic-numerical assessment of the thermal cycle in HAZ with three dimensional heat source models in agreement with modelling rules

## Part III Non-linear analytic-numerical assessment of thermal cycle - examples

Eugeniusz Ranatowski, Prof  
 University of Technology and Life Science, Bydgoszcz

### ABSTRACT



*This part is continuation of PART II. Analytic solutions for the temperature distribution in HAZ – presented in the previous part of this article are transformed for computer calculation with used Mathcad programme. There are established algorithms in moving and stationary systems for thermal cycle calculating. Finally, a few analytical examples with use of C-I-N and D-E models are demonstrated.*

**Keywords:** welding; shipbuilding; welding in shipbuilding; thermal cycle; heat affected zone; heat source model

### ADAPTATION OF THE ANALYTICAL SOLUTIONS FOR NON-LINEAR COMPUTER CALCULATIONS

The equations (37)÷(42) of PART II of this article are algebraic form of linear heat flow solutions.

In order to execute computer calculations with temperature dependent physical parameters:  $\lambda$ ,  $c_p$ ,  $\rho$  the above algebraic expressions must be transformed. For this purpose we will use calculations in Mathcad programme [1]. This programme is very useful for modelling and simulation of welding thermal process [2, 3].

Therefore the following assumptions were done:

- heat source energy is being input to the metal during time  $\Delta t$ , not impulsively  $\Delta t \rightarrow 0$ . HS inputs are being summed up in points in distance  $\Delta x = v \Delta t$ . Considering this  $t' = (j-1)\Delta t$ , ( $j = 1, 2, 3 \dots n$ ).
- integrals were replaced by finished sums assuring sufficient exactness. Finally, the following computing expressions for linear heat flow solutions are obtained [4]:

#### A. from Cylindrical-Involution-Normal heat source model

- Stationary co-ordinates system :

$$T(x_0, y_0, z_0, t) = \sum_{j=1}^n \text{if } \{t < (j-1) \cdot \Delta t, 0, \frac{q \cdot k \cdot K_z}{\pi \cdot c_\gamma \cdot (1 - \exp(-K \cdot s))} \cdot \frac{1}{4 \cdot a \cdot k \cdot (t - (j-1))\Delta t + 1} \cdot \exp\left[\frac{-k \cdot ((x_0 - (j-1)v \cdot \Delta t)^2 + y_0^2)}{4 \cdot a \cdot k(t - (j-1)\Delta t) + 1}\right] \cdot \sum_{i=1}^{\text{last}} B_i \cdot C_i \cdot D_i \cdot \exp[-a \cdot r_i^2(t - (j-1)\Delta t)]\} \quad (1a)$$

- Moving co-ordinates system:

$$T(x, y, z, t) = \sum_{j=1}^n \text{if } \{t < (j-1) \cdot \Delta t, 0, \frac{q \cdot k \cdot K_z}{\pi \cdot c_\gamma \cdot (1 - \exp(-K \cdot s))} \cdot \frac{1}{4 \cdot a \cdot k \cdot (t - (j-1))\Delta t + 1} \cdot \exp\left[\frac{-k \cdot ((x + vt - (j-1)v \cdot \Delta t)^2 + y^2)}{4 \cdot a \cdot k(t - (j-1)\Delta t) + 1}\right] \cdot \sum_{i=1}^{\text{last}} B_i \cdot C_i \cdot D_i \cdot \exp[-a \cdot r_i^2(t - (j-1)\Delta t)]\} \quad (1b)$$



### B. from Double Ellipsoidal configuration of source

- Stationary co-ordinates system

$$T(x_0, y_0, z_0, t) = \sum_{j=1}^n \text{if } \{t < (j-1) \cdot \Delta t, 0,$$

$$\left( \frac{q \cdot f_r \cdot 3 \cdot \sqrt{3} \cdot \Delta t}{\pi \cdot \sqrt{\pi} \cdot \frac{\lambda}{a} \cdot c_f \cdot \sqrt{\left( (12 \cdot a \cdot (t - (j-1)\Delta t) + a_f^2) \cdot (12 \cdot a \cdot (t - (j-1)\Delta t) + b_f^2) \right)}} \right) \cdot \exp \left[ - \left( \frac{(x_0 - v \cdot (j-1)\Delta t)^2}{4 \cdot a \cdot (t - (j-1)\Delta t) + \frac{1}{3} \cdot a_f^2} + \frac{y_0^2}{4 \cdot a \cdot (t - (j-1)\Delta t) + \frac{1}{3} \cdot b_f^2} \right) \right] + \left( \frac{q \cdot f_r \cdot 3 \cdot \sqrt{3} \cdot \Delta t'}{\pi \cdot \sqrt{\pi} \cdot \frac{\lambda}{a} \cdot c_f \cdot \sqrt{\left( (12 \cdot a \cdot (t - (j-1)\Delta t) + a_r^2) \cdot (12 \cdot a \cdot (t - (j-1)\Delta t) + b_r^2) \right)}} \right) \cdot \exp \left[ - \left( \frac{(x_0 - v \cdot (j-1)\Delta t)^2}{4 \cdot a \cdot (t - (j-1)\Delta t) + \frac{1}{3} \cdot a_r^2} + \frac{y_0^2}{4 \cdot a \cdot (t - (j-1)\Delta t) + \frac{1}{3} \cdot b_r^2} \right) \right] \cdot \sum_{j=1}^{\text{last}} B_i \cdot C_i \cdot D_i \cdot \exp[-a \cdot r_i^2 (t - (j-1)\Delta t)] \} \quad (2a)$$

- Moving co-ordinates system

$$T(x, y, z, t) = \sum_{j=1}^n \text{if } \{t < (j-1) \cdot \Delta t, 0,$$

$$\left( \frac{q \cdot f_r \cdot 3 \cdot \sqrt{3} \cdot \Delta t}{\pi \cdot \sqrt{\pi} \cdot \frac{\lambda}{a} \cdot c_f \cdot \sqrt{\left( (12 \cdot a \cdot (t - (j-1)\Delta t) + a_f^2) \cdot (12 \cdot a \cdot (t - (j-1)\Delta t) + b_f^2) \right)}} \right) \cdot \exp \left[ - \left( \frac{(x + v(t - (j-1)\Delta t))^2}{4 \cdot a \cdot (t - (j-1)\Delta t) + \frac{1}{3} \cdot a_f^2} + \frac{y^2}{4 \cdot a \cdot (t - (j-1)\Delta t) + \frac{1}{3} \cdot b_f^2} \right) \right] + \left( \frac{q \cdot f_r \cdot 3 \cdot \sqrt{3} \cdot \Delta t'}{\pi \cdot \sqrt{\pi} \cdot \frac{\lambda}{a} \cdot c_f \cdot \sqrt{\left( (12 \cdot a \cdot (t - (j-1)\Delta t) + a_r^2) \cdot (12 \cdot a \cdot (t - (j-1)\Delta t) + b_r^2) \right)}} \right) \cdot \exp \left[ - \left( \frac{(x + v(t - (j-1)\Delta t))^2}{4 \cdot a \cdot (t - (j-1)\Delta t) + \frac{1}{3} \cdot a_r^2} + \frac{y^2}{4 \cdot a \cdot (t - (j-1)\Delta t) + \frac{1}{3} \cdot b_r^2} \right) \right] \cdot \sum_{j=1}^{\text{last}} B_i \cdot C_i \cdot D_i \cdot \exp[-a \cdot r_i^2 (t - (j-1)\Delta t)] \} \quad (2b)$$

In order to execute computer calculations with temperature dependent physical parameters:  $\lambda$ ,  $c_p$ ,  $\rho$  the above algebraic expressions must be transformed.

Therefore the following assumptions were done:

- heat source energy is being input during time  $\Delta t$ , not impulsively  $\Delta t \rightarrow 0$ . HS inputs are being summed up in points in distance  $\Delta x = v \Delta t$ . Considering this  $t' = (j-1) \Delta t$  ( $j = 1, 2, 3, \dots, S$ ),
- the integrals are changed to an algorithm executing proper summing with physical parameters upon temperature change control,
- as  $\lambda(T)$ ,  $c_p(T)$ ,  $\rho(T)$ ,  $\alpha(T)$  values in defined increments are known – like shown in table 1, the matrices containing T and corresponding  $\lambda(T)$ ,  $c_p(T)$ ,  $\rho(T)$ ,  $\alpha(T)$  values are defined.

With use of linear interpolation procedure, the continuous functions  $\lambda(T)$ ,  $c_p(T)$ ,  $\rho(T)$ ,  $\alpha(T)$  were created and built-in inside calculation sheet.

There are three main mini-procedures responsible for thermal cycle calculating. In the first of them initial values are presented (these values are specific for the given cycle). "Stab\_time" parameter is estimated time needed for stabilisation of thermal field in moving co-ordinates system, " $\Delta t$ " is duration time of every heat impulse being input. Therefore "S" gives the total number of heat impulses to be generated in order to obtain

the summary thermal field as a result (this parameter is being used finally in the third mini-procedure). The estimation of thermal fields from several impulses is running with changeable values of  $\alpha$  and  $\lambda$  parameters according to Table 1. Parameter "Last" is used in the second mini-procedure which computes  $r_1, r_2, r_3, \dots, r_n$  values – again with step by step  $\lambda(T)$  values being modified. The final mini-procedure summarises thermal fields from several heat energy impulses using a proper formula specific for several HS model.

The following algorithms (3) and (4) with initial computing parameters are usually used to perform calculations for various heat sources in moving co-ordinates system:

### A. from Cylindrical-Involution-Normal heat source model:

$$\text{Stab\_time} = 19 \text{ sec } \Delta t = 0.05 \text{ sec}$$

$$S = \text{Stab\_time} / \Delta t = 380 \text{ last} = 0$$

$$T_n(x, y, z, t) = \begin{cases} T \leftarrow 0 \\ \text{for } j \in 1 \dots S = \frac{\text{Stab\_time}}{\Delta t} \\ a \leftarrow a(T) \\ \lambda \leftarrow \lambda(T) \\ \text{for } i \in 1 \dots \text{last} \end{cases}$$

$$r_i = \left[ \begin{array}{l} n \leftarrow \text{threshold} \\ \text{root} \left[ \frac{\cot(n \cdot g) - \lambda^2 \cdot \left[ n + (i-1) \cdot \frac{\pi}{g} \right]^2 - \alpha_0 \cdot \alpha_1}{(\alpha_0 + \alpha_1) \cdot \left[ \lambda \cdot \left[ n + (i-1) \cdot \frac{\pi}{g} \right] \right]} \right] \cdot n + \\ + (i-1) \cdot \frac{\pi}{g} \\ \text{if} \left[ \text{root} \left[ \frac{\cot(n \cdot g) - \lambda^2 \cdot \left[ n + (i-1) \cdot \frac{\pi}{g} \right]^2 - a_0 \cdot a_1}{(a_0 + a_1) \cdot \left[ \lambda \cdot \left[ n + (i-1) \cdot \frac{\pi}{g} \right] \right]} \right] \cdot n \right] > \\ > \text{threshold} \\ \text{threshold} + (i-1) \cdot \frac{\pi}{g} \quad \text{otherwise} \end{array} \right]$$

$$r_i = \left[ \begin{array}{l} n \leftarrow \text{threshold} \\ \text{root} \left[ \frac{\cot(n \cdot g) - \lambda^2 \cdot \left[ n + (i-1) \cdot \frac{\pi}{g} \right]^2 - \alpha_0 \cdot \alpha_1}{(\alpha_0 + \alpha_1) \cdot \left[ \lambda \cdot \left[ n + (i-1) \cdot \frac{\pi}{g} \right] \right]} \right] \cdot n + \\ + (i-1) \cdot \frac{\pi}{g} \\ \text{if} \left[ \text{root} \left[ \frac{\cot(n \cdot g) - \lambda^2 \cdot \left[ n + (i-1) \cdot \frac{\pi}{g} \right]^2 - a_0 \cdot a_1}{(a_0 + a_1) \cdot \left[ \lambda \cdot \left[ n + (i-1) \cdot \frac{\pi}{g} \right] \right]} \right] \cdot n \right] > \\ > \text{threshold} \\ \text{threshold} + (i-1) \cdot \frac{\pi}{g} \quad \text{otherwise} \end{array} \right]$$

$$\left[ \begin{array}{l} T \leftarrow T \text{ if } t < (j-1) \cdot \Delta t, 0, q \cdot \\ \cdot k \frac{K_z \Delta t}{\pi \cdot \frac{\lambda}{a} \cdot (1 - \exp(-K_z \cdot s))} \cdot \\ \frac{1}{[1 + 4 \cdot a \cdot k(t - (j-1) \cdot \Delta t)]} \\ \cdot \exp \left[ -k \frac{[(x + v \cdot (t - (j-1) \Delta t))^2 + y^2]}{1 + 4 \alpha \cdot k(t - (j-1) \Delta t)} \right] \cdot \\ \cdot \sum_{i=1}^{\text{last}} B_i \cdot C_i \cdot D_i \exp[a \cdot r_i^2 \cdot (t - (j-1) \cdot \Delta t)] \\ T \end{array} \right] \quad (3)$$

$$\left[ \begin{array}{l} T \leftarrow T \text{ if } t < (j-1) \cdot \Delta t, 0, \\ \left( \frac{q \cdot f_f \cdot 3 \cdot \sqrt{3} \cdot \Delta t}{\pi \cdot \sqrt{\pi} \cdot \frac{\lambda}{a} \cdot c_f \cdot \sqrt{\left( (12 \cdot a \cdot (t - (j-1) \Delta t) + a_f^2) \cdot \right. \right.} \\ \left. \left. \cdot (12 \cdot a \cdot (t - (j-1) \Delta t) + b_f^2) \right)} \right) \\ \cdot \exp \left( \left( \frac{(x + v \cdot (t - (j-1) \Delta t))^2}{4 \cdot a \cdot (t - (j-1) \Delta t) + \frac{1}{3} \cdot a_f^2} + \right. \right) \\ \left. \left. + \frac{y^2}{4 \cdot a \cdot (t - (j-1) \Delta t) + \frac{1}{3} \cdot b_f^2} \right) \right) + \\ \left( \frac{q \cdot f_r \cdot 3 \cdot \sqrt{3} \cdot \Delta t}{\pi \cdot \sqrt{\pi} \cdot \frac{\lambda}{a} \cdot c_r \cdot \sqrt{\left( (12 \cdot a \cdot (t - (j-1) \Delta t) + a_r^2) \cdot \right. \right.} \\ \left. \left. \cdot (12 \cdot a \cdot (t - (j-1) \Delta t) + b_r^2) \right)} \right) \\ \cdot \exp \left( \left( \frac{(x + v \cdot (t - (j-1) \Delta t))^2}{4 \cdot a \cdot (t - (j-1) \Delta t) + \frac{1}{3} \cdot a_r^2} + \right. \right) \\ \left. \left. + \frac{y^2}{4 \cdot a \cdot (t - (j-1) \Delta t) + \frac{1}{3} \cdot b_r^2} \right) \right) \cdot \\ \cdot \sum_{i=1}^{\text{last}} B_i \cdot C_i \cdot E_i \cdot \exp[a \cdot r_i^2 \cdot (t - (j-1) \cdot \Delta t)] \end{array} \right] \quad (4)$$

**B. from D-E configuration of source:**

$$T_n(x, y, z, t) = \left[ \begin{array}{l} T \leftarrow 0 \\ \text{for } j \in 1 \dots S = \frac{\text{Stab\_time}}{\Delta t} \\ a \leftarrow a(T) \\ \lambda \leftarrow \lambda(T) \\ \text{for } i \in 1 \dots \text{last} \end{array} \right]$$

For stationary system ( $x_0 = x + vt$ ,  $y_0 = y$ ,  $z_0 = z$ ) the following algorithms (5) and (6) are presented:

**C. from Cylindrical-Involution-Normal heat source model:**

Stab\_time = 19 sec  
 $\Delta t = 0.05$  sec  
 $S = \text{Stab\_time} / \Delta t = 380$  last = 0

$$T_n(x, y, z, t) = \begin{cases} T \leftarrow 0 \\ \text{for } j \in 1 \dots S = \frac{\text{Stab\_time}}{\Delta t} \\ a \leftarrow a(T) \\ \lambda \leftarrow \lambda(T) \\ \text{for } i \in 1 \dots \text{last} \\ n \leftarrow \text{threshold} \\ \text{root} \left[ \frac{\cot(n \cdot g) - \lambda^2 \cdot \left[ n + (i-1) \cdot \frac{\pi}{g} \right]^2 - \alpha_0 \cdot \alpha_1}{(\alpha_0 + \alpha_1) \cdot \left[ \lambda \cdot \left[ n + (i-1) \cdot \frac{\pi}{g} \right] \right]} \right] \cdot n + \\ + (i-1) \cdot \frac{\pi}{g} \\ \text{if} \left[ \text{root} \left[ \frac{\cot(n \cdot g) - \lambda^2 \cdot \left[ n + (i-1) \cdot \frac{\pi}{g} \right]^2 - a_0 \cdot a_1}{(a_0 + a_1) \cdot \left[ \lambda \cdot \left[ n + (i-1) \cdot \frac{\pi}{g} \right] \right]} \right] \cdot n \right] > \\ > \text{threshold} \\ \text{threshold} + (i-1) \cdot \frac{\pi}{g} \text{ otherwise} \\ T \leftarrow T \text{ if } \\ t < (j-1) \cdot \Delta t, 0, q \cdot \\ \cdot k \frac{K_z \Delta t}{\pi \cdot \frac{\lambda}{a} \cdot (1 - \exp(-K_z \cdot s))} \cdot \\ \cdot \frac{1}{[1 + 4 \cdot a \cdot k(t - (j-1) \cdot \Delta t)]} \\ \cdot \exp \left[ -k \frac{[(x + v \cdot (t - (j-1) \Delta t))^2 + y^2]}{1 + 4 \alpha \cdot k(t - (j-1) \Delta t)} \right] \cdot \\ \cdot \sum_{i=1}^{\text{last}} B_i \cdot C_i \cdot D_i \cdot \\ \cdot \exp[a \cdot r_i^2 \cdot (t - (j-1) \cdot \Delta t)] \\ T \end{cases}$$

**D. from D-E configuration of source:**

$$T_n(x, y, z, t) = \begin{cases} T \leftarrow 0 \\ \text{for } j \in 1 \dots S = \frac{\text{Stab\_time}}{\Delta t} \\ a \leftarrow a(T) \\ \lambda \leftarrow \lambda(T) \\ \text{for } i \in 1 \dots \text{last} \end{cases}$$

$$r_i = \begin{cases} n \leftarrow \text{threshold} \\ \text{root} \left[ \frac{\cot(n \cdot g) - \lambda^2 \cdot \left[ n + (i-1) \cdot \frac{\pi}{g} \right]^2 - \alpha_0 \cdot \alpha_1}{(\alpha_0 + \alpha_1) \cdot \left[ \lambda \cdot \left[ n + (i-1) \cdot \frac{\pi}{g} \right] \right]} \right] \cdot n + \\ + (i-1) \cdot \frac{\pi}{g} \\ \text{if} \left[ \text{root} \left[ \frac{\cot(n \cdot g) - \lambda^2 \cdot \left[ n + (i-1) \cdot \frac{\pi}{g} \right]^2 - a_0 \cdot a_1}{(a_0 + a_1) \cdot \left[ \lambda \cdot \left[ n + (i-1) \cdot \frac{\pi}{g} \right] \right]} \right] \cdot n \right] > \\ > \text{threshold} \\ \text{threshold} + (i-1) \cdot \frac{\pi}{g} \text{ otherwise} \end{cases}$$

$$(5) \quad \begin{cases} T \leftarrow T \text{ if } t < (j-1) \cdot \Delta t, 0, \\ \left( \frac{q \cdot f_f \cdot 3 \cdot \sqrt{3} \cdot \Delta t}{\pi \cdot \sqrt{\pi} \cdot \frac{\lambda}{a} \cdot c_f \cdot \sqrt{\left( (12 \cdot a \cdot (t - (j-1) \Delta t) + a_f^2) \cdot \right. \right.} \right. \\ \left. \left. \cdot (12 \cdot a \cdot (t - (j-1) \Delta t) + b_f^2) \right)} \right) \cdot \exp \left[ - \left( \frac{\left( \frac{(x_0 - v \cdot (j-1) \Delta t)^2}{4 \cdot a \cdot (t - (j-1) \Delta t) + \frac{1}{3} \cdot a_f^2} + \right. \right. \right. \\ \left. \left. \left. + \frac{y_0^2}{4 \cdot a \cdot (t - (j-1) \Delta t) + \frac{1}{3} \cdot b_f^2} \right)} \right) \right] + \\ + \frac{q \cdot f_r \cdot 3 \cdot \sqrt{3} \cdot \Delta t}{\pi \cdot \sqrt{\pi} \cdot \frac{\lambda}{a} \cdot c_r \cdot \sqrt{\left( (12 \cdot a \cdot (t - (j-1) \Delta t) + a_r^2) \cdot \right. \right.} \\ \left. \left. \cdot (12 \cdot a \cdot (t - (j-1) \Delta t) + b_r^2) \right)} \right) \cdot \exp \left[ - \left( \frac{\left( \frac{(x_0 - v \cdot (j-1) \Delta t)^2}{4 \cdot a \cdot (t - (j-1) \Delta t) + \frac{1}{3} \cdot a_r^2} + \right. \right. \right. \\ \left. \left. \left. + \frac{y_0^2}{4 \cdot a \cdot (t - (j-1) \Delta t) + \frac{1}{3} \cdot b_r^2} \right)} \right) \right] \cdot \\ \cdot \sum_{i=1}^{\text{last}} B_i \cdot C_i \cdot E_i \exp[a \cdot r_i^2 \cdot (t - (j-1) \cdot \Delta t)] \end{cases}$$

The base procedure defined by algorithms (3) ÷ (5) requires cooperation with several sub-procedures such as *Stab\_time*, *last*, calculation of roots  $r_i$ ,  $\lambda(T)$ ,  $\alpha(T)$ .

From essential point of view the sub-procedure *Stab\_time* defines in time dimension the moment of time after which it estimated its value needed for stabilisation of thermal fields as follows:

- sub-procedure *Stab\_time*

$$\begin{aligned}
 & \text{Stab\_time}(x, y, z) = \\
 & \left[ \begin{array}{l} \text{absolute} \leftarrow 20 \\ \text{settled} \leftarrow 10 \\ \text{stroke} \leftarrow 1 \\ \text{while } \frac{T\_MOVE(x, y, z, \text{absolute})}{T\_MOVE(x, y, z, \text{settled})} < 1.02 \\ \text{if} \\ \text{settled} \leftarrow \text{settled} - \text{stroke} \\ \text{while } \frac{T\_MOVE(x, y, z, \text{absolute})}{T\_MOVE(x, y, z, \text{settled})} > 1.02 \\ \text{otherwise} \\ \text{settled} \leftarrow \text{settled} + \text{stroke} \end{array} \right] \\
 & = \left[ \frac{\text{settled} + \text{stroke}}{\frac{T\_MOVE(x, y, z, \text{absolute})}{T\_MOVE(x, y, z, \text{settled} + \text{stroke})}} \right] \\
 & \left[ \frac{T\_MOVE(x, y, z, \text{absolute})}{T\_MOVE(x, y, z, \text{absolute})} \right]
 \end{aligned} \quad (7)$$

*Stab\_time* is compound sub-procedure realising calculation of wanted value of stabilised time for optional point in moving coordinates system. Parameters “absolute” and “settled” are preliminary set up values of start and end of partition of time, in which follows search of time stabilisation with “stroke” step.

The procedure is built in this way that last value of *Stab\_time* does not depend on value “absolute” and “settled” but correct assumption of these values shorten time wanted for account of *Stab\_time*.

Furthermore in the first main mini-procedure also cooperation is required with sub-procedures for inside calculation of  $\lambda(T)$ ,  $\alpha(T)$ . The discrete values of  $\lambda(T)$ ,  $\alpha(T)$  are known and shown in Table 1 the matrices containing T and corresponding  $\lambda(T)$ ,  $\alpha(T)$  values are defined experimentally. Than with use of linear interpolation procedure, continuous functions were created and built in inside calculation sheet as follows:

- sub-procedure  $\lambda(T)$

<1>	<2>
0	0.6285
100	0.5866
200	0.5447
300	0.5028
400	0.4609
500	0.419
600	0.3771
700	0.3487
800	0.3268
900	0.3226
1000	0.3268
1100	0.331
1200	0.3352
1300	0.3352
1400	0.3352
1500	0.3352

$$\begin{aligned}
 & \lambda(T) := \\
 & \left[ \begin{array}{l} i \leftarrow \text{floor}\left(\frac{T}{100}\right) \\ i \leftarrow 14 \text{ if } T \geq 1500 \\ \left[ \frac{(A_{i+2,2} - A_{i+1,2})}{(A_{i+2,1} - A_{i+1,1})} \cdot (t - A_{i+1,1}) + A_{i+1,2} \right] \\ T := 1 \dots 1500 \end{array} \right] \quad (8)
 \end{aligned}$$

- sub-procedure  $\alpha(T)$

<1>	<2>
0	0.19
100	0.16
200	0.13
300	0.11
400	0.093
500	0.079
600	0.062
700	0.05
768	0.034
800	0.042
900	0.055
901	0.062
1200	0.062
1300	0.062
1400	0.062
1500	0.062

$$\begin{aligned}
 & \alpha(T) := \\
 & \left[ \begin{array}{l} i \leftarrow \text{floor}\left(\frac{T}{100}\right) \\ \text{if } T < 768 \\ i \leftarrow 8 \text{ if } T \geq 768 \\ i \leftarrow 9 \text{ if } T \geq 800 \\ i \leftarrow 10 \text{ if } T \geq 900 \\ i \leftarrow 11 \text{ if } T \geq 901 \\ i \leftarrow 12 \text{ if } T \geq 1200 \\ \left[ \frac{(C_{i+2,2} - C_{i+1,2})}{(C_{i+2,1} - C_{i+1,1})} \cdot (t - C_{i+1,1}) + C_{i+1,2} \right] \\ T := 0 \dots 1500 \end{array} \right] \quad (9)
 \end{aligned}$$

On Fig. 1 are presented discrete values of  $\lambda(T)$ ,  $\alpha(T)$  and determined by continuous functions with used sub-procedures (8) and (9) for a.  $\lambda(T)$ , b.  $\alpha(T)$ .

We have high conformity of continuous functions and discrete value of  $\lambda(T)$ ,  $\alpha(T)$  from above-mentioned date on Fig. 1.

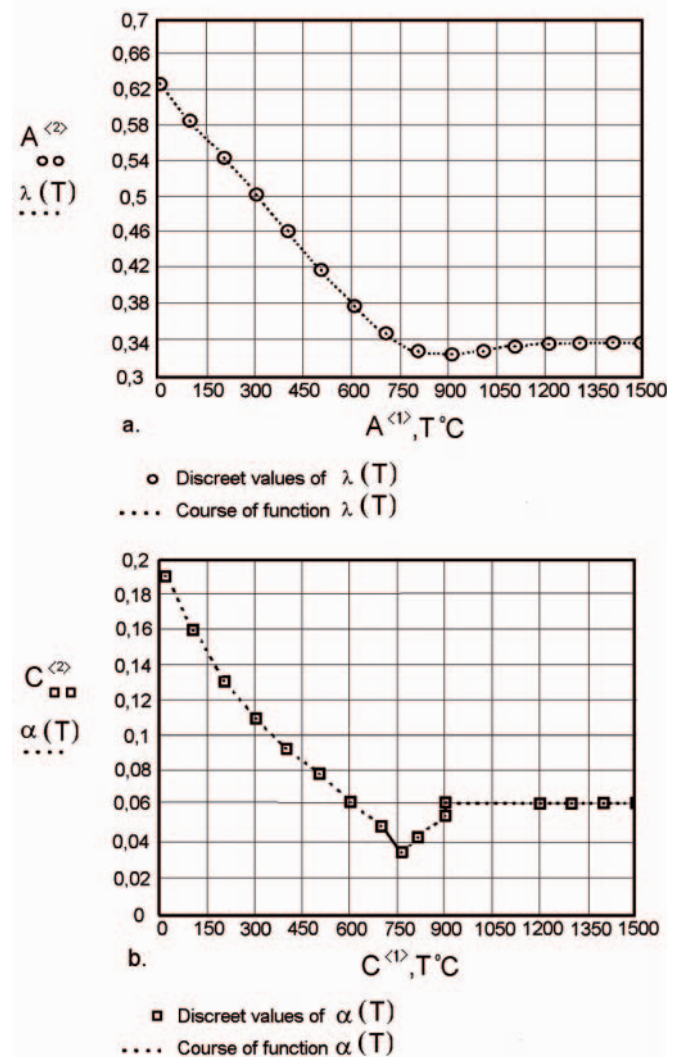


Fig. 1. Values of a.  $\lambda(T)$  and b.  $\alpha(T)$  in agreement with tab. 1 and continuous functions of for low carbon steel 0.1% C



The sub-procedure “LAST” realises calculation of value of parameter “last” defining correctness of calculation in analytical meaning but it decides indirectly about amount of  $r_i$  roots which is taken into consideration in each computational step. It is possible to assure required accuracy of calculation when value of “last” is sufficiently large.

Sub-procedure “LAST” can find this value through analysis of moment of numeric convergence of neuralgic mathematical module in most adverse conditions at  $t = 0$  and  $z = 0$  as below:

- sub-procedure “LAST”

$$\text{Last} = \begin{cases} i \rightarrow 1 \\ \text{while} \left[ \left( \frac{\text{Total}_{i+1}}{\text{Total}_i} > 1.001 \right) + \right. \\ \left. + (\text{Total}_i < 0.96 \cdot \max(W)) \right] \\ i \rightarrow i + 1 \\ \left[ \begin{array}{l} i \text{ if } i > 15 \\ 15 \text{ otherwise} \end{array} \right. \end{cases} \quad (10)$$

$$\text{Pulse}_i = \left[ \frac{k K_z}{(1 - \exp(-K \cdot s)) \cdot \frac{\lambda}{\alpha}} \right] \cos(r_i \cdot z_0) + \frac{\alpha_0}{\lambda \cdot r_i} \cdot \sin(r_i \cdot z_0) \cdot B_i C_i D_i \quad (11)$$

$$\text{Total}_i = \sum_{i=1}^i \text{Pulse}_i \quad (12)$$

Realisation of sub-procedure “LAST” relies on search of sufficiently large value “i”. In order to set up condition of assumption converge of monotones growing series (from foundation for value 0.001) at necessity outreaching of 9% of maximum value “Total” in treated interval “i”. It catches on that

minimal value of “i” and can’t be smaller than 15. On Fig. 2 it is presented course of value “Pulse” and “Total”.

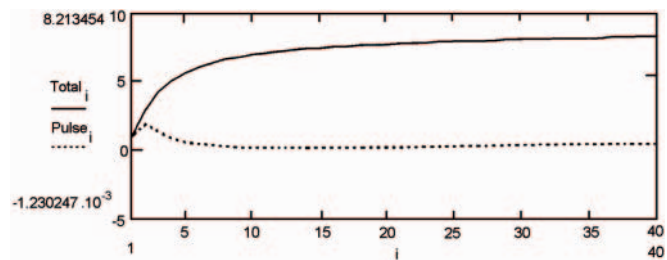


Fig. 2. Course of value “Pulse” and “Total” as function of growing value “i”

Furthermore let’s notice that computational cycle is started with acceptance of value  $\lambda(T = 0)$ ,  $\alpha(T = 0)$  but each next time step “ $\Delta t$ ” change the values of  $\lambda(T)$ ,  $\alpha(T)$  in agreement with current value of temperature  $T$ . Generation of value “ $r_i$ ” is next computational step and for each time step, which is found in numeric way according to separate “sub-procedure  $r_i$ ” which is directly insert in algorithms (3)÷(4) and simultaneously checks accuracy of calculation with used “threshold” parameter. The value of “threshold” parameter is established on very close zero but unzero.

For example in Tab. 2 some values are presented of roots  $r_i$  along with estimates of their accuracy for  $t = 0$  and  $g = 1.2$  cm, threshold = 0.0000001,  $\alpha_0 = 0.02$  W m<sup>-2</sup>K<sup>-1</sup>,  $\alpha_1 = 0.01$ .

The final sub-procedure “Temperature – T” in algorithms (3) ÷ (4) summarises thermal fields from several heat energy impulses using a proper formula specific for appropriated H-S model.

## EXAMPLES

A few examples of welding cycles in stationary co-ordinates system are shown. C-I-N and D-E configuration of source are used for analysis. The results from C-I-N and D-E models are compared with Rosenthal-Rykalin solution along with experimental results<sup>5</sup>. Material parameters are accordance with Tab. 1 for low carbon steel.

Tab. 1.  $\lambda(T)$ ,  $c_p(T)$ ,  $\rho(T)$ , and  $\alpha(T)$  values in several temperatures for low carbon steel – 0.1%C

T °C	$\lambda(T)$ Wcm <sup>-1</sup> K <sup>-1</sup>	T °C	$\rho(T) \cdot c_p(T)$ JK <sup>-1</sup> c <sup>m-3</sup>	T °C	$\alpha(T)$ cm <sup>2</sup> s <sup>-1</sup>
0	0.6285	0	3.307	0	0.190
100	0.5866	100	3.666	100	0.160
200	0.5447	200	4.190	200	0.130
300	0.5028	300	4.570	300	0.110
400	0.4609	400	4.950	400	0.093
500	0.4190	500	5.303	500	0.079
600	0.3771	600	6.082	600	0.062
700	0.3477	700	6.955	700	0.050
800	0.3268	768	9.809	768	0.034
900	0.3226	800	6.536	800	0.042
1000	0.3268	900	5.866	900	0.055
1100	0.3310	901	5.204	901	0.062
1200	0.3352	1200	5.406	1200	0.062
1300	0.3352	1300	5.406	1300	0.062
1400	0.3352	1400	5.406	1400	0.062
1500	0.3352	1500	5.406	1500	0.062

Tab. 2. The assessment of a few  $r_i$  roots (11 of 60) for non-linear approach calculation at  $t = 0$

i	$r_i$ values	$r_i$ check
1	0.198811490	$5.153050313 \cdot 10^{-9}$
2	2.633099949	$3.597482134 \cdot 10^{-8}$
3	5.243573590	$6.028955113 \cdot 10^{-10}$
4	7.859042948	$6.232056649 \cdot 10^{-9}$
5	10.475772574	$5.70471002 \cdot 10^{-7}$
6	13.093007438	$5.118749868 \cdot 10^{-9}$
7	15.710495155	$3.640161481 \cdot 10^{-6}$
8	18.332817429	$2.0121055824 \cdot 10^{-7}$
9	20.945850074	$1.066098321 \cdot 10^{-8}$
10	23.563632979	$4.666276254 \cdot 10^{-10}$
11	26.1814807	$3.501158403 \cdot 10^{-6}$

Tab. 3. Results of estimate temperature

No of example	Temperature [°C]											
	1. experiment			2. C-I-N calcul.			3. D-E calcul.			4. R-R calcul.		
	$T_{max}$	$T_{10s}$	$T_{20s}$	$T_{max}$	$T_{10s}$	$T_{20s}$	$T_{max}$	$T_{10s}$	$T_{20s}$	$T_{max}$	$T_{10s}$	$T_{20s}$
1	1300	740	520	1410	660	420	1410	630	410	1610	360	250
2	1030	500	380	1110	470	330	1250	440	310	1560	380	265
3	1430	770	500	1470	730	470	1570	610	380	1820	470	340

**Example 1.**

Main parameters:  $q = 2400W$ ;  $g = 0.4$  cm;  $v = 0.75$  cm  $s^{-1}$   
 C-I-N:  $s = 0.2$  cm;  $Kz = 15$  cm $^{-1}$ ;  $k = 12$  cm $^{-2}$   
 D-E:  $f_f = 0.$ ;  $a_f = 0.5$  cm;  $b_f = 0.5$  cm;  $c_f = 3.0$  cm;  
 $f_r = 1.4$ ;  $a_r = 1.0$  cm;  $b_r = 0.5$  cm;  $c_r = 3.0$  cm – Fig. 3.

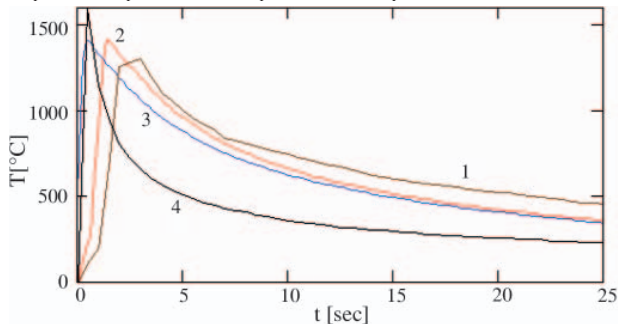


Fig. 3. Temperature change in points:  $x_0 = 0, y_0 = 0.1, z_0 = 0$   
 Symbols: 1 – experimental, 2 – C-I-N calculation, 3 – D-E calculation  
 4 – Rykalin-Rosenthal solution (plate model with the sector line source)

**Example 2.**

Main parameters:  $q = 3300$  W;  $g = 0.8$  cm;  $v = 0.5$  cm  $s^{-1}$   
 C-I-N:  $s = 0.$  cm;  $Kz = 5$  cm $^{-1}$ ;  $k = 12$  cm $^{-2}$   
 D-E:  $f_f = 0.$ ;  $a_f = 0.$  cm;  $b_f = 0.$  cm;  $c_f = 4.2$  cm;  
 $f_r = 1.4$ ;  $a_r = 1.2$  cm;  $b_r = 0.$  cm;  $c_r = 4.2$  cm – Fig. 4.

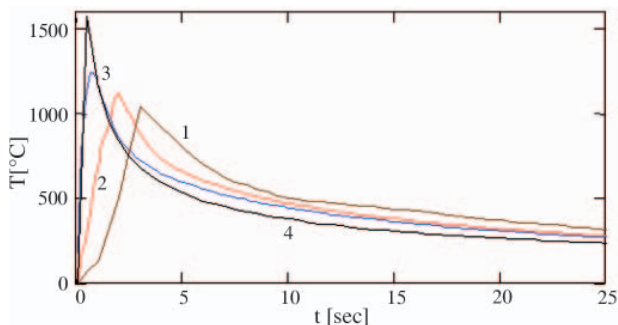


Fig. 4. Temperature change in points:  $x_0 = 0, y_0 = 0.1, z_0 = 0$   
 Symbols: 1 – experimental, 2 – C-I-N calculation, 3 – D-E calculation  
 4 – Rykalin-Rosenthal solution (plate model with the sector line source)

**Example 3.**

Main parameters:  $q = 12000W$ ;  $g = 0.8$ cm;  $v = 1.1$  cm  $s^{-1}$   
 C-I-N:  $s = 0.$  cm;  $Kz = 2$  cm $^{-1}$ ;  $k = 8$  cm $^{-2}$   
 D-E:  $f_f = 0.$ ;  $a_f = 0.$  cm;  $b_f = 0.7$  cm;  $c_f = .2$  cm;  
 $f_r = 1.4$ ;  $a_r = 1.4$  cm;  $b_r = 0.7$  cm;  $c_r = .2$  cm – Fig. 5.

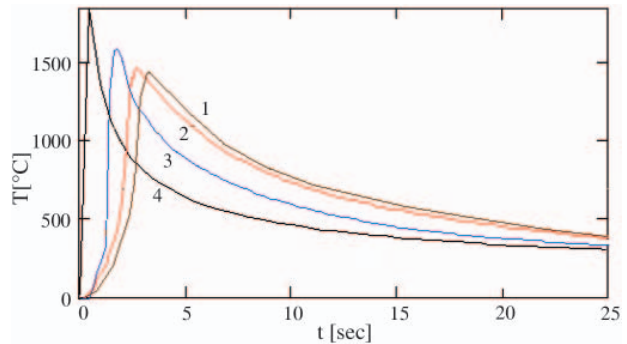


Fig. 5. Temperature change in points:  $x_0 = 0, y_0 = 0.1, z_0 = 0$   
 Symbols: 1 – experimental, 2 – C-I-N calculation, 3 – D-E calculation  
 4 – Rykalin-Rosenthal solution (plate model with the sector line source)

For the comparison of account and experiment results, in Table 3, effects of estimated temperatures for examples 1 ÷ 3 are collected.

Temperature is defined for:

- $T_{max}$  – maximum temperature,
- $T_{10s}$  – temperature after 10 s,
- $T_{20s}$  – temperature after 20 s.

In the first example we can see distinctly correspondence of assessed temperature and experiment when we used analytic-numerical method and equations (1a), (2a) with use C-I-N and D-E heat source models respectively. For above example it take a stand of difference of order 100 - 300°C for maximum temperature. Results got run away from these issues is analytical assessment of run of temperature by used of Rosenthal-Rykalin (R-R) solutions.

In the second example it takes a stand a similar situation but with certain difference in upper temperature. Highest

conformity with experiment in this range of temperature is for analytic-numerical solution and agreement with equation (1a) for C-I-N heat source model. Results of estimates temperature with used pure analytical R-R solutions definitely run away from analytic-numerical solution especially in upper temperatures where divergence in estimated  $T_{max}$  amount to 500°C. Results of third example are similar to second example in essential meaning.

The special feature of characteristic of above examples 1 ÷ 3 depends on heat source power and line energy of welding (1 – 3200 J cm<sup>-1</sup>, 2 – 00 J cm<sup>-1</sup> and 3 – 10909 J cm<sup>-1</sup>).

Furthermore these issues indicate on utility of analytic-numerical solution with adopted C-I-N heat source model rather for simulation of welding process of high concentrated energy used but may also be used for the simulation of arc welding process similarly as D-E heat source model. It confirms also laser welding process simulation [7].

## CONCLUSIONS

In this work some extended consideration about analytic-numerical methods conforming has taken place.

It is obvious that:

- with an application of various heat source models one can obtain very effective temperature field solutions,
- with appropriate algorithms, calculations are very attractive, effective and can be quickly executed on PC computers,
- further impact should of course be put on still more detailed welding phenomenon analysis. The specificity of metal phase change and other complicated phenomena should be discovered and reflected in complex model in order to make more accurate and detailed analysis possible.

The results of proposed methods were compared with experimental data and Rosenthal-Rykalin solution. The accuracy of D-E and C-I-N results having in mind experimental data was discussed and there's no doubt that the accuracy of old solutions (R-R) seems to be out of date for these examples.

All this makes analytical solutions very competitive with numerical ones and makes them very useful in engineering practice.

## REFERENCES

1. *Mathcad-User's Guide*. MathSoft, inc. 2001. Cambridge, MA02142. USA
2. B. Buchmayr: *Materials and engineering with Mathcad. Modelling and simulation in applications*. Springer-Verlag Berlin Heidelberg. 2002
3. H. Benker: *Mathematica with MathCAD*. Springer-Verlag Berlin Heidelberg. 1999
4. E. Ranatowski, A. Poćwiardowski: *Mathematical Modelling of Weld Phenomena 5*. (ed. H. Cejrak), pp. 725-742. 2000. IOM Communications
5. A. Marmołowski: *The optimal method of define of the welding temperature field in systems formulate*. PhD thesis. Technical University of Gdańsk. 2001
- A. Poćwiardowski: *The thermal identification of weld process with used analytical-numerical methods*. PhD thesis. Technical University of Bydgoszcz. 2002
7. E. Ranatowski: *Review of welding* No 8-10, pp. 152-155. 2002.

## NOMENCLATURE

- |                     |   |
|---------------------|---|
| “absolute”, s,      | - preliminary assumption of upper value of time stabilised          |
| “settled”, s,       | - preliminary assumption of lower value of time stabilised          |
| “stroke”, s,        | - a step assumption on way of installation of time of stabilisation |
| T_MOVE (x, y, z, t) | - a temperature field in moving coordinate system, °C.              |

---

## CONTACT WITH THE AUTHOR

Prof. Ranatowski Eugeniusz  
 Faculty of Mechanical Engineerig,  
 University of Technology and Life Science,  
 Prof. S. Kaliskiego 7  
 85-73 Bydgoszcz, POLAND  
 e-mail: ranatow@utp.edu.pl

# Analysis of fracture toughness of structural timber

## Part I Theory and experimental tests

Lesław Kyziół, Ph.D.  
Polish Naval Academy in Gdynia

### ABSTRACT

*This paper presents fundamentals of fracture mechanics of anisotropic materials. Fracture toughness of anisotropic materials, e.g. structural timber, depends a. o. on state of stress, environment, temperature and changes due to ageing, therefore in such materials cracking process runs in various ways. Timber is characterized by eighteen coefficients which determine its fracture toughness in contrast to metals for which this number is as low as three. In this part of considerations a way of conducting the tests of specimens subjected to cracking as well results of the tests of natural and modified timber, are presented.*

**Keywords:** anisotropic material; anisotropic material cracking; CAD specimens; test stand; complex loading; stress distribution

### INTRODUCTION

In the majority of structures operating under load the sudden cracking of elements occur in spite of that stresses in them do not exceed their allowable level. Such cracks can be caused both by material defects resulting from improper technological processes, and by external random overloading.

This work is aimed at the determination of relations between fracture toughness of natural and modified wood and size of defects, in given loading conditions. Results of the tests should reveal an effect of modification of wood on its fracture toughness.

In order to be able to determine structural material fracture toughness it is necessary to determine experimentally material constants, mainly the stress intensity factor and critical crack length. It was consisted in determining quantitative relations between resistance against the cracking in given loading conditions and size of defect. Fundamentals of fracture theory of orthotropic materials are presented. Ways are discussed of determining the critical load and possibilities in determining the structural timber fracture toughness in selected anatomic directions.

The tests were conducted for the two crack propagation modes where stratification develops along fibres in crack containing specimen: tangential-longitudinal (TL), radial-longitudinal (RL). Specimens were subjected to load leading to crack (gap) opening (disruption).

### BASIC RELATIONS WHICH DESCRIBE CRACKING PROCESS OF ISOTROPIC MATERIALS

Fracture mechanics is applied to assessing material resistance against loss of its coherence. As results from many literature sources concerning fracture of isotropic materials, crack-containing material can be loaded in three ways which may lead to crack opening (rupture), longitudinal shearing (slipping) or lateral shearing [5, 6]. The specified modes are called pure modes of loading the crack (gap) - containing element, marked I, II and III, respectively, (Fig. 1), [5, 6].

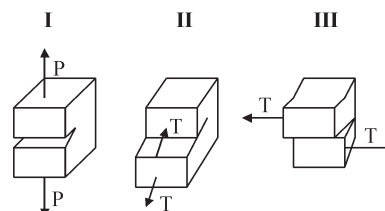


**Fig. 1.** Basic modes of cracking depending on a mode of loading applied to a body: **I)** Rupture (crack opening, pulling apart); **II)** Longitudinal shearing (slipping); **III)** Lateral shearing

Apart from the specified loading modes a few cases of complex loading which are combinations of the above mentioned cracking modes, can be met in reality.



For description of fracture toughness of specimens made of a given material the following parameters are used: critical value of the energy release coefficient  $G_{ac}$ , stress intensity factor  $K_{ac}$ , and integral  $J_c$ . The parameter  $G_{ac}$  is determined as the derivative of the potential energy released during cracking process,  $U$ , taken with respect to the crack length  $a$  [2]:

$$G_{\alpha} = -\frac{\partial U}{\partial a}, \quad \alpha = I, II, III \quad (1)$$

The energy release coefficient corresponding to the loading modes I, II, III are marked  $G_I, G_{II}, G_{III}$ , respectively. As assumed, if material fracture toughness is only slightly dependent on crack length rate then in order the gap to be capable of developing in an uncontrollable way, the following condition is to be satisfied:

$$G_{\alpha} \geq G_{ac} \quad (2)$$

The condition (2) is assumed to be the crack propagation criterion, and the parameter  $G_{\alpha}$  which characterizes material fracture toughness, is determined experimentally [6]. The critical values of the energy release coefficients  $G_{Ic}, G_{IIc}, G_{IIIc}$  characterize material fracture toughness. The stress intensity factor  $K_{\alpha}$  is used as a measure of stress and displacement field in the vicinity of gap vertex. Its value depends on value of the external loading  $\sigma_{zw}$ , crack length  $a$  as well as factor  $Y$  (a constant dependent on a crack opening mode and specimen geometry, [1, 3, 5]).

$$K_{\alpha} = K_{\alpha}(\sigma_{zw}, a, Y) \quad \alpha = I, II, III \quad (3)$$

In the subject-matter literature the stress intensity factor corresponding to the pure loading modes is marked  $K_I, K_{II}, K_{III}$ , respectively [2, 3]. To initiate cracking process, its value, like that of the stress intensity factor, should exceed the critical value  $K_{ac}$  for a given material, in compliance with the following inequality [3, 5]:

$$K_{\alpha} \geq K_{ac} \quad (4)$$

The relation (4), in contrast to the relation (2), concerns only the area around gap vertex.

Between the energy release coefficient  $G_{\alpha}$  and stress intensity factor  $K_{\alpha}$  the following relation occurs [3, 5]:

$$G_{\alpha} = c_{\alpha} K_{\alpha}^2 \quad (5)$$

where:

$c_{\alpha}$  - coefficient depending on state of stress, loading mode and mechanical properties of a given material.

The third parameter which determines resistance of materials to loss of coherence, is the so-called integral  $J_c$ . The integral  $J_c$ , like the preceding parameters, is a measure of energy necessary to trigger crack developing. In contrast to the parameters  $G_{ac}$  and  $K_{ac}$ , the parameter in question accounts for a significant plastic deformation occurring in structural materials [1, 3, 5].

## BASIC RELATIONS WHICH DESCRIBE CRACKING PROCESS OF ANISOTROPIC MATERIALS

Structural timber, an orthotropic material, is characterized by that it is subjected to cracking in various ways, depending on stress state, environment, temperature and ageing changes. The material is stratified and undergoes delamination under load. The delamination of such composite material results from many factors such as: assembling errors, mechanical failures, stress concentration in vicinity of defects and cracks as well as changes in material structure during drying.

Timber is a non-homogenous, anisotropic (multi-directional) material, that makes describing its strength properties difficult.

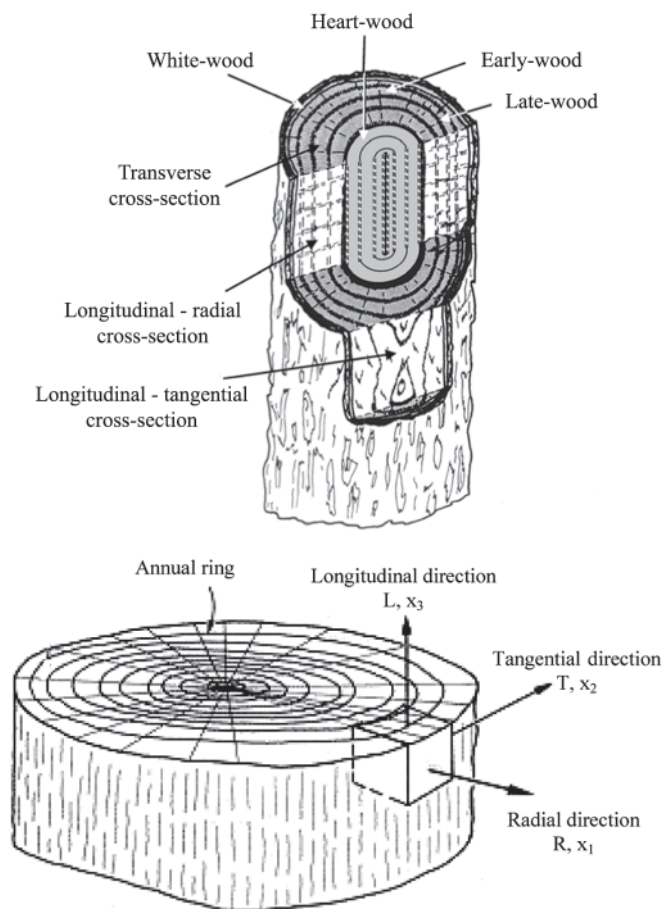


Fig. 2. A stump of wood with marked anatomic directions

As arrangement of rings in a given volume is differentiated, three principal directions (three planes of symmetry) are specified in wood: radial -  $R$  ( $x_1$ ), tangential -  $T$  ( $x_2$ ) and longitudinal one -  $L$  ( $x_3$ ), Fig. 2. If a wood specimen is cut sufficiently far from the centre of wood stump, so as to be able to consider curvature of rings negligible, then its properties can be deemed orthotropic. Wood considered as an orthotropic material has three characteristic directions strictly associated with its anatomic structure [4].

For orthotropic materials six basic modes of crack propagation are distinguished (Fig. 3). The first letter of the symbols stands for the direction normal to plane of crack, the second - direction of its propagation. Hence the tangential - longitudinal mode of propagation TL, tangential-longitudinal TR, radial-tangential RT, radial-longitudinal RL, longitudinal-tangential LT and longitudinal-radial LR, are distinguished [4].

For three modes of loading eighteen possible modes of crack propagation are assumed. Two modes are distinguished where delamination develops along fibres: tangential - longitudinal - TL and radial-longitudinal - RL, as well as four ones in lateral direction. In practice, structures are subjected to complex loads, e.g. I/II or II/III.

For assessment of fracture toughness of orthotropic materials linear fracture mechanics is used as any standard method is still lacking. In fracture toughness testing, critical values of the coefficients  $G_{Ic}, G_{IIc}, G_{IIIc}$  and factors  $K_{Ic}, K_{IIc}, K_{IIIc}$  have to be determined for every propagation mode. Wood is characterized by eighteen coefficients which determine its

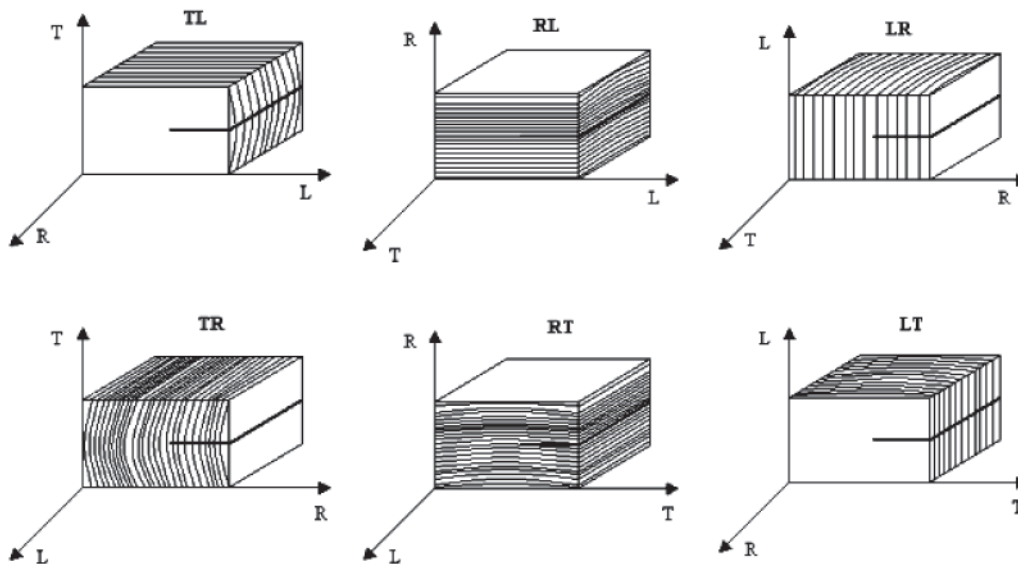


Fig. 3. Crack propagation modes in orthotropic material

fracture toughness in contrast to metals for which the number is reduced to three.

An important problem of fracture toughness of materials is determination of the critical load  $P_c$ . The critical load is defined as such value of force under which loss of specimen material coherence occurs. Its determination is complex. For determining  $P_c$  value a few methods are used out of which the following can be distinguished [6, 7, 8]:

- the method NL in which it is assumed that initiation of cracking process is commenced in the instant when a non-linearity of the  $P-\delta$  (force- gap opening) diagram appears (Fig. 4);

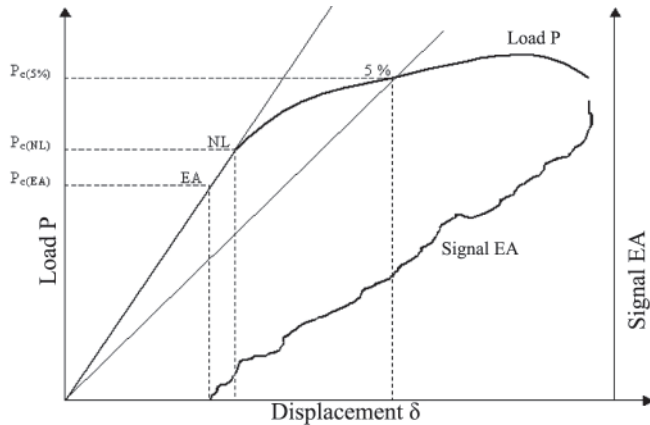


Fig. 4. Methods for determining the critical load  $P_c$

- the method  $P(\delta)$  in which the point of intersection of the diagram  $P(\delta)$  and the straight line whose slope angle tangent is smaller by 5% than that of the straight line which contains the linear part of the diagram  $P(\delta)$ , is assumed the beginning of cracking process (Fig. 4);
- the method based on non-linear and linear approximation of the diagram  $P(\delta)$ , (Fig. 5)
- the method based on acoustic emission (EA) [6].

## TESTS ON STRUCTURAL TIMBER CRACKING

### Geometry of specimens

Tests of fracture toughness of composite materials can be performed with the use of specimens of different geometrical

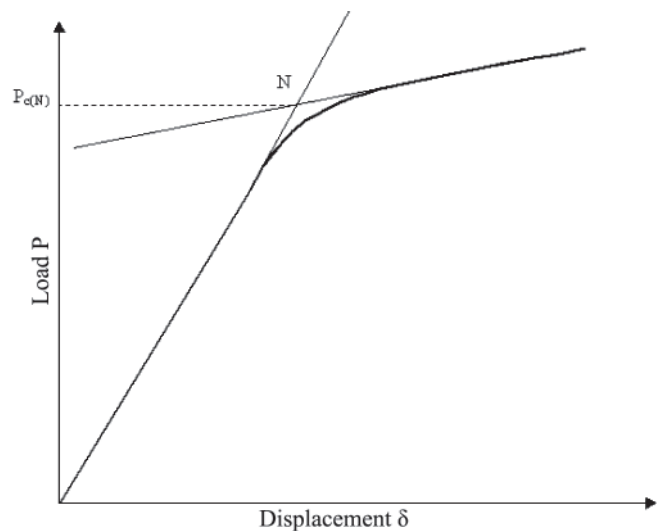


Fig. 5. Method for determining the critical load  $P_c$  based on approximation of the diagram  $P(\delta)$

forms (Fig. 6) [6]. In structural timber testing the double cantilever beam specimens (DCB) were used.

The critical energy release coefficient  $G_{1c}$  [2] for a given specimen is described by the relation:

$$G_{1c} = \frac{1}{2} \cdot \frac{P_c^2}{B} \cdot \frac{\partial C}{\partial a} \quad (6)$$

where:

- $P_c$  – critical load
- $C$  – specimen flexibility
- $B$  – thickness (breadth)
- $a$  – crack (gap) length.

The critical energy release coefficient  $G_{1c}$  for an assumed type of specimen is determined from the following formula [2]:

$$G_{1c} = \frac{3}{2} \cdot \frac{P_c \cdot \delta}{B \cdot a} \quad (7)$$

where:

- $\delta$  – crack (gap) opening.

The corrected crack length equal to  $a + |\Delta|$  was determined on the basis of the beam theory in which experiment conditions and influence of real geometry have been accounted for. The

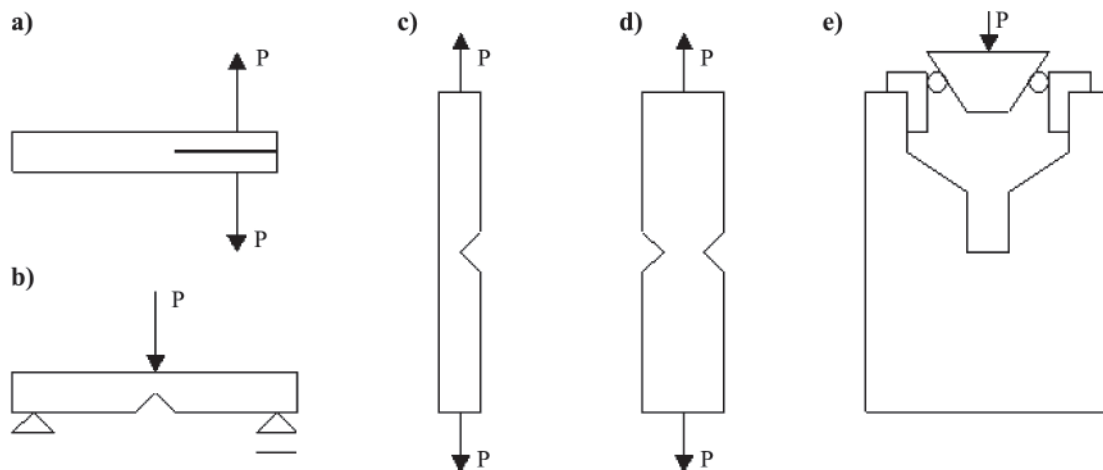


Fig. 6. Specimens for determining fracture toughness of wood elements loaded in compliance with the mode I: a) double cantilever beam specimen, b) one-sided-notched specimen under three-point bending, c) one-sided-notched specimen under tension, d) double-sided-notched specimen under tension, e) specimen for splitting test

unknown quantity  $\Delta$  was experimentally determined from the diagram  $C^{1/3}(a)$ . The relation was built graphically by measuring the flexibility  $C$  for a few different values of the crack length  $a$ . The straight line approximating the diagram  $C^{1/3}(a)$  determines the quantity  $\Delta$  on the horizontal axis level (Fig. 7). The way of determining the quantity  $\Delta$  is described in detail in the work [7].

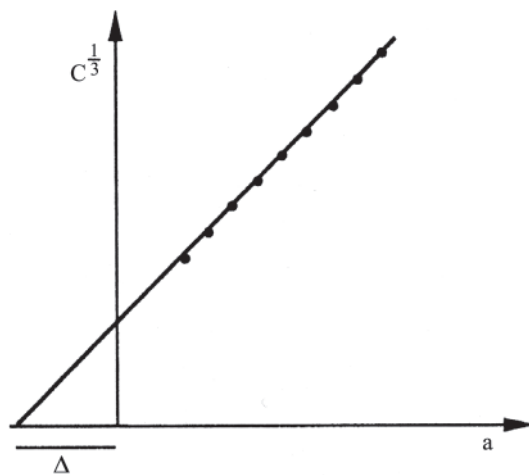


Fig. 7. Method for determining the linear correction  $\Delta$  to the beam theory [3]

For the double cantilever beam specimens the critical energy release coefficient  $G_{Ic}$  is determined from the formula as follows [7]:

$$G_{Ic} = \frac{3}{2} \cdot \frac{P_c \cdot \delta}{B \cdot (a + |\Delta|)} \quad (8)$$

The specimen flexibility  $C$  is determined by using Berry method, i.e. by means of the relation:

$$C = K \cdot a^n \quad (9)$$

where:

- $n$  – a coefficient experimentally determined on the basis of the diagram  $\ln(C)$  versus  $\ln(a)$
- $K$  – numerical value determined from the point of intersection of the diagram with the ordinate axis.

The diagram  $\ln(C)$  versus  $\ln(a)$  can be built by measuring the flexibility  $C$  for different values of the crack length  $a$  (Fig. 8).

The coefficient  $n$  is equivalent to its slope angle tangent. The critical energy release coefficient  $G_{Ic}$  is determined by using the following relation [8]:

$$G_{Ic} = \frac{1}{2} \cdot \frac{n \cdot P_c \cdot \delta}{B \cdot a} \quad (10)$$

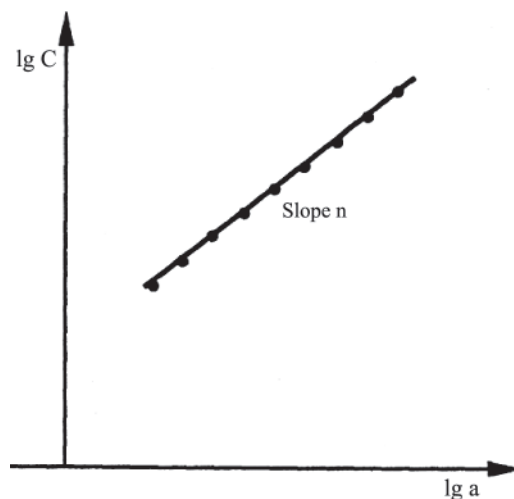


Fig. 8. Method for determining the coefficient  $n$

### Characteristics of the tested material and description of the test running

A natural and modified pine wood was used in the tests. Modification of wood by means of methyl polymethacrylate improves its properties. The detailed description of run of the modification process by using methyl polymethacrylate as well as properties of the modified wood are given in the work [4]. In Tab. 1 and 2 are exemplified values of material constants as well as strength properties of the natural and modified wood [4].

The fracture toughness tests of natural and modified wood were conducted with the use of the universal electrohydraulic testing machine MTS-81012. The tested specimens were made of the natural wood of abt. 12% humidity and modified one of abt. 8% humidity. The tests were performed in the room temperature of abt. 20° C. The DCB specimens were used in the tests (Fig. 9). They were made of the same batch of wood on the basis of which their strength properties were earlier determined [4]. For the specimens the square cross-section of 20 mm x 20 mm sides, was assumed. The gap was cut by using

a saw of 1.8 mm in thickness and 70 mm in length, and then it was deepened up to 80 mm by using a thin blade.

Tab. 1. Values of the material constants of the natural and modified wood

Material constant	K0.0	K0.56
$E_R = E_1$ [GPa]	2.15	5.09
$E_T = E_2$ [GPa]	2.35	5.12
$E_L = E_3$ [GPa]	11.85	16.45
$G_{TL} = G_{23}$ [GPa]	0.72	2.57
$G_{LR} = G_{31}$ [GPa]	1.04	2.34
$G_{RT} = G_{12}$ [GPa]	0.91	1.94
$\nu_{RL} = \nu_{13}$	0.06	0.08
$\nu_{TL} = \nu_{23}$	0.07	0.05
$\nu_{LT} = \nu_{32}$	0.35	0.18
$\nu_{RT} = \nu_{12}$	0.58	0.34
$\nu_{TR} = \nu_{21}$	0.66	0.35
$\nu_{LR} = \nu_{31}$	0.32	0.28

**Notation:** the symbol K0.0÷K0.56 stands for amount of methyl methacrylate [kg] per 1 kg of dry wood

Tab. 2. Strength limits for natural and modified wood under tension, compression and shear load, respectively

Kind of material	$R_{m_{II}}$ [MPa]	$R_{c_{II}}$ [MPa]	$R_{m_{\perp}}$ [MPa]	$R_{c_{\perp}}$ [MPa]	$R_t$ [MPa]
<b>K0.0</b>	95	55	4.5	8.5	22.10
<b>K0.56</b>	118	98	9	32	30.20

**Notation:**  $R_{m_{II}}$  - tensile strength along fibres;  $R_{c_{II}}$  - compression strength along fibres;  $R_{m_{\perp}}$  - tensile strength across fibres;  $R_{c_{\perp}}$  - compression strength across fibres;  $R_t$  - shear strength

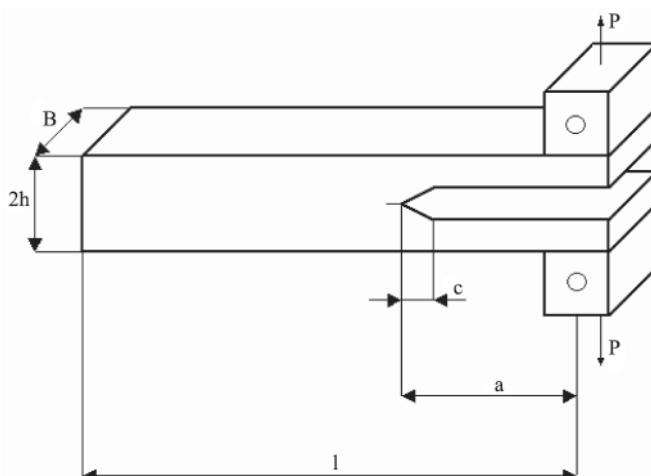


Fig. 9. DCB specimen used in the tests, of the dimensions:  $l = 200$  mm,  $a = 80$  mm,  $c = 10$  mm,  $B = 2h = 20$  mm

For description of wood fracture toughness the energy release coefficients  $G_{ac}$  were used in view of anisotropy of the tested material. The tests were conducted for two modes of crack propagation in wood, i.e. for the tangential – longitudinal

direction TL and the radial – longitudinal direction RL. They were performed for the gap length  $a = 80$  mm. The specimens complied with the provisions of the PN-EN 408 standard. The pine wood was suitably dried and prepared to testing. For the specimens 200 mm length was selected, i.e. ten times greater than the greater dimension of their cross-section which was on average equal to 20 mm in the case of the modes RL and TL. Load was applied to the specimens at the constant rate of 0.03 mm/s. Special holding devices (chucks) had to be manufactured to make performing the tests with the use of the MTS machine possible. The tested material was glued to the chucks by means of the „PATTEX”, a universal glue for wood.

Each of the specimens was measured with the accuracy of 0,01 mm and marked in line with its direction of orientation. On each specimen measuring length was made with the accuracy up to 0,01 mm, in order to analyze fracture toughness coefficient. During the tests values of the load  $P$  and displacement  $\delta$  were recorded. Value of the critical load was determined by means of the method  $P(\delta)$  (Fig. 4). The load  $P$  and displacement  $\delta$  was recorded by using the measuring system consisted of a computer and A/D card.

For determining the critical fracture toughness coefficient  $G_{Ic}$ , it is necessary to know the coefficient  $n$  whose value for a given kind of wood is determined experimentally on the basis of the approximation of function of flexibility versus gap length. As in the available literature sources the  $n$ -coefficient value for Douglas fir equal to  $n = 2.80$  is found and pine wood properties are close to those of Douglas fir, hence for further calculations  $n = 2.80$  was assumed for the pine wood [9]. On the basis of the relation (11) were determined critical values of the energy release coefficient  $G_{Ic}$  of the natural and modified wood specimens for the directions RL and TL.

Based on the assumed value of the coefficient  $n = 2.80$ , the critical coefficient  $G_{Ic}$  of the tested and modified wood for the modes TL and RL can be determined from the relation:

$$G_{Ic} = \frac{1}{2} \cdot \frac{2,80 \cdot P_c \cdot \delta}{B \cdot a}$$

The tests of natural and modified wood fracture toughness for the mode TL demonstrated that the crack initiation was triggered off before the load applied to the specimens obtained its maximum value. The determined critical load was equal on average to 80% of the maximum load. The initial cracking run was mild, then passing to violent. As observed, in the natural wood specimens occurred a single crack which was next developing until the maximum stresses were exceeded (Fig. 10). In the case of the mode TL the crack propagated almost parallel to direction of the fibres.

In the case of the mode RL the crack was initiated, like in the preceding case, already before the element reached its maximum load. The determined average load was equal to 85% of the maximum one. In the mode RL the crack was developing in a stable way both in the specimens of natural and modified wood, as shown in Fig. 10. The specimens under tension in the mode RL, cracked along the fibres. The crack propagation direction was in line with the anatomic direction of the fibres. The crack propagated along the hardwood-softwood boundary. In the mode TL, like in the mode RL, the crack propagated up to the moment of splitting the specimens, however in the specimens of modified wood it was propagating slowly.

Results of the tests of the specimens made of natural and modified wood, loaded in the way I of the modes TL and RL, will be presented in the next part of the paper.



## RESULTS OF FRACTURE TOUGHNESS TESTS OF STRUCTURAL TIMBER

The cracks in wood specimens have developed in different ways depending on a propagating mode. For the mode TL, value of the applied axial force was increasing up to the critical load  $P_c$ . In this mode, single cracks appeared in the specimens; they were developing until the maximum stress values were reached. As shown in Fig. 10, the cracks propagated parallel to direction of fibres. It was observed that cracks were developing in the same way in the tested specimens for the same loads and constant time intervals. The 20 mm long fracture was formed. The identical crack development process in the tested specimens results from the fact that they were cut from neighbouring areas of the tested material.



Fig. 10. Images of crack propagation surfaces in the specimens in the mode TL: a) natural wood, b) modified wood

In the case of the mode RL (Fig. 11) the crack was propagating steadily along wood fibres. The cracking process of the specimens developed faster as it met a smaller resistance than in the mode TL. It results from the internal structure of the wood, an orthotropic material. In the mode RL the alternate softwood and hardwood layers makes that in their planes cracks develop under smaller loads than in the case of the mode TL.



Rys. 11. Images of crack propagation surfaces in the specimens in the mode RL: a) natural wood, b) modified wood

### SUMMARY

- This work aimed at fracture toughness determination of natural and modified pine wood, made it possible to determine, by means of the method  $P(\delta)$ , the load which

initiates cracking process. The method is capable of determining, in a simple and sufficiently accurate way, the instant of initiating the cracking process. As results from the performed tests, the ratio of the load in question and the maximum load was equal to about 0,80 for the mode TL and about 0.85 for the mode RL.

- The fracture toughness of natural and modified pine wood was determined experimentally by means of critical values of the energy release coefficients  $G_{lc}$  complying with the relation (11), to be presented in the next part of the work.
- In the tests were used the beam specimens which make it possible to model real phenomena of cracking the wood elements containing defects. The critical coefficients  $G_{lc}$  were determined with the use of the beam theory accounting for material anisotropy. The critical values of the coefficients  $G_{lc}$ , determined for the splitting of natural and modified pine wood, were practically identical for both analyzed crack propagation modes: RL and TL.

### NOMENCLATURE

- a - crack length
- B - specimen thickness
- $G$  - energy release coefficient
- $K_a$  - stress intensity factor
- $L_a$  - longitudinal direction
- R - radial direction
- T - tangent direction
- l - specimen length
- P - load
- U - potential energy released during cracking
- $\delta$  - crack opening.

### BIBLIOGRAPHY

1. Blicharski M.: *Deforming and cracking* (in Polish). Uczelniane Wydawnictwa Naukowe – Dydaktyczne (University Scientific Didactic Publishing House), Cracow, 2002
2. Dobrzański L. A.: *Metal materials for engineering* (in Polish). Wydawnictwo Naukowe – Techniczne (Scientific Technical Publishing House), Warsaw, 2004
3. Gołaski L.: *Elements of experimental fracture mechanics* (in Polish). Wydawnictwo Politechniki Świętokrzyskiej (Publishing House of Saint Cross University of Technology), Kielce, 1992
4. Kyzioł L.: *Analysis of properties of structural timber superficially saturated with MM polymer* (in Polish). Akademia Marynarki Wojennej (Polish Naval Academy), Gdynia, 2004
5. Neimitz A.: *Fracture mechanics* (in Polish). Wydawnictwo Naukowe PWN (Polish Scientific Publishing House), Warsaw, 1998
6. Ochelski S.: *Experimental methods in mechanics of structural composites* (in Polish). Wydawnictwa Naukowe – Techniczne (Scientific Technical Publishing House), Warsaw, 2004
7. Davies P.: *Protocols for Inter-laminar Fracture Testing of Composites. European Structural Integrity Society, Polymers & Composites Task Group*, 1992
8. Ducept F., Davies P., Gamby B.: *An Experimental Study of Validation Tests Used to Determine Mixed Mode Failure Criteria of Glass/Epoxy Composites*. Composites, Part A, Vol. 28 A, 1997.
9. Schniewind A. P., Pozniak R., A.: *On the Fracture Toughness of Douglass Fir Wood*. Engineering Fracture Mechanics, Vol. 2, 1971

### CONTACT WITH THE AUTHOR

Lesław Kyzioł, Ph.D.  
 Faculty of Mechanical and Electrical Engineering  
 Institute of Basic Engineering  
 Polish Naval Academy in Gdynia  
 Śmidowicza 69  
 81-103 Gdynia, POLAND  
 e-mail: L.Kyziol@amw.gdynia.pl



The Ship Handling Research and Training Centre at Ilawa is owned by the Foundation for Safety of Navigation and Environment Protection, which is a joint venture between the Gdynia Maritime University, the Gdansk University of Technology and the City of Ilawa.

**Two main fields of activity of the Foundation are:**

- Training on ship handling. Since 1980 more than 2500 ship masters and pilots from 35 countries were trained at Ilawa Centre. The Foundation for Safety of Navigation and Environment Protection, being non-profit organisation is reinvesting all spare funds in new facilities and each year to the existing facilities new models and new training areas were added. Existing training models each year are also modernised, that's why at present the Centre represents a modern facility perfectly capable to perform training on ship handling of shipmasters, pilots and tug masters.
- Research on ship's manoeuvrability. Many experimental and theoretical research programmes covering different problems of manoeuvrability (including human effect, harbour and waterway design) are successfully realised at the Centre.

The Foundation possesses ISO 9001 quality certificate.

**Why training on ship handling?**

The safe handling of ships depends on many factors - on ship's manoeuvring characteristics, human factor (operator experience and skill, his behaviour in stressed situation, etc.), actual environmental conditions, and degree of water area restriction.

Results of analysis of CRG (collisions, rammings and groundings) casualties show that in one third of all the human error is involved, and the same amount of CRG casualties is attributed to the poor controllability of ships. Training on ship handling is largely recommended by IMO as one of the most effective method for improving the safety at sea. The goal of the above training is to gain theoretical and practical knowledge on ship handling in a wide number of different situations met in practice at sea.

For further information please contact:

**The Foundation for Safety of Navigation and Environment Protection**

Head office:  
36, Chrzanowskiego Street  
80-278 GDAŃSK, POLAND  
tel./fax: +48 (0) 58 341 59 19

Ship Handling Centre:  
14-200 ILAWA-KAMIONKA, POLAND  
tel./fax: +48 (0) 89 648 74 90  
e-mail: office@ilawashiphandling.com.pl  
e-mail: office@portilawa.com



## GDANSK UNIVERSITY OF TECHNOLOGY

is the oldest and largest scientific and technological academic institution in the Pomeranian region. The history of Gdansk University of Technology is marked by two basic dates, namely: October 6, 1904 and May 24, 1945.

The first date is connected with the beginning of the technical education at academic level in Gdansk. The second date is connected with establishing of Gdansk University of Technology, Polish state academic university. Gdansk University of Technology employ 2,500 staff, 1,200 whom are academics. The number of students approximates 20,000, most of them studying full-time. Their career choices vary from Architecture to Business and Management, from Mathematics and Computer Science to Biotechnology and Environmental Engineering, from Applied Chemistry to Geodesics and Transport, from Ocean Engineering to Mechanical Engineering and Ship Technology, from Civil Engineering to Telecommunication, Electrical and Control Engineering. Their life goals, however, are much the same - to meet the challenge of the changing world. The educational opportunities offered by our faculties are much wider than those of other Polish Technical universities, and the scientific research areas include all of 21st Century technology. We are one of the best schools in Poland and one of the best known schools in Europe – one that educates specialists excelling in the programming technology and computer methods used in solving complicated scientific, engineering, organizational and economic problems.

### THE FACULTY OF OCEAN ENGINEERING AND SHIP TECHNOLOGY

The Faculty of Ocean Engineering and Ship Technology (FOEST) as the only faculty in Poland since the beginning of 1945 has continuously been educating engineers and doctors in the field of Naval Architecture and Marine Technology.

The educational and training activities of FOEST are supported by cooperation with Polish and foreign universities, membership in different international organizations and associations, as well as participation in scientific conferences and symposia. Hosting young scientists and students from different countries is also a usual practice in FOEST.


The activities of Faculty departments are related to: mechanics and strength of structures, hydromechanics, manufacturing, materials and system quality, power plants, equipment and systems of automatic control, mostly in shipbuilding, marine engineering and energetic systems.

FOEST is a member of such organizations like WEGEMT; The Association of Polish Maritime Industries and the co-operation between Nordic Maritime Universities and Det Norske Veritas. The intensive teaching is complemented and supported by extensive research activities, the core of which is performed in close collaboration between FOEST staff and industry. We take great care to ensure that the applied research meet both the long term and short term needs of Polish maritime industry. FOEST collaborates with almost all Polish shipyards. Close links are maintained with other research organizations and research institutions supporting the Polish maritime industry, such as Ship Design and Research Centre and Polish Register of Shipping, where several members of the Faculty are also members of the Technical Board.

The Faculty of Ocean Engineering and Ship Technology is a unique academic structure, which possesses numerous highly qualified and experienced staff in all above mentioned specific research areas. Moreover, the staff is used to effective co-operation and exchange of ideas between specialists of different detailed areas. This enables a more integrated and comprehensive treatment of research and practical problems encountered in such a complicated field of activity as naval architecture, shipbuilding and marine engineering.


The staff of the Faculty has strong international links worldwide, being members or cooperating with international organizations like International Maritime Organization IMO, International Towing Tank Conference ITTC, International Ship and Offshore Structures Congress ISSC, International Conference on Practical Design of Ship and other floating Structures PRADS just to name a few.

GDANSK UNIVERSITY OF TECHNOLOGY  
Faculty of Ocean Engineering and Ship Technology  
11/12 Narutowicza Street, 80-952 Gdansk, Poland  
Tel (+48) 58 347 1548 ; Fax (+48) 58 341 4712  
e-mail: sekoce@pg.gda.pl



# Gdansk University of Technology

## Faculty of Ocean Engineering and Ship Technology



[www.oce.pg.gda.pl](http://www.oce.pg.gda.pl)